Jungang Yin

Multi(Wide)-Band Multi-Functional Antennas Based On Folded Dipoles

Thesis for the degree of Philosophiae Doctor

Trondheim, September 2011

Norwegian University of Science and Technology
Faculty of Information Technology, Mathematics and Electrical Engineering
Department of Electronics and Telecommunications

NTNU – Trondheim
Norwegian University of
Science and Technology

NTNU
Norwegian University of Science and Technology

Thesis for the degree of Philosophiae Doctor

Faculty of Information Technology, Mathematics and
Electrical Engineering
Department of Electronics and Telecommunications

© Jungang Yin

ISBN 978-82-471-3047-6 (printed ver.)
ISBN 978-82-471-3048-3 (electronic ver.)
ISSN 1503-8181

Doctoral theses at NTNU, 2011:243

Printed by NTNU-trykk

0.1 Abstract

Keywords: Orthogonal Folded Dipoles (OFD), Log-Periodic Folded Dipole Array (LPFDA), Eleven antenna, monopulse tracking, Genetic Algorithms (GA's), radio telescopes, reverberation chamber, Multiple-Input-Multiple-Output (MIMO)

This doctoral thesis deals with designs and developments of multi(wide)-band multifunctional antennas based on folded dipoles.

In the beginning, the concept of Orthogonal Folded Dipoles (OFD) are put forward. Orthogonal folded dipoles are formed by two identical two-port folded dipoles orthogonally joining with each other at the center, and can be fed through different combinations of feed nodes to offer dual- and wide-band modes, respectively. The impedances of the 2 modes are studied both by analytical models and by commercial electromagnetic simulation tools. The properties of the linearly polarized radiation patterns in the two modes vary quite little, except for ±45° rotation of two principal planes. In this way, orthogonal folded dipoles can possibly provide pattern reconfigurability in a context of switchable types and orientations of polarizations.

Next, the concept of Log-Periodic Folded Dipole Array (LPFDA) is proposed. It stems from the traditional log-periodic dipole array, whereas folded dipoles instead of straight dipoles are applied as the elements of the array. Two configurations, i.e. partly-scaled LPFDA and fully-scaled LPFDA, are studied through simulations and optimizations. The comparison shows that the latter outperforms the former in terms of higher directivity, reduced front-to-back ratio and lower crosspolar level.

The key parts of this thesis focus on exploiting Eleven antennas, based on the LPFDAs, in a variety of applications. First, the 4-port L-band lab model for use in satellite terminals demonstrates that the radiation patterns for monopulse tracking can be achieved through different excitation combinations of the multiport Eleven antenna. Second, a decade bandwidth, an unchanged phase center and nearly constant directivities over the whole band can be regarded as the major figure-of-merit of the Eleven antenna, which makes it suitable as feed for prime-fed reflector antennas. Through endeavors of using Genetic Algorithms, the wideband Eleven antennas have been gradually optimized in term of matching as well as efficiencies. Besides, the rotationally symmetric circular Eleven feed is a very promising solution for improving the BOR1 efficiency and therefore the aperture efficiency by a fraction of dB. Last but not least, the two multiport L-band lab models measured in a reverberation chamber demonstrate that the Eleven antenna with MIMO diversity ports can possibly overcome narrowband multipath fading in a real radio link and improve the link quality in terms of a significant diversity gain and high maximum available capacity.

0.2 Preface

This thesis is submitted to the Norwegian University of Science and Technology (NTNU) for partial fulfilment of the requirements for the degree of *Doktor Ingeniør*.

From autumn of 2005 to spring of 2011, this doctoral project has been carried out at the Department of Electronics and Communications (IET), NTNU, Trondheim, with Associate Professor Jon Anders Aas as the main supervisor. The first years were partly spent on compulsory courses, which laid a solid theoretical foundation for this thesis. Moreover, I spent one year working as a teaching assistant in various undergraduate/graduate courses at NTNU, including Antenna Engineering, Radio Communications, Passive Microwave Components, etc. During 2006-2011, a close collaboration in terms of regular/short courses, technical meetings/seminars as well as joint scientific papers/presentations, has been carried out together with the Antenna Group at Chalmers University of Technology (Chalmers), Gothenburg, Sweden. Professor Per-Simon Kildal and Associate Professor Jian Yang at Chalmers act as my co-supervisors.

This doctoral work was primarily funded by the Research Council of Norway (NFR) and partly funded by internal scholarship and traveling grants offered by IET, NTNU. The important results of this thesis have been reported in 9 international conference or journal papers (refer to Appendix C).

By the way, anyone who has comments on this thesis is welcome to contact me even in the future.

0.3 Acknowledgements

About 2500 years ago, the most famous thinker and philosopher in Chinese history, Confucius, once said that: "As any three persons walk together, one of them is bound to be good enough to act as a teacher for the rest."

About 1200 years ago, another famous philosopher in Chinese Tang Dynasty, Yu Han, once said that: "A teacher, is a person who disseminates philosophy of life among students, passes on knowledge to students and answers questions from students."

Through my work and life in Norway and Sweden during 2005-2011, I have gained more in-depth understanding of what those sayings concerning teachers actually mean.

First of all, I would like to thank my main supervisor Jon Anders Aas at NTNU for his guidance, encouragement and patience during the course of this doctoral work. He is a true friend both inside and outside work. I was greatly impressed by his persistence and precision on his career in the field of antennas and propagation for almost half a century. We established good cooperations both on research work and on course duties. Besides, personal contacts and activities at leisure time also gave me great memories that I will never forget.

Second, I am very grateful to my co-supervisor Prof. Per-Simon Kildal at Chalmers in Sweden. Without his enlightening wisdom, helpful discussions and extensive comments, I am afraid that this thesis would never have been a reality. The second co-supervisor Jian Yang gives me valuable tutorials on antenna design and optimization, and also contributes a great deal to my thesis.

My thanks also go to all my colleagues with the Radio System Group at NTNU. Our group chair Morten Olavsbråten kept in charge of my case after Jon Anders Aas retired in summer 2009; Terje Mathiesen fixed my computer problems as well as manufactured a couple of antenna models for tests; Xin Li proof-read the last major chapter of the thesis; Marius Ubostad updated the software for the instruments in our antenna lab; Kari Berit Øien and Kirsten Ekseth handled all the non-technical issues concerning this thesis ... I can not in here name all the endeavor and help my colleagues did to me.

Special thanks go to all the colleagues and friends with the Antenna Group at Chalmers. I will forever bear in mind Yogesh Karandikar's interpretation of aperture efficiency by analogy with a shower on a barrel, Daniel Nyberg's help on the measurement procedure inside a reverberation chamber, Xiaoming Chen's backup presentation in Taipei, and so on and on. Besides, I would also like to thank Agneta Kinnander at S2 Chalmers for lending me a helping hand with non-technical things when I stayed in Gothenburg.

At last, but not least, I would like to thank my parents, relatives, friends and the most important one when it comes to my life, my beloved wife, Fan Zheng.

Contents

0.1 Abstract i

Abstract **i**

0.2 Preface iii

Preface **iii**

0.3 Acknowledgements v

Acknowledgements **v**

Contents **ix**

List of Tables **xi**

List of Figures **xviii**

Abbreviation **xix**

1 Introduction **1**

1.1 Background 1

1.2 Thesis Outline 5

2 Basics of Simulation and Optimization Technology for This Thesis **7**

2.1 Computational Electromagnetics 7

2.1.1 Method of Moments 8

2.1.2 Finite Integration Technique 12

2.2 Optimization Methods 15

2.2.1 Genetic Algorithms 16

3 Antennas with Wideband Performance **19**

3.1 Background of Broadband Antennas 19

3.1.1 Traveling Wave Antennas 19

3.1.2 Helical Antennas 20

3.1.3 Biconical Antennas 21
3.2 Background of Frequency Independent Antennas 21
3.2.1 Principles 21
3.2.2 Spiral Antennas 22
3.3 Folded Dipole Antennas 23
3.3.1 Two-Port Wired Folded Dipole 23
3.3.2 Orthogonal Folded Dipoles 25
3.4 Summary of Chapter 3 32

4 Log-Periodic Folded Dipole Array 35
4.1 Background 35
4.2 Log-periodic Folded Dipole Array 37
4.2.1 LPFDA With Length and Spacing Log-periodically Scaled 38
4.2.2 LPFDA With All Dimensions Log-periodically Scaled 41
4.3 Summary of Chapter 4 46

5 Multi-Port Eleven Antenna For Use In Satellite Terminals 47
5.1 4-port Eleven Antenna For Monopulse Tracking 48
5.1.1 Impedance Model (Σ mode) 49
5.1.2 Radiation Model 54
5.2 Laboratory Demonstration 58
5.2.1 Network model 58
5.2.2 Feeding network 59
5.2.3 Feed without reflector 62
5.2.4 Feed with reflector 64
5.3 Review of a Dual-Band Feed Based on Choke Horn and Circular Eleven Antenna 70
5.4 Summary of Chapter 5 71

6 Wide Band Eleven Antennas As Feed For Radio Telescopes 73
6.1 Triple Bandwidth Simulation Models 73
6.1.1 Linearly Polarized Model 74
6.1.2 Dually Polarized Model 80
6.2 Review of Wide Band Models Below 3 GHz 83
6.3 Review of a Decade Wide Band Model 1-10 GHz 85
6.4 Review of an Ultra Wide Band Model Above 10 GHz 90
6.5 Circular Eleven Feed 93
6.6 Summary of Chapter 6 99

7 Multi-Port Eleven Antenna For Narrowband MIMO Applications 101
7.1 Background of Narrowband Radio Channel 101
7.1.1 AWGN Channel 102

    - 7.1.2 Rayleigh Fading Channel 102
    - 7.1.3 Rician Fading Channel 103
    - 7.1.4 Doppler Effect 104
  - 7.2 Background of Diversity Technology 105
    - 7.2.1 Diversity 106
    - 7.2.2 Combination Methods 107
  - 7.3 Background of Reverberation Chamber 108
  - 7.4 MIMO Performance of Multiport Eleven Antenna 112
    - 7.4.1 Scenario 1 & 2: 1×4 and 2×4 Models (Without Hybrids) 115
    - 7.4.2 Scenario 3: Combined 1×2 Model (1×4 With Hybrids) 117
    - 7.4.3 Scenario 4: Combined 2×2 Model (2×4 With Hybrids) 118
  - 7.5 Summary of Chapter 7 120

8 Conclusion and Future Work **123**

References **125**

A Computation of Aperture Efficiencies **137**
  - A.1 Radiated Power 137
  - A.2 Body of Revolution (BOR) 137
  - A.3 Aperture Efficiency 138
    - A.3.1 BOR1 Efficiency 139
    - A.3.2 Spillover Efficiency 139
    - A.3.3 Polarization Sidelobe Efficiency 140
    - A.3.4 Illumination Efficiency 140
    - A.3.5 Phase Efficiency 140

B Far Field of Paraboloidal Reflector **141**

C List of Publications **145**

List of Tables

3.1 Performance Details of Dual-band OFD Over Infinite PEC Ground 30
3.2 Performance Details of Wide-band OFD Over Infinite PEC Ground 32

4.1 Normalized Parameters For The Simple LPFDA 40
4.2 Normalized Parameters For The Modified LPFDA 44

5.1 Dimensions of manufactured L-band Eleven antenna 49
5.2 Dimensions of the L-band Eleven antenna in Fig. 5.14 59
5.3 Parameters of the paraboloidal reflector 64
5.4 Measured performance of C/Ku-band feed [1] 70

6.1 Normalized Parameters For Eleven Simulation Models 75
6.2 Results of one-by-one parameter optimization scheme [2] 87
6.3 Dimensions that define the circular Eleven antenna 96

7.1 Measured efficiencies, diversity gains and capacities at 1.57GHz 115

List of Figures

2.1 Categories within computational electromagnetics appeared in [3]. 7
2.2 The orthogonal hexahedral grid system used in CST. Courtesy of [4]. . . . 13
2.3 The leap-frog scheme for discretized set of MGEs. 15
2.4 Basic Genetic Algorithm Structure. 17

3.1 2-port (left) and 1-port (right) folded dipole. Note: the current amplitudes denoted in the figure are close to the corresponding feed nodes. . . . 24
3.2 Dual-band (left) and wide-band (right) orthogonal folded dipoles 25
3.3 Input admittance of the dual-band OFD 26
3.4 Calculated and simulated S_{11} of the dual-band OFD (reference: 300Ω) . . 27
3.5 Wide-band OFD ($L = 265\ mm, a = 1.53\ mm, s = 5.1\ mm$) Note: the current amplitudes denoted in the figure are close to the corresponding feed nodes. 27
3.6 Calculated and simulated S_{11} of wide-band OFD (reference: 300 Ω) . . . 28
3.7 Simulated E-field patterns of dual-band OFD at 0.45 GHz (0.287$\lambda_{0.65GHz}$ over infinite PEC ground) 29
3.8 Simulated E-field patterns of dual-band OFD at 0.65 GHz (0.287$\lambda_{0.65GHz}$ over infinite PEC ground) 30
3.9 Simulated E-field patterns of wide-band OFD at 0.45 GHz (0.287$\lambda_{0.65GHz}$ over infinite PEC ground) 31
3.10 Simulated E-field patterns of wide-band OFD at 0.60 GHz (0.287$\lambda_{0.65GHz}$ over infinite PEC ground) 31
3.11 2-port wide-band OFD over infinite PEC ground (CST model) 32
3.12 S-parameters in dB of 2-port wide-band OFD over infinite PEC ground (Ref: 280 Ω, CST) 32

4.1 A log-periodic dipole array with apex angle 2α 36
4.2 Two feed methods: Straight (left) and crisscross connection (right). 37
4.3 Partly-scaled strip-type 8-pair LPFDA (upper half) 38
4.4 S_{11} magnitude in dB and Smith chart of partly-scaled 8-pair LPFDA (Ref: 200 Ω, CST) 39
4.5 Fully-scaled strip-type 8-pair LPFDA (upper half) 41

4.6 Fully-scaled strip-type 8-pair LPFDA modeled in CST 42

4.7 S_{11} magnitude in dB and Smith chart of fully-scaled 8-pair LPFDA (Ref: 280 Ω, CST) 43

4.8 A) a) H-plane copolar directivity B) b) E-plane copolar directivity C) c) 45°-plane relative crosspolar level of partly-scaled and fully-scaled 8-pair LPFDA, respectively (CST) 45

5.1 Monopulse beams: the sum and the difference beams in one plane 47

5.2 Manufactured L-band Eleven antenna and its model in CST 48

5.3 Pair of folded dipoles under the Eleven configuration and its equivalent antenna mode 49

5.4 Two-conductor transmission line with circular cross section (left) and the equivalence between circular and rectangular cross sections(right) 50

5.5 Real part of self and mutual impedance of the Eleven antenna shown in Table 5.1. 51

5.6 Imaginary part of self and mutual impedance of the Eleven antenna shown in Table 5.1. 52

5.7 The model of the center network in CST (p1 stands for port1 and so on). . 52

5.8 Calculated, simulated and measured reflection coefficients of the Eleven antenna. ("2-mode" means that both the antenna mode and the transmission line mode are taken into account on the folded dipoles). 53

5.9 Top and side views of sum channel model 54

5.10 Type-I and Type-II monopoles 54

5.11 Calculated and CST-simulated sum patterns in E and H planes (normalized). 57

5.12 Top and side views of horizontal difference channel model. 57

5.13 Calculated and CST-simulated horizontal difference patterns (normalized). 58

5.14 The equivalent network model of the 4-port folded dipole pair 58

5.15 Excitations for 3 modes of the 4-port folded dipole pair 59

5.16 The block diagram of the antenna system for any of the monopulse channels 60

5.17 The principle diagram (left) and the block diagrams of the feeding (comparator) networks (right). Note that the blocks marked with "*" are 180° hybrids, and the blocks marked with "#" are power dividers. 62

5.18 Port S-parameters magnitude in dB (left); total S11 magnitude in dB for sum and two difference channels (right) 63

5.19 Simulated (left) and measured (right) co- and cross-polar components of sum beam 63

5.20 Simulated (left) and measured (right) co- and cross-polar components of horizontal difference beam 63

5.21 Simulated (left) and measured (right) co- and cross-polar components of vertical difference beam 64

5.22 Directivity vs. spacing (S) for Σ channel 65

5.23 Efficiencies vs. spacing (S) for Σ channel 66
5.24 Total S_{11} vs. spacing (S) for Σ channel 66
5.25 Sum beam after reflection for Σ channel (spacing S=0.65λ) 67
5.26 Total S_{11} vs. spacing (S) for Δ_h channel 68
5.27 Horizontal difference beam after reflection for Δ_h channel (spacing S=0.65λ) 68
5.28 Total S_{11} vs. spacing (S) for Δ_v channel 69
5.29 Vertical difference beam after reflection for Δ_v channel (spacing S=0.65λ) 69
5.30 C/Ku-band feed prototype geometry [1] 70
5.31 Simulated and measured radiation patterns of the Eleven feed and choke horn in ϕ=45° plane at 6 and 10.5 GHz [1]. 71

6.1 Linearly polarized simulation models without (left) and with (right) PCB over an infinite ground plane (8-pair folded dipoles on one petal). 74
6.2 Simple side view graph of one antenna petal after displacement and rotation (X_0 is equivalent to -Z_0 in Figure 4.3). 74
6.3 CST-simulated S_{11} of linearly polarized ideal models without and with PCB (reference: 200 Ω); CST-simulated S_{11} of a linearly polarized real model without PCB (fed by pairs of 50 Ω coaxial cables). 76
6.4 CST-simulated BOR1 patterns (in ϕ=45^o plane) of linearly polarized ideal models (over infinite ground plane) without (left) and with (right) PCB. . 76
6.5 Calculated efficiencies of linearly polarized ideal models without and with PCB (half subtended angle = 60^o). Plotted at an interval of 0.5 GHz. 77
6.6 Drawing of symmetrical half of the real feed with regard to half ground plane (some dimensions are not in right proportion). Top view (left) and side view (upper right) of the hole and the transmission pins; top view (lower right) of the parallel trapezoidal matching lines. 78
6.7 Real feed model in CST. The trapezoidal lines are connected with a pair of 50 Ω coaxial cables that are shorted to the ground plane. 78
6.8 Dually polarized ideal model without PCB over an infinite ground plane; real feed model in CST (the trapezoidal lines are connected with a pair of 75 Ω coaxial cables that are shorted to the ground plane). 80
6.9 CST-simulated S_{11} of a dually polarized ideal model (reference: 300 Ω) and a real model (fed by pairs of 75 Ω coaxial cables). 80
6.10 Left: Simulated BOR1 copolar directivities of the three Eleven simulation models; Right: CST-simulated BOR1 patterns (in ϕ=45^o plane) of dually polarized ideal model (over infinite ground plane). 81
6.11 Calculated efficiencies of dually polarized Eleven ideal model (half subtended angle = 60^o). Plotted at an interval of 0.5 GHz. 81

6.12 Three previous all-metal Eleven feed models developed for use in Green Bank radio telescope for 150 - 1700 MHz (left), in RATAN telescope for 500 - 3000 MHz (middle), and in Giant Meter Radio Telescope for 200 - 800 MHz (right). 83

6.13 Simulated and measured reflection coefficients of Eleven feed for Green Bank, GMRT and RATAN radio telescopes, from left to right, respectively [5] [6]. 83

6.14 Measured and simulated radiation patterns in 45 degree plane of Eleven feed for RATAN telescope at selected frequencies. Red lines are measured. Blue are simulated. Solid lines are co-polar patterns. Dashed lines are cross-polar patterns [6]. 84

6.15 Measured radiation efficiencies of Green Bank (top) and RATAN (bottom) models by using reverberation chamber. Note that some efficiencies being larger than 0 dB is due to the 0.5 dB RMS accuracy of the reverberation chamber [6]. 85

6.16 Configuration of Eleven feed of single polarization and parameters describing the geometry of the two petals [2]. 86

6.17 Eleven feed for 1-10 GHz (21-pair dipoles) and the measurement set-up for reflection coefficient [2]. 87

6.18 Measured and simulated reflection coefficient [2]. 88

6.19 Measured (a) and simulated (b) radiation patterns in ϕ=45° plane. Solid line-copolar, dash line-crosspolar. Measured and simulated directivity (upper right). Radiation efficiency measured in Bluetest's reverberation chamber (bottom right) [2]. 89

6.20 Modeling in CST and hardware of the dually polarized Eleven feed for 2-13 GHz (14-pair dipoles). The octagon of metal dewar has a circumradius of 200 mm [7]. 90

6.21 Simulated (dash) and measured (solid) reflection coefficient of the dually polarized Eleven feed, and the final result (dot) of optimized linearly polarized Eleven feed [7]. 91

6.22 Simulated and measured efficiencies of the dually polarized Eleven feed (left); simulated and measured directivity of the dually polarized Eleven feed (upper right); measured radiation pattern of BOR1 component (bottom right) [7]. 92

6.23 Flat petal plate above ground disc with angle $ang0$ from the ground plane (top); example of auxiliary circular cylinder used to find the circularly curved shape of the folded dipoles on the petal. The shape appears circular when seen from above (middle, bottom). 94

6.24 Dimensions that define the antenna structure (the denoted lengths are projected lengths in the XY-plane; ang_1, ang_2 and ang_3 are the projected angles in the XY-plane of the denoted angles ang1′, ang2′ and ang3′, respectively). 95
6.25 Different views of circularly curved 8-pair-dipole Eleven antenna with dual linear polarization. 97
6.26 Simulated input reflection coefficient (with reference of 300 Ω port impedance) of the dually polarized circularly curved 8-pair-dipole Eleven antenna. . . 97
6.27 Co- and cross-polar radiation patterns (in $\phi = 45^\circ$ plane, in dBi) of the simulated total far field (upper) and the extracted BOR1 component (lower) of the dually polarized circularly curved Eleven antenna (the ground plane is set as an infinite PEC plane in CST. 98
6.28 Simulated directivities and cross-polar level of the BOR1 patterns over the whole band. Plotted at an interval of 0.1 GHz. 98
6.29 Calculated efficiencies when the dually polarized circularly curved Eleven antenna feeds a reflector with semi-subtended angle of 60°, based on the simulated far field by using CST. Plotted at an interval of 0.2 GHz. 99

7.1 Drawing (left) and photo (right) of the Bluetest reverberation chamber. Its measurement accuracy is 0.5 dB standard deviation. 109
7.2 Setup for measuring 3x4 (left) and 3x8 (right) MIMO system (3 wall antennas, 4 or 8 AUT ports). The antenna is a 1x4 and 2x4 port Eleven antenna, respectively, and the three antenna elements in the MIMO systems are the three orthogonal wall antennas in the reverberation chamber. 114
7.3 Measured embedded element efficiencies, normalized transmission CDFs and maximum available capacities (at 1.57 GHz) of 1x4 (left column) and 2x4 (right column) L-band Eleven antenna. The measurement was performed in Bluetest Reverberation chamber with accuracy of 0.5 dB standard deviation. 116
7.4 1×4 model with hybrids turns into a model with 1×2 combined ports. 50Ω resistors load the unused hybrid ports. 117
7.5 Scenario 3.1: Δ - Δ (Combined Port 1 - 2), diversity measured at 1.57 GHz. 117
7.6 Scenario 3.2: Δ - Σ (Combined Port 1 - 2), diversity measured at 1.57 GHz. 118
7.7 Scenario 3.3: Σ - Σ (Combined Port 1 - 2), diversity measured at 1.57 GHz. 118
7.8 2×4 model with hybrids turns into a model with 2×2 combined ports. 50Ω resistors load the unused hybrid ports. 119
7.9 Scenario 4.1: Δ - Δ - Δ - Δ (Combined Port 1 - 2 - 3 - 4), diversity measured at 1.57 GHz. 119
7.10 Scenario 4.2: Δ - Σ - Δ - Δ (Combined Port 1 - 2 - 3 - 4), diversity measured at 1.57 GHz. 120

7.11 Scenario 4.3: Δ - Σ - Σ - Δ (Combined Port 1 - 2 - 3 - 4), diversity measured at 1.57 GHz. 120
7.12 Scenario 4.4: Δ - Δ - Σ - Σ (Combined Port 1 - 2 - 3 - 4), diversity measured at 1.57 GHz. 121
7.13 Scenario 4.5: Δ - Σ - Σ - Σ (Combined Port 1 - 2 - 3 - 4), diversity measured at 1.57 GHz. 121
7.14 Scenario 4.6: Σ - Σ - Σ - Σ (Combined Port 1 - 2 - 3 - 4), diversity measured at 1.57 GHz. 122
7.15 Measured maximum available capacities of Eleven models varying with frequency (40 MHz interval) in all the scenarios (SNR = 15 dB). 122

B.1 GO reflection at a parabolic surface 141

Abbreviations

ACF	Auto-Correlation Function
ADS	Advanced Design System
AFS	Average Fading Sensitivity
AOA	Angle-of-Arrival
ATA	Allen Telescope Array
AUT	Antenna Under Test
AWGN	Additive White Gaussian Noise
BER	Bit Error Rate
BOR	Body of Revolution
CDF	Cumulative Distribution Function
CDMA	Code Division Multiple Access
CEM	Computational Electromagnetics
Chalmers	Chalmers University of Technology
DAB	Digital Audio Broadcasting
DTU	Technical University of Denmark
DVB	Digital Video Broadcasting
EM	Electromagnetics
EMC	Electromagnetic Compatibility
EMI	Electromagnetic Interference
FDTD	Finite Difference Time Domain
FER	Frame Error Rate
FIT	Finite Integration Techniques
FOV	Field-Of-View
GA	Genetic Algorithm
GBT	Green Bank Telescope

GMRT	Giant Meter Radio Telescope
GO	Geometrical Optics
GSO	Geostatoinary Orbit
GTD	Geometrical Theory of Diffraction
HOBF	Higher Order Basis Function
LOS	Line-of-Sight
LPDA	Log-Periodic Dipole Array
LPFDA	Log-Periodic Folded Dipole Array
MEG	Maxwell's Grid Equations
MIMO	Multiple-Input-Multiple-Output
MIT	Massachusetts Institute of Technology
MoM	Method of Moments
MWS	Microwave Studio
NASA	National Aeronautics and Space Administration
NFR	Norges Forskningsrådet
NLOS	Non-Line-of-Sight
NRAO	Natinal Radio Astronomy Observatory
OFD	Orthogonal Folded Dipoles
OFDM	Othorgonal Frequency Division Multiplexing
PBA	Perfect Boundary Approximation
PCB	Printed Circuit Board
PDF	Probability Density Function
PEC	Perfect Electrical Conductor
PMC	Perfect Magnetic Conductor
PML	Perfect Matched Layer
PO	Physical Optics
PTD	Physical Theory of Diffraction
RCS	Radar Cross Section
RFI	Radio Frequency Interference
SKA	Square Kilometer Array
SNR	Signal-to-Noise Ratio

TDMA	Time Division Multiple Access
TEM	Transverse Electromagnetic
TIS	Total Isotropic Sensitivity
TRP	Total Radiated Power
UWB	Ultra Wide Band
VLBI	Very Long Baseline Interferometry
WiMax	Worldwide Interoperability for Microwave Access
WLAN	Wireless Local Area Network
XPD	Crosspolar Power Discrimination

Chapter 1

Introduction

1.1 Background

During the recent decades, there has been growing interest in evolving from conventional narrowband systems to multi/wideband or even ultra wideband systems in many applications, such as wireless communications, microwave tomography, remote sensing and radio telescopes, etc. This has boosted considerable demands for new wideband microwave components, such as antennas, amplifiers, couplers, baluns and so on.

Since more and more wireless standards become commercialized in various civil applications, attention has been increasingly paid to reduce the number of antennas on different platforms by combining multiple functions in only one antenna, for the sake of cost, weight, compactness as well as aesthetic point of view. To achieve this, the multi-functional antenna needs to be multi/wideband to cover the frequencies of all functions. Today's iPhone, for instance, is compatible with 4 GSM bands, 3 UMTS/HSDPA bands, GPS, Wi-Fi, Bluetooth, etc. The advantages of multiband multifunctional antennas apply not only to cell phones, but also to mobile base stations, radio links, automobile electronics, aviation industry and so on.

In addition to the commercial applications, multi/wideband antennas also attract great interest in fundamental researches, particularly in radio astronomy. As a subfield of astronomy, radio astronomy studies celestial objects at the radio frequency portion of the electromagnetic spectrum. The initial detection of radio waves from an astronomical object was made in the 1930s, subsequent advances in the same century had identified a number of different sources of radio emission, including stars and galaxies as well as entirely new classes of objects, such as Pulsars and Masers, etc. Different from optical telescopes, the radio telescopes operate at radio frequencies, where they can detect and collect data on various radio sources. The Universe can be studied in unique ways by radio telescopes because radio waves penetrate dust, allowing us to look into regions, such as the center of our Galaxy, which are completely obscured at optical wavelengths. Radio astronomy is conducted using large radio antennas referred to as radio telescopes. A radio telescope is a form of highly directional antenna and is typically a large parabolic reflector antenna used singly or in an array. It is worth mentioning that the same types of antennas are also used in tracking and collecting data from satellites in space. Radio observatories are preferably located far from major centers of population in order to avoid electromagnetic interference (EMI) from radio, TV, radar, and other emitting sources.

In the past 20^{th} century, quite a few radio telescopes were built and developed in different sites world wide. In the following, I just want to name two out of all the telescopes, because some of the Eleven antennas (the main topic of my thesis) were delivered to them as feed candidates.

First, the Giant Meterwave Radio Telescope (GMRT), located near Pune in India, is the world's largest array of radio telescopes at meter wavelengths [8]. There are 14 telescopes randomly arranged in the central square, with a further 16 arranged in 3 arms of a nearly "Y"-shaped array, giving an interferometric baseline of about 25 km. Each antenna dish is 45 meters in diameter and, instead of a solid surface like many radio telescopes, the reflector is made of wire rope stretched between metal struts in a parabolic configuration. This meshing surface works well because of the long wavelengths (21 cm and longer) at which the telescope operates. The array can operate in 6 frequency bands centered around 50, 153, 233, 325, 610 and 1420 MHz. The correlation of radio signals from all the antennas or interferometers over several hours will thus enable radio images of celestial objects to be synthesized with a resolution equivalent to that obtainable with a single gigantic dish 25 km in diameter [9].

Second, the old 43-meter dish telescope located at the National Radio Astronomy Observatory's (NRAO) site in Green Bank, West Virginia, USA, is the second largest in the same site. By the way, the largest is the Robert C. Byrd Green Bank Telescope (GBT), where an off-axis feed arm cradles the dish, projecting upward at one edge, and the reflector surface is asymmetrical (actually a 100×110 meter section of a conventional, symmetric 208-meter paraboloid) [10]. During recent years, the Massachusetts Institute of Technology's (MIT) Lincoln Laboratory and NRAO have been collaborating to study turbulent properties of Earth's Ionosphere [11]. The 43-meter telescope is thus back online as part of the collaborative project, i.e., Bistatic Radar Observations of the Ionosphere, where the nature of the studies is such that a large bandwidth, from around 150 MHz to 10 GHz, is required.

Furthermore, in the 21^{st} century, scientists seek to understand the complete evolution of our Universe and its constituents. To attack these fundamental questions, a new generation of astronomical facilities is needed. Among others, the SKA (Square Kilometer Array) plays such a crucial role and is planned to be built by 2020. The SKA will provide continuous frequency coverage from 70 MHz to 10 GHz in the first phases of its construction; the extension of the array to higher frequencies is expected to take place after 2020 [12]. The SKA will be an aperture synthesis instrument, where signals from several thousand separated antennas will be combined digitally to simulate a telescope having a diameter equal to the largest antenna separation - more than 3000 km for the SKA. Consequently, the SKA will have an extremely high angular resolution and a very large field-of-view (FOV) . Besides, the use of phased-array technology is being explored to provide multiple FOVs, which would greatly increase the survey speed and enable multiple users to observe different pieces of the sky simultaneously. The SKA will be the world's premier imaging and surveying radio telescope with a combination of unprecedented versatility and sensitivity that will open up new windows of discovery. Another major radio astronomy project at the brink of a new era is the geodetic VLBI2010 (Very Long Baseline Interferometry) , which comes at a time when problems with aging antennas, a deteriorating RFI environment, obsolete electronics, and high operating costs are making current levels of accuracy, reliability, and timeliness difficult to sustain. VLBI2010 is a new set of criteria by which to measure the next generation geodetic VLBI system established based on the requirements of the Global Geodetic Observing System project of the International Association of Geodesy, and on the science driven geodetic goals outlined in the NASA Solid Earth Science Working Group report [13].

Historically and also presently, most radio telescopes only cover a narrow band of frequency. Some existing telescopes do however cover large bandwidth, but they use many different feeds and receiver systems at different times. In other words, the telescope can only be available at one narrow band at one time. Switching between different feeding systems in a giant reflector is really time-consuming and very often requires manual work or rather sophisticated mechanical solutions. In the radio astronomy community, multi/wideband feeds for the reflectors would be very beneficial, both from scientific, economical and practical point of view.

Paraboloidal reflector antennas were early used for long-distance radio communications and high-resolution radar applications. The most common feeds were half wavelength dipoles, waveguide or horn antennas. The radiation pattern of the half wavelength dipole with or without a ground disk is very different in the two principal planes, resulting in low efficiency, high spillover and high cross polarization; the cross polarization being detrimental in dually polarized systems. These deficiencies can be improved either by locating a metal ring of about one wavelength diameter above the dipole [14] [15], or by using two parallel dipoles with half wavelength spacing [16].

The horn feeds became quite popular during the 1980s, especially when corrugated horns were used to offer pretty good performance, typically within octave bandwidth, in terms of symmetrical main lobe and low cross polarization [17] [18]. Corrugated horns were and still are popular as feeds for reflectors. However, they are heavy and expensive, so simpler dielectric alternatives have been proposed [19] [20] [21]. The double-/quad-ridged horn provides even wider bandwidth, but the efficiency and cross polarization is not so good [22] [23]. A major problem of all the above mentioned horns in wideband applications is that the beamwidth varies significantly with frequency, unless the horn aperture is made very large. To improve this, a compact horn feed with constant beamwidth and low cross-polarization over almost an octave bandwidth was proposed in [24]. In addition, there exist also self-supported feeds for prime-focus reflectors, mounted at the center of the reflector with a tube containing the feed waveguides or cables. Such feeds include, for instance, the hat feed [25]. The hat feed has a ring-shaped phase center and a nearly 100% phase efficiency can by obtained by using a ring-shaped focus paraboloidal reflector [26]; however, the impedance bandwidth (<-15 dB) of the hat feed is usually within 40% [27] [28] [29].

End-fire style log-periodic dipole arrays [30] were traditionally used to generate medium gain over wide bandwidths for use in EMC measurements. However, they are not common as feeds for reflectors because their phase center varies strongly with frequency [31]. Due to that, a lot of efforts were made to reduce the phase center variation, for example, in the log-periodic array feed adopted in the Allen Telescope Array (ATA) [32]. The ATA [33] uses innovative 6.1-meter offset Gregorian dishes equipped with wideband feeds covering frequencies from 0.5 to 11 GHz. The first phase with 42 antennas (ATA-42) became operational in 2007; when completed, the array is expected to consist of 350 antennas. Nevertheless, the ATA feed is still significantly lossy due to the variable phase center and is very large in physical dimensions [34]. Moreover, it is difficult to place the receiver close to the feed point as this end-fire array is fed at the shortest dipoles; long transmission lines are thus needed, which will however give a significant noise contribution to the radio receiver.

As mentioned in one of the previous paragraphs, two parallel dipoles with half wavelength spacing can produce symmetrical radiation patterns in two principal planes. So can the wideband performance be obtained if we extend this dual dipole feed into a log-periodic version? If so, can we further solve problems on the ATA feed regarding the variable phase center, the large size and the end-fire feed style, etc.? Fortunately, the Eleven feed has answered all these questions. The Eleven feed, featured as a low-profile, log-periodic and ultra wideband antenna, has during the past few years been developed at Chalmers in Sweden. The basic geometry of the Eleven feed is two parallel folded dipoles half-wavelength apart above a ground plane. It can be used in both linear and dual polarizations, and its phase center changes very little with frequency [35]. In a nutshell, the Eleven feed is greatly suitable for reflector antennas, in particular, primary-focus ones, and has become feed candidate of the US SKA proposal and VLBI2010 project. There are also other feed candidates for SKA and VLBI2010 radio telescopes, e.g., the quasi self-complementary antenna [36] and the quad-ridged horn [37]. The quasi self-complementary antenna is also a log-periodic dual-dipole-like antenna, but it has a polarization that squints with frequency and no antenna hardware has yet been realized within or above C-band. The main drawback of the quad-ridged horn is that its beamwidth and phase center vary with frequency, leading to a low aperture efficiency compared to the Eleven feed [38].

As for a linearly-polarized Eleven antenna, traditionally, the shortest folded dipoles at the two array petals are connected by a set of transmission line. The same feed strategy applies on the dually-polarized version too, where two sets of transmission line go orthogonally over or under each other at the center, forming a so-called central network. This central network is complicated to model in an accurate way, and even often causes problems in terms of matching, manufacturing, mounting issues and so on. A new idea was consequently put forward - what if we remove the central network and then use a center puck (a picture of the center puck can be found in Figure 6.20) to connect the shortest folded dipoles with the subsequent components, thus making the Eleven feed a multiport configuration? In the following chapters, the performance of the multiport Eleven antennas for use in satellite terminals, radio telescopes and MIMO communications will be introduced and discussed. Prior to those, however, the orthogonal folded dipoles and log-periodic folded dipole arrays will be addressed.

1.2 Thesis Outline

I tried my best to present each chapter of this thesis as self-contained. Each chapter contains results and partial conclusions dedicated to it, so that interested readers can go through each chapter almost independent of the rest. The first 2 brief chapters are the introduction to the thesis topic and the basics of simulation and optimization technology used in this doctoral work, respectively. The following major chapters including my main contributions are as follows:

Chapter 3: Antennas with Wideband Performance

During recent years, the wideband antennas are among others being paid more attention to than before. The concepts and examples of conventional broadband and frequency independent antennas are briefly introduced.

My contribution in Chapter 3 includes the analysis and discussion of a novel dual-/wideband pattern-reconfigurable antenna based on the orthogonal folded dipoles (OFD), which are presented in Section 3.3.

Chapter 4: Log-Periodic Folded Dipole Array

The log-periodic antennas have been used for decades in a lot of wideband applications. There are many interesting and bizarre shapes, such as planar and wire log-periodic structures, planar and wire trapezoidal toothed log-periodic structures, log-periodic slots and so forth.

My contribution in Chapter 4 includes the numerical study of a new type of structure called log-periodic folded dipole array (LPFDA), and the comparison between its partly-scaled and fully-scaled versions, which are presented in Section 4.2.

Chapter 5: Multi-Port Eleven Antenna For Use In Satellite Communications Terminal

The Eleven antenna invented at Chalmers is a new wideband feed that can cover a decade bandwidth up to a largest frequency of within Ku-band so far. As reviewed in the last section of this chapter, a single-band circular Eleven antenna can further be combined with a choke horn to form a dual-band feed for use in satellite terminals. In addition, the multi-port configurations of Eleven antennas are versatile in various applications.

My contribution in Chapter 5 includes the numerical and experimental studies of a 4-port L-band Eleven antenna that is capable of performing monopulse tracking in two orthogonal planes with linear polarization, which are presented in Section 5.1 and 5.2.

Chapter 6: Wide Band Eleven Antennas As Feed For Radio Telescopes

In this chapter, 3 previous Eleven feeds for radio telescopes are reviewed, which are wideband models below 3 GHz, a decade wideband model over 1-10 GHz and an ultra wideband model above 10 GHz, respectively.

My contribution in Chapter 6, presented in Section 6.1 and 6.5, includes the numerical study of 3 triple bandwidth Eleven feed models, which consist of 8 folded dipoles in each petal and have single or dual polarization; additionally, a novel circular version of Eleven feed (also 8 folded dipoles in each petal) with improved BOR1 and therefore aperture efficiency for reflector antennas is reported.

Chapter 7: Multi-Port Eleven Antenna For Narrowband MIMO Applications

The fundamentals of narrowband radio channel are addressed in the beginning. The concept of diversity is subsequently examined as it is an important technique to mitigate the degradation of the signal quality due to the narrowband multipath fading. And then the reverberation chamber is introduced, which is capable of emulating an isotropic Rayleigh fading environment with acceptable accuracy.

My contribution in Chapter 7, presented in Section 7.4, includes the description of how to measure the MIMO performance of Eleven antennas with diversity ports in the reverberation chamber, and the analysis and discussion on the experimental results in terms of embedded element efficiency, diversity gain and maximum available capacity, etc.

Chapter 2

Basics of Simulation and Optimization Technology for This Thesis

2.1 Computational Electromagnetics

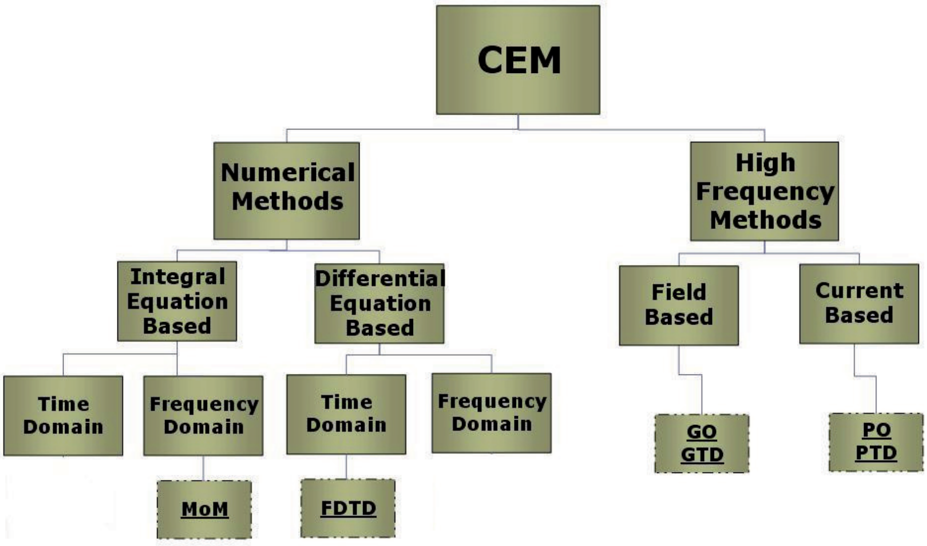
CEM
Numerical Methods
High Frequency Methods
Integral Equation Based
Differential Equation Based
Field Based
Current Based
Time Domain
Frequency Domain
Time Domain
Frequency Domain
GO
GTD
PO
PTD
MoM
FDTD

Figure 2.1: Categories within computational electromagnetics appeared in [3].

The theoretical foundation for analyzing any problem in macroscopic electromagnetism is the well known Maxwell's equations, which describe the properties of the electric and magnetic fields and relate them to the charge density and current density. The Maxwell's equations can be formulated in both differential and integral forms. Under various constitutive relations of media as well as boundary conditions, closed form solutions to Maxwell's equations can be feasible when dealing with regular geometries, e.g. a rectangular waveguide, a cylindrical coaxial cable or a spherical resonator, etc. In practice, however, many electromagnetic problems regarding irregular geometries are not analytically calculable. The inability to derive closed form solutions to Maxwell's equations in such scenarios can however be overcome by computational electromagnetics (CEM) techniques, which typically apply computationally efficient approximations to Maxwell's equations in order to calculate antenna performance, wave propagation, electromagnetic compatibility, radar cross section (RCS) and so on.

There are various ways to assort the techniques in CEM. In this chapter, I prefer applying the classification in [3], where the CEM for antennas are basically divided into two major categories: numerical methods and asymptotic high-frequency methods as shown in Figure 2.1. The numerical methods are used in the cases where the size of the antenna or scatterer is on the order of the wavelength to just a few tens of wavelengths. They are not suitable for even larger objects, e.g. an earth station reflector, because the rate of convergence of these techniques will generally become quite poor when dealing with such an electrically large antenna or scatter. On the other hand, the high-frequency methods are better suited to objects that are arbitrarily large in terms of wavelengths. In the following sections, I would like to briefly introduce two numerical methods, i.e., Method of Moments (MoM) and Finite Integration Techniques (FIT) , because both of them have been used for antenna simulations in my doctoral project.

2.1.1 Method of Moments

In order to understand the principle of MoM, it is preferable to start with a dipole as an example. Consider a metal (e.g. copper) cylindrical wire with radius a and length L ($a \ll L$) in free space. We let its center coincide with the center of a cylindrical coordinate system and make it vertical with the z-axis. We assume that the longitudinal currents are uniform and confined to the surface due to the skin effect, whereas the circumferential surface currents are negligible. The wire with such a uniform surface current density can be approximated as an equivalent filamentary line current source, $I(z')$, along the z-axis. The metal material is thus removed, making it possible to apply the free-space Green's function. The longitudinal scattered field due to $I(z')$ can be equated to the negative of the incident field, $E_z^i(z)$ (an observation point: (a, ϕ, z)), since the boundary condition holds at the cylindrical wire surface,

$$E_z^i(z) = -\frac{1}{j\omega\varepsilon_0}\int_{-L/2}^{L/2} I(z')[\frac{\partial^2\psi(z,z')}{\partial z^2} + \omega^2\mu_0\varepsilon_0\psi(z,z')]dz' \qquad (2.1)$$

where ω is the angular frequency, μ_0 and ε_0 are the permeability and permittivity in free space, respectively, and $\psi(z,z')$ is the free-space Green's function, which is the solution to the wave equation in connection with a point source at the origin. The equation (2.1) is the popular type of integral equation derived by Pocklington.

Point-Matching

For convenience, a more general expression of the Pocklington's formulation can be written as follows,

$$E_z^i(z) = -\int_{-L/2}^{L/2} I(z')K(z,z')dz' \tag{2.2}$$

where the kernel $K(z,z')$ depends on the specific integral equation formulation used. The unknown current $I(z')$ can be approximated by a series of known basis (or expansion) functions $B_n(z')$,

$$I(z') \approx \sum_{n=1}^{N} I_n B_n(z') \tag{2.3}$$

where I_n's are unknown expansion coefficients. Assume the wire is divided into N segments of length $\Delta z'_n$ and the basis functions are a set of orthogonal pulse functions, i.e. $B_n(z')$ is 1 within $\Delta z'_n$ but 0 otherwise, so substituting (2.3) into (2.2) will yield the following expression, where the subscript m on z_m indicates that the integral equation is enforced at segment m.

$$\begin{aligned} E_z^i(z_m) &\approx -\textstyle\int_{-L/2}^{L/2} \sum_{n=1}^{N} I_n B_n(z')K(z_m,z')dz' \\ &= \textstyle\sum_{n=1}^{N} I_n \{-\int_{\Delta z'_n} K(z_m,z')dz'\} \end{aligned} \tag{2.4}$$

Let $Z_{mn} = -\int_{\Delta z'_n} K(z_m,z')dz'$ and $V_m = E_z^i(z_m)$, then

$$V_m \approx \sum_{n=1}^{N} Z_{mn} I_n \tag{2.5}$$

which shows resemblance between the integral equation given in (2.1) and Kirchhoff's network equations. As (2.5) is only one equation in N unknowns, $(N-1)$ additional independant equations are needed to solve for the N unknowns. Point-matching is such a process, where we sucessively enforce the integral equation at N points (center of each segment) on the axis of the wire so that we have a different Z_m for each equation. Point-matching at N points results in the following system of equations in matrix form,

$$\begin{bmatrix} Z_{11} & Z_{12} & \dots & Z_{1N} \\ Z_{21} & Z_{22} & \dots & Z_{2N} \\ \cdot & \cdot & \cdot & \\ \cdot & \cdot & \cdot & \\ \cdot & \cdot & \cdot & \\ Z_{N1} & Z_{N2} & \dots & Z_{NN} \end{bmatrix} \begin{bmatrix} I_1 \\ I_2 \\ \cdot \\ \cdot \\ \cdot \\ I_N \end{bmatrix} \approx \begin{bmatrix} E_z^i(z_1) \\ E_z^i(z_2) \\ \cdot \\ \cdot \\ \cdot \\ E_z^i(z_N) \end{bmatrix} \tag{2.6}$$

or in the compact notation as

$$[Z_{mn}][I_n] \approx [V_m] \tag{2.7}$$

where $[Z_{mn}]$, $[I_n]$ and $[V_m]$ are referred to as generalized impedance, current and voltage matrices, respectively; note their units need not necessarily be ohms, amperes and volts. If N approaches infinity, the above approximations will become equalities. In practice, however, N is chosen to be sufficiently large in order to obtain accurate solutions for the current distribution.

According to [3], there are three typical methods to model the source. Concerning the case of an incident plane wave at a receiving antenna or scatterer, we need the tangential component of the known incident field at the match points along the axis of the wire dipole, in order to obtain the elements in $[V_m]$. For transmitting antennas, the delta gap source and frill source are usually applied. The former assumes an excitation voltage V_A is placed across the small gap (width: δ) at the center of the dipole, giving rise to an impressed field $E^i = V_A/\delta = V_m$. The latter assumes a purely dominant mode distribution (TEM) in the aperture of a coaxial cable that feeds a monopole, and through imaging the ground plane the aperture can be replaced with a frill of magnetic current. The elements in $[V_m]$ can readily be calculated once the source is modeled. After $[I_n]$ is found by using (2.3) and $[V_m]$ is calculated based on source modeling, we can proceed to determine impedance, radiation patterns, the radar cross section and so on.

Weighted Residuals

In the previous dipole example, the method of point-matching can only guarantee the boundary condition at the match points, i.e., the centers of all N segments; so the point-matching procedure can be viewed as a relaxation of the boundary condition such that it is only satisfied at specific points. To improve the accuracy, we look into a residual R, which is the sum of the tangential components of the scattered and incident fields. Based on (2.4), we have

$$R(z) = \sum_{n=1}^{N} I_n \{ \int_{\Delta z'_n} K(z, z') dz' \} + E_z^i(z) \tag{2.8}$$

By introducing a weighting (or testing) function $W_m(z)$, we force the residual to zero in a weighted average sense

$$\int W_m(z)R(z)dz = 0 \qquad m = 0, 1, 2...N \tag{2.9}$$

Substituting (2.8) into (2.9) leads to, ($m = 0, 1, 2...N$)

$$\int_{-L/2}^{L/2} W_m(z)\sum_{n=1}^{N} I_n\{\int_{\Delta z'_n} K(z,z')dz'\}dz + \int_{-L/2}^{L/2} W_m(z)E_z^i(z)dz = 0 \tag{2.10}$$

If the weighting functions are Dirac delta functions, i.e. $W_m(z) = \delta(z - z_m)$, then (2.10) reduces to (2.4). If the weighting functions are the pulse functions, i.e. $W_m(z)$ is 1 within Δz_m but 0 otherwise, then (2.10) becomes as follows,

$$\sum_{n=1}^{N} I_n \int_{\Delta z_m}\{\int_{\Delta z'_n} K(z,z')dz'\}dz + \int_{\Delta z_m} E_z^i(z)dz = 0 \qquad m = 0, 1, 2...N \tag{2.11}$$

Let $Z_{mn} = \int_{\Delta z_m}\{\int_{\Delta z'_n} K(z,z')dz'\}dz$ and $V_m = \int_{\Delta z_m} E_z^i(z)dz$, then (2.11) will turn to a compact form involving the generalized impedance, current and voltage, which bears an analogy to (2.5)-(2.7).

The process of expanding the unknown current in a series of basis functions and setting up N equations in N unknown using the weighted residual method is more commonly referred to as the method of moments [39] [40]. If the weighting functions are Dirac delta functions, the specific MoM procedure is called point-matching; if the weighting functions are the same as the basis functions, e.g. the pulse functions, then it is known as Galerkin's method. The above example is a pulse-pulse Galerkin formulation. Other formulations that are useful include:
⋆ Triangle (or piecewise linear) Galerkin formulation used in $MININEC\ Pro$ thin wire code [41];
⋆ Piecewise sinusoidal Galerkin formulation by Richmond [42];
⋆ Sinusoidal interpolation - delta formulation used in NEC program [43];
⋆ RWG (Rao-Wilton-Glisson) Galerkin formulation on triangle surface meshes used in $FEKO$ [44] [45];
⋆ Higher Order Basis Functions (HOBFs) on a quad mesh regarded as the foundation of $WIPL\text{-}D$ EM solver [46].

In this section, MoM has been interpreted using an approach that takes advantage of Kirchhoff's network equations. Other alternative approaches to MoM, such as reaction formulation and linear algebra formulation, can in addition be found in the literature [40] [47] [48]. We do not want to dig much into this subject here, as it is beyond the scope of this chapter.

2.1.2 Finite Integration Technique

$CST\ STUDIO\ SUITE^{TM}$ is a general-purpose EM solver based on the Finite Integration Technique (FIT), which was first proposed by Weiland in 1977 [49]. FIT discretizes the following integral form of Maxwell's equations rather than the differential ones:

$$\oint_{\partial A} \vec{E} \cdot d\vec{l} = -\iint_A \frac{\partial \vec{B}}{\partial t} \cdot d\vec{A} \tag{2.12}$$

$$\oint_{\partial A} \vec{H} \cdot d\vec{l} = \iint_A (\frac{\partial \vec{D}}{\partial t} + \vec{J}) \cdot d\vec{A} \tag{2.13}$$

$$\iint_{\partial V} \vec{D} \cdot d\vec{A} = \iiint_V \rho \, dV \tag{2.14}$$

$$\iint_{\partial V} \vec{B} \cdot d\vec{A} = 0 \tag{2.15}$$

where ∂A is the closed line boundary of a surface A, while ∂V is the closed surface boundary of a volume V. All of the four equations stem from the corresponding Maxwell's equations in differential form. The first two equations are manipulated by using Stokes' theorem, while the last two by Gauss' divergence theorem. To solve these equations numerically, a finite calculation domain must be defined, enclosing the application problem in question. Then a suitable mesh system splits the domain down into small grid cells. For simplicity, we first exemplify the orthogonal hexahedral grid system in the following.

In Figure 2.2, the zoomed grey grid is called the primary grid G and it can be visualized in CST. A second blue grid, called the dual grid $\tilde{G}$, is internally set up orthogonally to the first one. The spatial discretization of Maxwell's equations is finally performed on these two orthogonal grids, where the electric grid voltage *e* and magnetic facet flux *b* are defined on G, while the dielectric facet flux *d* and magnetic grid voltage *h* are allocated on $\tilde{G}$. First, we formulate Faraday's law (Equation (2.12)) for each of the primary grid facets separately. Regarding a grid facet A_n, the closed integral on the left side of (2.12) can be rewritten as a sum of four grid voltages, while the right side of (2.12) is represented by the time derivative of the magnetic flux

$$e_i + e_j - e_k - e_l = -\frac{d}{dt} b_n \tag{2.16}$$

Repeating this procedure for all available grid facets summarizes the calculation rule in a matrix formulation, introducing a topological matrix **C** as the discrete equivalent of the

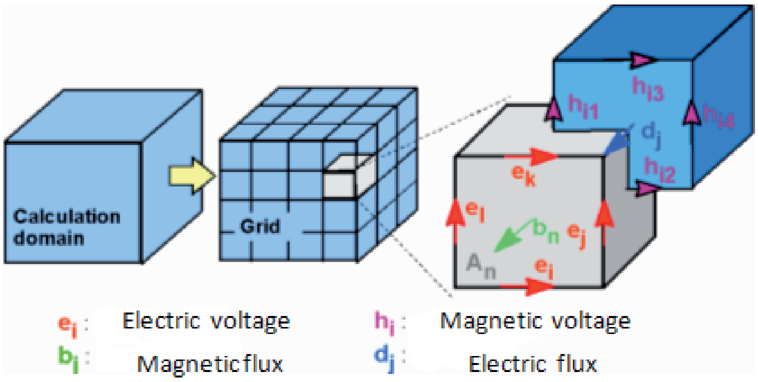

Figure 2.2: The orthogonal hexahedral grid system used in CST. Courtesy of [4].

analytical curl operator:

$$\mathbf{C}\mathbf{e} = -\frac{d}{dt}\mathbf{b} \tag{2.17}$$

Applying this scheme to Ampere's law (Equation (2.13)) on the dual grid leads to the definition of a corresponding dual discrete curl operator $\tilde{\mathbf{C}}$. Similarly, the discretization of the last two divergence equations on the primary and dual grids, gives rise to discrete divergence operators $\mathbf{S}$ and $\tilde{\mathbf{S}}$, respectively. Composed of elements '0' and '±1', all of these discrete operators represent merely topological information. Moreover, analogue to the continuous form of Maxwell's equations, they follow:

$$\begin{aligned} \mathbf{S}\mathbf{C} = \tilde{\mathbf{S}}\tilde{\mathbf{C}} = 0 \quad &\Longleftrightarrow \quad \nabla \cdot \nabla \times (vector) \equiv 0 \\ \mathbf{C}\tilde{\mathbf{S}}^T = \tilde{\mathbf{C}}\mathbf{S}^T = 0 \quad &\Longleftrightarrow \quad \nabla \times \nabla (scalar) \equiv 0 \end{aligned} \tag{2.18}$$

Now we have the complete discrete equivalents of Maxwell's equations, which are known as Maxwell's Grid Equations (MGEs) [49]:

$$\mathbf{C}\mathbf{e} = -\frac{d}{dt}\mathbf{b} \qquad \tilde{\mathbf{C}}\mathbf{h} = \frac{d}{dt}\mathbf{d} + \mathbf{j} \qquad \tilde{\mathbf{S}}\mathbf{d} = \mathbf{q} \qquad \mathbf{S}\mathbf{b} = 0 \tag{2.19}$$

This description is so far an exact representation of Maxwell's equations, and does not contain any approximation errors. It can be shown that the FIT formulation is not affected by the spatial discretization, since the set of MEGs maintain energy and charge conservation [50].

However, the missing material relations introduce inevitable numerical inaccuracy due to spatial discretization. To find out the relations between voltages (**e**, **h**) and fluxes (**d**, **b**, **j**), their integral values have to be approximated over the grid edges and areas, respectively. The resulting coefficients, summarized as follows, depend on the averaged material parameters as well as on the spatial resolution of the grid.

$$\begin{aligned}&\mathbf{d} = \mathbf{M}_\epsilon \mathbf{e} \quad \Longleftrightarrow \quad \vec{D} = \epsilon \vec{E}\\ &\mathbf{b} = \mathbf{M}_\mu \mathbf{h} \quad \Longleftrightarrow \quad \vec{B} = \mu \vec{H}\\ &\mathbf{j} = \mathbf{M}_\sigma \mathbf{e} + \mathbf{j}_s \quad \Longleftrightarrow \quad \vec{J} = \sigma \vec{E} + \vec{J}_s\end{aligned} \tag{2.20}$$

Now we obtain all matrix equations that are available to solve electromagnetic field problems on the domain discretized by hexahedral grids. These matrices have diagonal form and contain unavoidable approximations of any numerical procedure. The boundary of the calculation domain is assumed to be ideal electric, magnetic or open. On the occasion of open boundary, a perfect matched layer (PML) is wrapped around the structure to absorb incident waves at the boundary [51]. It should be noted that FIT can also be applied to more general mesh types such as tetrahedral grids and irregular grids (subgrids), which can be seen as an extension to the basic method outlined above [52].

FIT provides a universal spatial discretization scheme applicable to various electromagnetic problems ranging from static field calculation to high frequency applications in time or frequency domain. 6 EM solver products dedicated to different applications and 2 versatile solvers for mechnical/thermal analysis and circuit simulation/synthesis are currently available within CST (version 2010) [4], among which CST Microwave Studio (MWS) is frequently used in our work on antennas, etc. CST MWS includes three types of solvers: transient solver, frequency domain solver and eigenmode solver. The following is to give brief information to the transient solver, which in particular is most often used in our simulations.

The transient solver allows the simulation of a structure's behavior in a wide frequency range in just a single computation run, and it is especially efficient for devices with open boundaries or large dimensions. The transient solver is based on the solution of the discretized set of MGEs. Substituting the time derivatives by central differences yields explicit update formulation for the loss-free case [4]:

$$\begin{aligned}&\mathbf{e}^{n+\frac{1}{2}} = \mathbf{e}^{n-\frac{1}{2}} + \Delta t \mathbf{M}_\epsilon^{-1}[\tilde{\mathbf{C}}\mathbf{M}_\mu^{-1}\mathbf{b}^n - \mathbf{j}^n]\\ &\mathbf{b}^{n+1} = \mathbf{b}^n - \Delta t \mathbf{C}\mathbf{e}^{n+\frac{1}{2}}\end{aligned} \tag{2.21}$$

This is known as the so-called leap-frog algorithm. As illustrated in Figure 2.3, for instance, the magnetic flux at t=(n+1)Δt is computed from the magnetic flux at the previous time step t=nΔt and the electric voltage at t=(n+1/2)Δt.

Explicit time integrations are conditionally stable. The maximum stable time step inside

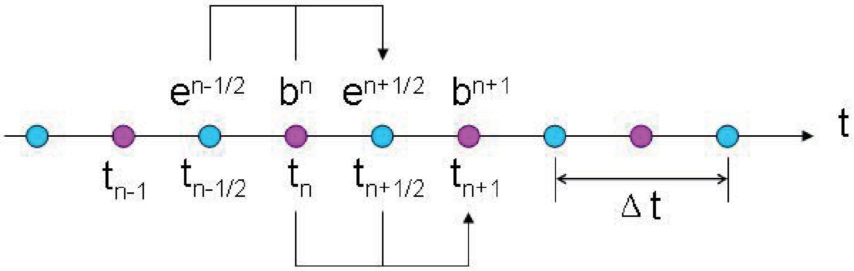

Figure 2.3: The leap-frog scheme for discretized set of MGEs.

a grid cell is restricted by the Courant criterion

$$\Delta t \leq \frac{\sqrt{\epsilon\mu}}{\sqrt{(\frac{1}{\Delta x})^2 + (\frac{1}{\Delta y})^2 + (\frac{1}{\Delta z})^2}} \tag{2.22}$$

where Δx, Δy, Δz are the grid space increments in the x, y, z-directions.

In the case of Cartesian grids (unit cubes), the FIT formulation can be rewritten in time domain to yield standard Finite Difference Time Domain (FDTD) methods [4]. However, classical FDTD methods are limited to staircase approximations of complex boundaries. In contrast, the Perfect Boundary Approximation (PBA) technique [53] applied to the FIT algorithm maintains all the advantages of structured Cartesian grids while allowing accurate modeling of curved structures. PBA takes into account the thickness of metallic sheets or strip lines within one grid cell, without explicitly meshing it. The consideration of field singularities of EM waves on edges further reduces the number of mesh points necessary to reach a precise field and impedance computation.

2.2 Optimization Methods

CST MWS offers a Parameter-Sweep function to perform several simulations with different structure parameter values. For each simulation, previously specified results (e.g. reflection coefficient) can be stored, and after the simulations finish, one can plot these results in relation to their parameters. Besides, a built-in optimizer is used to find optimal parameter settings for the modeled structure. There are two classical types of optimizers currently available in CST MWS: the Interpolated Quasi Newton optimizer and the Classic Powell optimizer.

The complexity of the optimization process will increase drastically in cases where the number of parameters defining an antenna structure becomes large. A few advanced optimization methods have thus been developed as the requirements increase. Paralleled with optimization methods such as hill-climbing, simulated annealing, swarm particle optimization, systematic search algorithm, the genetic algorithm provides an alternative to traditional optimization techniques by using directed random searches to locate optimal solutions in many problems.

2.2.1 Genetic Algorithms

During the past two decades, genetic algorithms (GA's) have emerged as practical optimization and search methods in a variety of areas such as electromagnetics, microelectronics, economic strategy planning, music generation, machine learning, etc [54]. GA's (along with Monte Carlo and simulated annealing techniques, etc.) belong to a special class of global optimizers which are stochastic in nature and therefore less prone to converge to a weak local optimum than deterministic optimization methods [55].

The application of modem electromagnetic theory to radiation and scattering problems often requires the use of optimization. Electromagnetic optimization problems generally involve a large number of parameters. The parameters can be either continuous, discrete, or both, and often include constraints in allowable values. The goal of the optimization is to find a solution that represents a global maximum or minimum. Genetic Algorithm optimizers are robust, stochastic search methods rooted in the biological mechanisms of natural selection and evolution. While perhaps not always the best method for attacking an optimization, GA's have the distinct advantage that they tend to produce globally optimal results without requiring a great deal of information about the solution domain; they are particularly useful when applied to problems that are highly constrained, or have discretized parameter sets that cause problems for the local techniques. GA's should be among the first methods considered when faced with a new electromagnetic optimization problem [56].

In the following, we will look into a basic structure of Genetic Algorithms.

GA's are implemented in a computer simulation, where a population of abstract representations (called chromosomes) of candidate solutions (called individuals) to an optimization problem evolves toward better solutions. The evolution usually starts from a population of randomly generated individuals and happens in generations. In each generation, the fitness of every individual in the population is evaluated by a fitness function. The fitness function is problem dependent and defined over the genetic representation, and it measures the quality of the represented solution. Individual solutions are selected through a fitness-based process, where fitter solutions as measured by a fitness function are typically more likely to be selected. The next generation from those selected is formed through crossover (also called recombination) and/or mutation. The new population is then used in the next iteration of the algorithm. The algorithm commonly terminates when either a maximum number of generations has been produced, or a satisfactory fitness level has been reached for the population. If the algorithm has terminated due to a maximum number of generations, a satisfactory solution may or may not have been reached.

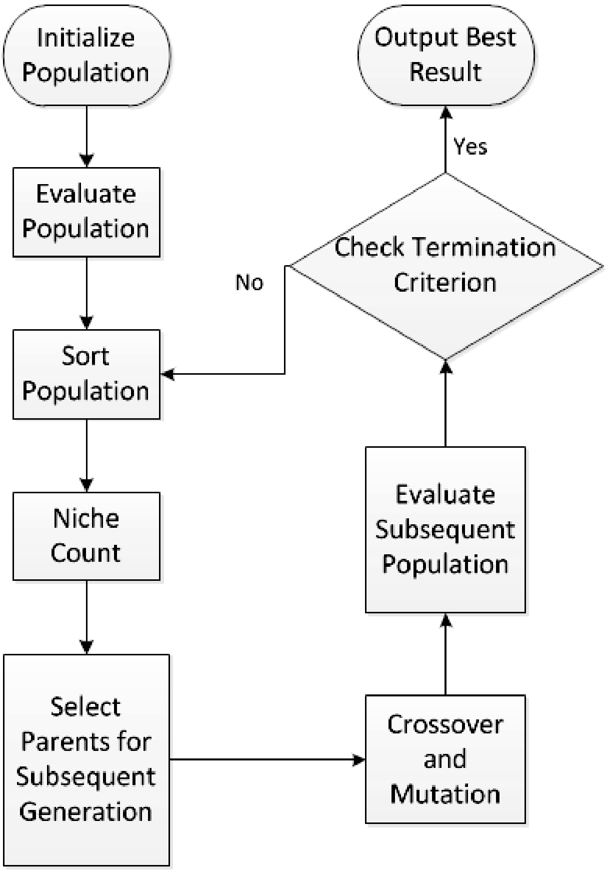
Initialize Population
Evaluate Population
Sort Population
Niche Count
Select Parents for Subsequent Generation
Crossover and Mutation
Evaluate Subsequent Population
Check Termination Criterion
No
Yes
Output Best Result

Figure 2.4: Basic Genetic Algorithm Structure.

The structure of our in-house program based on a basic genetic algorithm is illustrated in Figure 2.4. An objective function must be determined beforehand, which provides a mechanism for evaluating each potential solution. This function contains one or more than one objective to be optimized; e.g., it can either aim to optimize only the return loss or aim to optimize both the return loss and the cross-polar level of an antenna. For simplicity, we take optimization for only the return loss, which determines the impedance bandwidth, as an example here.

First of all, a population of potential solutions to an optimization or search problem, interpreted as sets of chromosomes, is randomly or empirically initialized. The chromosomes can, but not necessarily, be encoded as strings of binary bits (0s and 1s), and in any cases the encoding mechanism should map each set of chromosome to a unique binary string.

An EM field solver, e.g. CST, is needed to calculate the return loss of antenna structures defined by each set of chromosomes. When the simulation finishes, the population is sorted for the first time by the total number of points within the interested frequency range, on which the return loss is better than a preferred threshold, e.g. -10 dB.

A niche count function works to provide fitness values related to the sum of differences (within the predefined niche deviation) between any set of chromosomes and all the others. The fitness value is usually normalized in a convenient range of 0 to 1. When the niche count finishes, the population is sorted for the second time according to the calculated fitness values.

A selection mechanism picks up fitter sets of chromosomes to survive, as each set is associated with a fitness value that reflects how good it is and compared with others in the population. The higher the fitness value of an individual, the higher its chance of survival in the subsequent generation. The proportionate selection scheme is implemented by using a roulette wheel. Each set of chromosomes, with a normalized fitness value f_i, is allocated a sector of a roulette wheel with an angle subtended by $2\pi f_i$. A set of chromosomes is selected as parent if a randomly generated number $2\pi * rand$ (*rand* is in the range from 0 to 1) falls in the corresponding sector.

A crossover function comes after all the parents have been selected and the number of parents is usually half the population. The crossover algorithm is not always effected since it is invoked only if a random number (between 0 and 1) is greater than a predefined probability of crossover; otherwise the sets of chromosomes remain unaltered. The crossover is realized through exchange and recombination of portions between different sets of chromosomes. After crossover, a pair of parents have a pair of children who inherit transmitted genes from both parents.

Another mechanism called mutation comes next, which can cause random alteration of the chromosomes and regenerate lost genetic materials. The probability of mutation determines how probable a random set of chromosomes changes into something different from the genes of their parents.

The evolution procedure will be repeated until the termination criterion, i.e. the maximum number of generations, is met.

Chapter 3

Antennas with Wideband Performance

During recent years there has been a growing interest to move from narrowband communication systems to wideband systems, in a variety of different applications. The wideband antennas are among others being paid more attention to than before. The concepts and examples of conventional broadband and frequency independent antennas are briefly introduced in the first two sections. In the third section, the analysis of a dual-/wide-band pattern-reconfigurable antenna based on orthogonal folded dipoles is presented.

3.1 Background of Broadband Antennas

An antenna is in many applications demanded to operate over a broad range of frequencies. The term "broadband" is actually a relative measure of the bandwidth of the antenna, which can be computed in two ways. The bandwidth of a narrow band antenna is usually specified as a percent of the center frequency, whereas the bandwidth of a broadband antenna is expressed as a ratio between the upper-edge and the lower-edge frequencies. If the impedance and the radiation pattern of an antenna do not change significantly over about an octave (2:1) or more, we will classify it as a broadband antenna [57].

3.1.1 Traveling Wave Antennas

A traveling wave or nonresonant antenna is one on which the reflected wave is not strongly present. In general, there are two types of traveling wave antennas.

The first type is a surface-wave antenna defined as "an antenna which radiates power flow from discontinuities in the structure that interrupt a bound wave on the antenna surface" [57]. In general, a surface wave antenna is a slow wave structure on which the phase velocity of the traveling wave is equal to or less than the velocity of light in free space. The simplest form of this type is the Beverage antenna, which is a long (usually 2 to 10 wavelengths) and straight wire horizontally over an imperfect ground plane (earth), terminated with a matched load at the end. The distance between the wire and the ground is only a small fraction of wavelength. The input impedance is 200 to 300 Ω, and the load resistor can be adjusted in order to minimize, if not completely eliminate, reflections. It is usually used from 0.3 to 30 MHz, and more as a receiving rather than a transmitting antenna because of its poor radiation efficiency due to power dissipated in the resistive load and in the imperfect ground. The incident plane wave at an oblique angle produces a horizontal component of the E-field that is not completely shorted out by the earth ground. And it is this horizontal component that can induce a current on the long wire. From an alternative point of view, the Beverage antenna and its image in the earth can be considered as an unbalanced transmission line with unequal currents. As a matter of fact, unbalanced transmission lines can radiate.

The second type is a leaky-wave antenna defined as "an antenna that couples power in small increments per unit length, either continuously or discretely, from a traveling wave structure to free space"[57]. Most of the leaky-wave antennas are fast wave structures whose phase velocity of the traveling wave is greater than the velocity of light in free space. One typical example is a match-loaded rectangular waveguide with straight longitudinal slots offset from the centerline of the upper wall. The slots can be viewed as a periodic perturbation of the transmission line and cause a change in the propagation constant along the line.

3.1.2 Helical Antennas

The helical antenna, or helix for short, can operate in two principal modes, i.e. the normal (broadside) and the axial (endfire) modes. When the dimensions of a helix is small compared to the wavelength λ, it will work in the normal mode. The radiation pattern is similar to that of a small dipole or circular loop, and has its maximum in a direction normal to the helix axis. However, the input impedance of normal mode helix is very sensitive to changes of frequency; the bandwidth is therefore very narrow.

The axial mode occurs when the circumference is on the order of a wavelength. To obtain circular polarization in the major lobe with its maximum along the helix axis, it is required that the ratio between the circumference and the wavelength is within the range from 3/4 to 4/3 [3] [57], which gives a bandwidth radio of $16/9 : 1 \approx 1.78 : 1$, greater than that in the previous normal mode. The sense of the circular polarization is determined by the sense of the windings, and the purity of the circular polarization increases with the number of turns.

3.1.3 Biconical Antennas

The bandwidth of a wired dipole can be improved by using thicker wires. This simple idea can be extended to achieve broadband characteristics. An infinite biconical antenna is formed by placing two cones of infinite extent together, which can be viewed as that two wires in a dipole are flared smoothly with a fixed angle into infinity. Assuming that the cones are oriented along the z-axis, it can be proved that the radiation field contains only E_θ component (TEM mode), and the pattern varies as $1/sin\theta$ in the space of propagation. The input impedance is real and only related to the cone angle, regardless of the changing frequency.

A practical form is a finite biconical antenna. Reflections will occur at the ends of the finite cones, resulting in standing waves that lead to a complex input impedance. However, as the cone angle increases (while the height of the cone holds constant), both the real and imaginary parts of the input impedance become less sensitive to frequency. One alternative of the finite biconical antenna is a discone, i.e., a finite cone over a disk-shaped ground plane. It can offer acceptable impedance and radiation properties over a frequency range up to several octaves. Another practical alternative is the planar version, the so-called "bow-tie" antenna. It is advantageous in terms of weight and cost, but its impedance is more sensitive to frequency.

3.2 Background of Frequency Independent Antennas

3.2.1 Principles

An antenna with bandwidth as great as 10:1 or even more are referred to as a "frequency independent" antenna [3]. Lots of research has been done to find out what characteristics result in the broadband or frequency independent property.

First of all, the shape of the antenna should be specified more by angles than by lengths. Helical and spiral antennas are such examples that attempt to avoid any element with fixed physical length. Second, fatter antennas give wider bandwidths. As mentioned earlier, a resonant dipole can be improved in terms of bandwidth as its wire diameter increases, though its operational center frequency may be lower afterwards. Biconical antennas are both fat and angle-independent versions of the common wired dipole. Third, self-complementary structures are found to behave independent of frequency. A self-complementary antenna is one whose complement and itself are identical, but for a possible rotation. Complementary antennas are similar to a positive and negative in photography. A typical example is a slot antenna and its complement, the ribbon dipole. The Babinet's principle for optics can be extended to electromagnetics, and it leads to that the product of the impedances of two complementary antennas is a constant $\eta^2/4$ (η is the wave impedance, valued $120\pi\ \Omega$ in free space). Regarding a self-complementary antenna, the input impedance should be $\eta/2$ (valued $60\pi \approx 188.5\ \Omega$). However, many antennas that are not self-complementary, e.g. log-periodic dipole arrays, still have acceptable impedance variations with frequency in common applications.

In a strict sense, the frequency independent antenna must have constant impedance, pattern, polarization and phase center with frequency. Although no antennas meet these criteria in reality, it is of interest to study the analytical treatment of the frequency independent antenna. Assume that an antenna is best described by the spherical coordinates (r, θ, ϕ), and its surface (or edge) can be defined as an arbitrary function, $r = F(\theta, \phi)$, where r represents the distance between the origin and the surface. If the antenna is scaled to a frequency that is K times lower than the original frequency, its surface must be correspondingly enlarged K times to maintain the same electrical dimensions. Then the new surface becomes $r' = KF(\theta, \phi)$. The new and the original surfaces should be identical to each other, because such a physical congruence implies that the original antenna electrically would behave the same at both frequencies. In other words, if an antenna can be transformed into a scaled version of itself by means of rotation and/or translation, it will yield frequency independent performances. Since both translation and rotation in θ are prohibited [57], this congruence can only be realized by rotation in ϕ by an angle C (C depends on K but neither on θ nor on ϕ), i.e., $F(\theta, \phi + C) = KF(\theta, \phi)$. It has been further derived in [57] that the surface must then satisfy

$$r = F(\theta, \phi) = f(\theta) \cdot e^{\frac{\phi}{K}\frac{dK}{dC}} = f(\theta) \cdot e^{a\phi} \tag{3.1}$$

where $f(\theta)$ is a totally arbitrary function, and a is the flare rate.

3.2.2 Spiral Antennas

In general, equation (3.1) is applicable to any antenna with a three-dimensional structure. First we consider the case of a two-dimensional structure, assuming that the antenna is placed in the xy-plane, where $\theta=\pi/2$. If $f(\theta)$ in equation (3.1) is,

$$f(\theta) = \begin{cases} r_0 & \theta = \pi/2; \\ 0 & \text{otherwise} \end{cases} \tag{3.2}$$

where r_0 is a constant. Then equation (3.1) can thus be reduced to

$$r|_{\theta=\frac{\pi}{2}} = r_0 \cdot e^{a\phi} \tag{3.3}$$

where $r = 0$ when θ is different from $\pi/2$. This curve is called an equiangular spiral, and it can be used to create a self-complementary planar equiangular spiral antenna. Since no practical structure is made completely self-complementary due to truncations at the feed and far out, the impedance, pattern and polarization of the self-complementary planar equiangular spiral antenna remain nearly constant over a wide frequency band. The lower-end frequency is determined by the overall radius (or circumference), while the upper-end frequency by the truncation of the spiral and the feed structure at the vertex. It has two wide radiation beams normal to the plane of the spiral (bidirectional radiation) and the polarization is close to circular over wide angles, whose sense is determined by the sense of the flare of the spiral.

Next we consider the case of a three-dimensional structure by generalizing the geometry regarding the previous planar equiangular spiral. If $f(\theta)$ in equation (3.1) is,

$$f(\theta) = \begin{cases} r_0 & \theta = \beta; \\ 0 & \text{otherwise} \end{cases} \tag{3.4}$$

where β is a constant and allowed to take any value between 0 and π. Then equation (3.1) becomes

$$r|_{\theta=\beta} = r_0 \cdot e^{a\phi} \tag{3.5}$$

which describes a spiral wrapped on a conical surface. This three-dimensional spiral, called conical spiral, can provide a single lobe, instead of bidirectional radiation, towards the apex of the cone with the maximum along the axis, while the circular polarization and nearly constant impedance are preserved over wide bandwidths.

3.3 Folded Dipole Antennas

3.3.1 Two-Port Wired Folded Dipole

Folded dipoles are usually introduced in antenna literature as providing a way of matching twin-lead transmission lines with about 300 Ω characteristic impedance, and they are widely used in FM/TV broadcast reception and as feed for Yagi-Uda arrays and other popular antennas [3][57] .

As shown in Figure 3.1 (right), a one-port folded dipole consists of two parallel wired dipoles connected at both ends forming a narrow loop. A classical transmission-line/antenna model for analysis of a folded dipole antenna was originally put forward in [58]. This analytical model gives computationally efficient and accurate result for calculating the input impedance, provided the inter-element spacing s is very small compared with the wavelength λ, usually $s<0.05\lambda$.

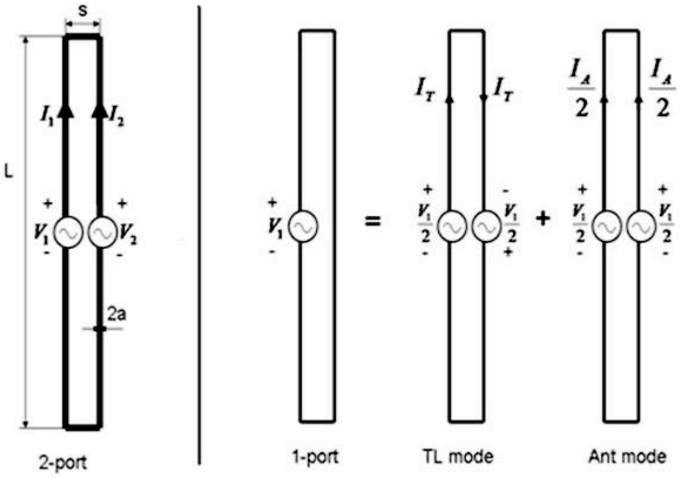

Figure 3.1: 2-port (left) and 1-port (right) folded dipole. Note: the current amplitudes denoted in the figure are close to the corresponding feed nodes.

A folded dipole can also be modeled as a two-port device, as depicted in Figure 3.1 (left). We hereby attempt to derive the admittance matrix of this two-port network model based on the classical method, i.e. superposition of both transmission line and antenna modes. First, it is still the case that the impedance for the transmission line mode Z_t is associated with a short-circuited lossless transmission line,

$$Z_t = jZ_0 \tan(\frac{\beta L}{2}) \tag{3.6}$$

where Z_0 is the characteristic impedance of the two-wire transmission line [57],

$$Z_0 = 120 \ln(\frac{\frac{s}{2} + \sqrt{(\frac{s}{2})^2 - a^2}}{a}) \tag{3.7}$$

The impedance for the antenna mode Z_d is that of a cylindrical dipole with an effective radius a_e, which is expressed as [57],

$$a_e = \sqrt{a \cdot s} \tag{3.8}$$

Z_d can be found through known methods such as the Moment Method. Similar to the model of the classical one-port folded dipole, the following current-voltage equations system can thus be set up for the two-port folded dipole,

$$I_1 = Y_{11}V_1 + Y_{12}V_2 \tag{3.9}$$

$$I_2 = Y_{21}V_1 + Y_{22}V_2 \tag{3.10}$$

Admittances Y_{11} and Y_{21} can be found when port 2 is shorted, i.e. V_2=0,

$$Y_{11} = \frac{I_1}{V_1}\Big|_{V_2=0} = \frac{\frac{I_A}{2} + I_T}{V_1} = \frac{\frac{V_1}{2\cdot 2Z_d} + \frac{V_1}{2Z_t}}{V_1} = \frac{Z_t + 2Z_d}{4Z_tZ_d} \tag{3.11}$$

$$Y_{21} = \frac{I_2}{V_1}\Big|_{V_2=0} = \frac{\frac{I_A}{2} - I_T}{V_1} = \frac{\frac{V_1}{2\cdot 2Z_d} - \frac{V_1}{2Z_t}}{V_1} = \frac{Z_t - 2Z_d}{4Z_tZ_d} \tag{3.12}$$

According to the reciprocity theorem, we have Y_{21}=Y_{12}; and due to the symmetry, we have Y_{11}=Y_{22}. Now the overall admittance matrix can be expressed as follows:

$$Y = \begin{bmatrix} \frac{Z_t+2Z_d}{4Z_tZ_d} & \frac{Z_t-2Z_d}{4Z_tZ_d} \\ \frac{Z_t-2Z_d}{4Z_tZ_d} & \frac{Z_t+2Z_d}{4Z_tZ_d} \end{bmatrix} \tag{3.13}$$

A special case occurs when port 2 is shorted, which is equivalent to an ordinary 1-port folded dipole. Its input impedance is the inverse of Y_{11},

$$Z_{in} = \frac{1}{Y_{11}} = \frac{4Z_tZ_d}{Z_t + 2Z_d} \tag{3.14}$$

3.3.2 Orthogonal Folded Dipoles

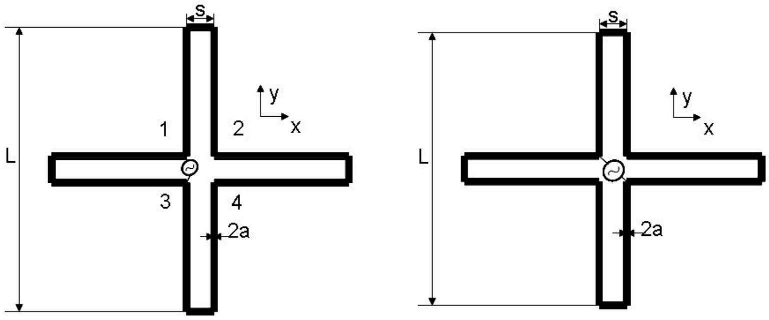

Figure 3.2: Dual-band (left) and wide-band (right) orthogonal folded dipoles

Two identical folded dipoles can be orthogonally connected and we hereinafter call them orthogonal folded dipoles (OFD) . One possible feeding scheme is illustrated in Figure 3.2 (left), in which the source (reference impedance: 300 Ω) crosses between nodes 1 and 3. In this case, which is referred to as the dual-band OFD, the shorted transmission line joined between nodes 2 and 4 can be thought of as a load, i.e. Z_2, at port 2. If the two-port model of a folded dipole is applied here, the voltage across the load is

$$V_2 = -I_2Z_2 = -jI_2Z_0\tan(\frac{\beta L}{2}) \tag{3.15}$$

By substitution, equations (3.9) and (3.10) can accordingly be developed to

$$I_1 = Y_{11}V_1 - jI_2Z_0\tan(\frac{\beta L}{2})Y_{12} \tag{3.16}$$

$$I_2 = Y_{21}V_1 - jI_2Z_0\tan(\frac{\beta L}{2})Y_{22} \tag{3.17}$$

We eliminate I_2 by combining the two equations, and then derive

$$\frac{I_1}{V_1} = Y_{11} - j\frac{Y_{12}Y_{21}Z_0\tan(\frac{\beta L}{2})}{1 + jY_{22}Z_0\tan(\frac{\beta L}{2})} \tag{3.18}$$

The total input admittance of the dual-band OFD is the sum of the above admittance and the admittance of a shorted transmission line joined at nodes 1 and 3,

$$Y_{in,dual} = Y_{11} - j\frac{Y_{12}Y_{21}Z_0\tan(\frac{\beta L}{2})}{1 + jY_{22}Z_0\tan(\frac{\beta L}{2})} + \frac{1}{jZ_0\tan(\frac{\beta L}{2})} \tag{3.19}$$

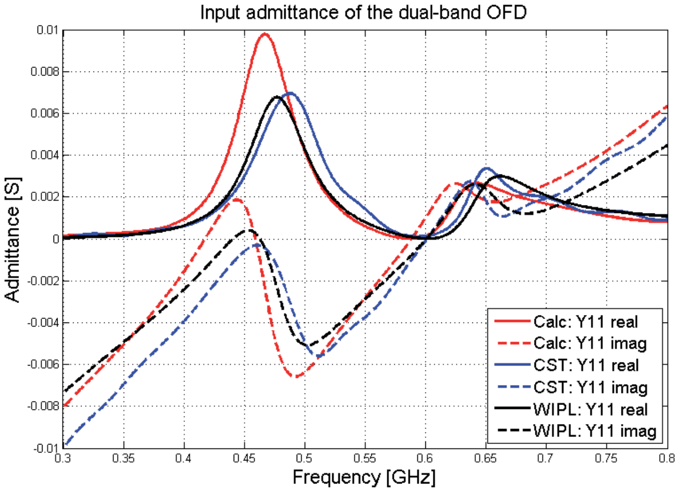

Figure 3.3: Input admittance of the dual-band OFD

We may start the verification with a practical dual-band OFD model, where *L* = 265 mm ($0.57\lambda_{0.65GHz}$), *a* = 1.53 mm ($0.0033\lambda_{0.65GHz}$), *s* = 5.1 mm ($0.011\lambda_{0.65GHz}$). The calculated (from 3.19) and the simulated (by both CST and WIPL-D) input admittances are compared in Figure 3.3. As can be seen, they agree quite well within the most of the displayed range. The discrepancies we believe are primarily due to the unaccounted mutual couplings between the vertical and horizontal arms. The corresponding S-parameters can be derived from the input admittances, and the magnitude curves are shown in Figure 3.4. It can be noticed from the matching properties that the dual-band OFD has two narrow bands around 0.45 and 0.65 GHz,

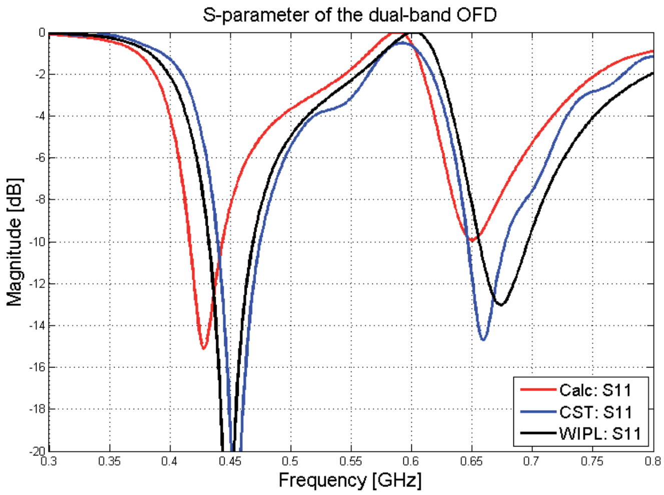

Figure 3.4: Calculated and simulated S_{11} of the dual-band OFD (reference: 300Ω)

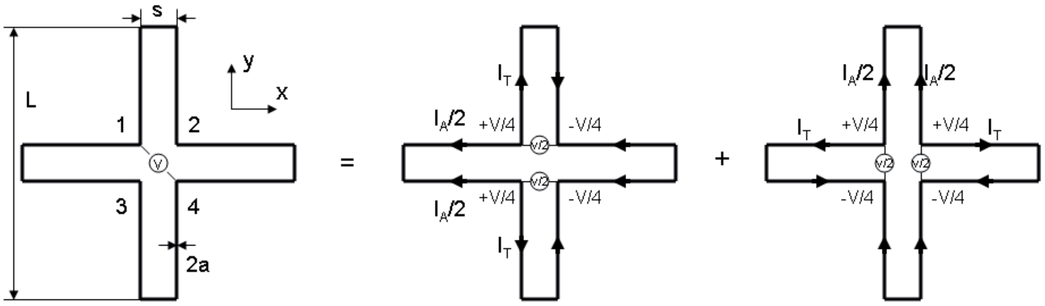

Figure 3.5: Wide-band OFD ($L = 265\ mm, a = 1.53\ mm, s = 5.1\ mm$) Note: the current amplitudes denoted in the figure are close to the corresponding feed nodes.

Another possible feeding scheme is illustrated in Figure 3.2 (right), where the source (also 300 Ω) crosses between nodes 1 and 4 of the antenna that is the same as before. We may hereinafter call this configuration wide-band OFD, instead. This configuration can be considered as superposition of two situations shown in Figure 3.5, where two identical voltage sources are placed between node 1-2 (V_{12}=+V/2), 3-4 (V_{34}=+V/2), and node 1-3 (V_{13}=+V/2), 2-4 (V_{24}=+V/2), respectively. The former excitation results in an antenna-mode current (I_A) only in the horizontal (x-oriented) folded dipole and a transmission-line-mode current (I_T) only in the vertical (y-oriented) folded dipole, provided the mutual coupling between the horizontal and vertical arms is neglected,

$$I_A = \frac{V}{2Z_d} \tag{3.20}$$

$$I_T = \frac{V}{2jZ_0 \tan(\frac{\beta L}{2})} \tag{3.21}$$

The expressions in (3.20) and (3.21) apply as well to the latter situation, where there is only I_T in the horizontal folded dipole and only I_A in the vertical folded dipole. By superposition it will end up with that the voltage at node 1, 2, 3, 4 becomes +V/2, 0, -V/2, 0, respectively, resulting in the total input admittance for the wide-band OFD,

$$Y_{in,wide} = \frac{2(\frac{I_A}{2} + I_T)}{V} = \frac{1}{2Z_d} + \frac{1}{jZ_0 \tan(\frac{\beta L}{2})} \tag{3.22}$$

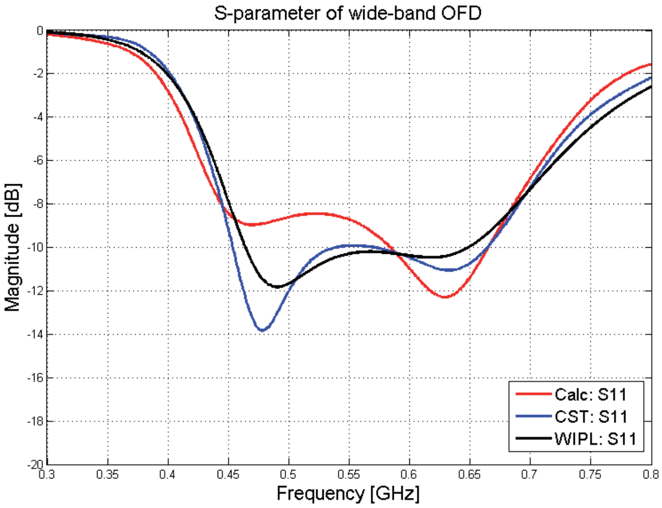

Figure 3.6: Calculated and simulated S_{11} of wide-band OFD (reference: 300 Ω)

Simulated and calculated (transformed from the input admittance w.r.t. 300 Ω reference) return loss curves (S_{11} magnitude) are plotted in Figure 3.6. As mentioned above, the dual-band OFD has two narrow bands around 0.45 and 0.65 GHz; however, the wide-band

OFD has a bandwidth approximately ranging from 0.45 to 0.66 GHz (corresponding to a relative bandwidth of 38$\%$, outperforming conventional wire folded dipoles). In spite of the disagreement from the simulation results, the calculated S_{11} curve of the wide-band OFD can indicate almost the same bandwidth as the simulated curves do. The disagreement is primarily due to the mutual coupling that is neglected in the derivation of (3.22). Especially, the three curves intersect at one frequency point around 0.58 GHz, where I_T in (3.21) will become zero. It implies that there is only I_A in the antenna and no mutual coupling occurs at this frequency point, as the related transmission line stubs can be considered open circuit at the ports..

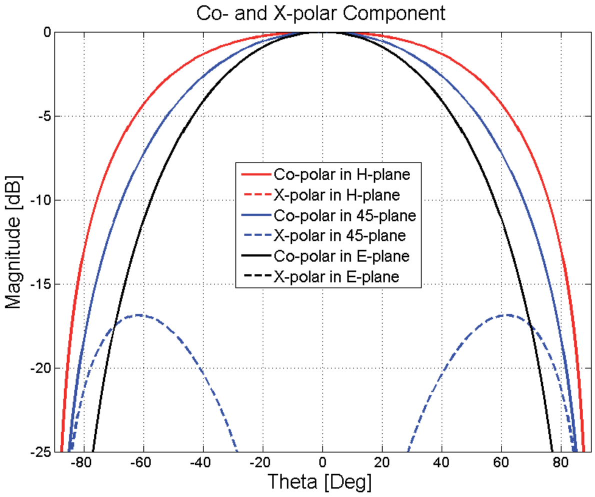

Figure 3.7: Simulated E-field patterns of dual-band OFD at 0.45 GHz ($0.287\lambda_{0.65GHz}$ over infinite PEC ground)

Figure 3.7 and Figure 3.8 show the CST-simulated far-field of the dual-band OFD over an infinite PEC ground at 0.45 and 0.65 GHz (height: 132.6 mm ($0.287\lambda_{0.65GHz}$)), respectively. The details of performance are provided in Table 3.1. As can be seen, there exist quite similar radiation patterns at both 0.45 and 0.65 GHz. However, the deviation of the beamwidths of E- and H-plane becomes larger as the frequency increases, resulting in an increased relative crosspolar level in the higher band.

Similar studies have been done for the cross-fed model that is called the wide-band OFD. The only difference between the two cases is the manner of feed, while all other conditions remain the same. Figure 3.9 and Figure 3.10 show the CST-simulated far-field of the wide-band OFD over an infinite PEC ground at 0.45 and 0.6 GHz, respectively. The details of performance are provided in Table 3.2. It can be observed that the radiation patterns are quite similar at both 0.45 and 0.6 GHz. However, there is also a trend that the deviation of

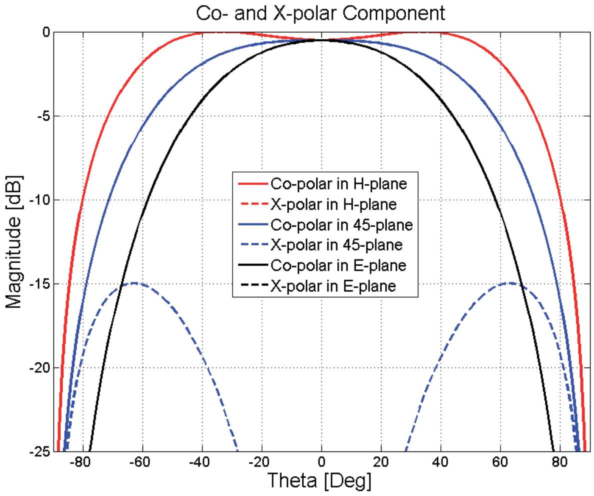

Figure 3.8: Simulated E-field patterns of dual-band OFD at 0.65 GHz ($0.287\lambda_{0.65GHz}$ over infinite PEC ground)

Table 3.1: Performance Details of Dual-band OFD Over Infinite PEC Ground

Frequency (GHz)	0.45	0.65
Return loss (dB, reference: 280 Ω)	13.5	9.8
3dB Beamwidth in E-/H-plane (°)	69.6/106.7	74.7/130.6
Directivity (dBi)	8.1	7.3
Crosspolar level in 45°-plane (dB)	16.9	14.6

the beamwidths of E- and H-plane will become larger as the frequency increases, which results in an increased relative crosspolar level in the upper end of the band.

Now, we can as well consider the 2-port case of the wide-band OFD. The overview of the antenna geometry is illustrated in the left side of Figure 3.11, while it is depicted in the right side the detail of how the two orthogonal ports are cross-fed. By the way, this cross-fed style is also found in some other antenna designs, e.g., in [59]. The scattering parameters with reference to 280 Ω are shown in Figure 3.12, from which we come to know that there exists high isolation (better than 40 dB) between the two orthogonal polarization ports. By the way, S_{12} should be 0 ($-\infty$ dB) if the model and the feed are perfectly symmetrical; the deviation from this, however, seems to be caused by some slight accuracies in the numerical calculations. As a result, it is very promising to realize dual-linear polarization in this type of 2-port antenna. Moreover, it is also possible that both right-hand and left-hand circular polarizations can be realized by manipulating the excitations with same amplitude but ±90° phase difference at the two ports.

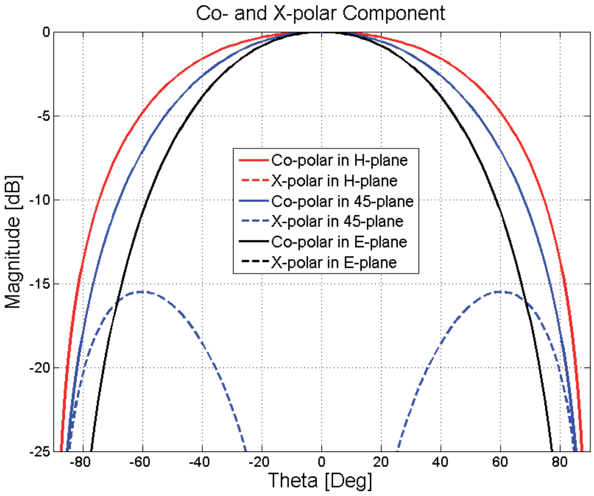

Figure 3.9: Simulated E-field patterns of wide-band OFD at 0.45 GHz ($0.287\lambda_{0.65GHz}$ over infinite PEC ground)

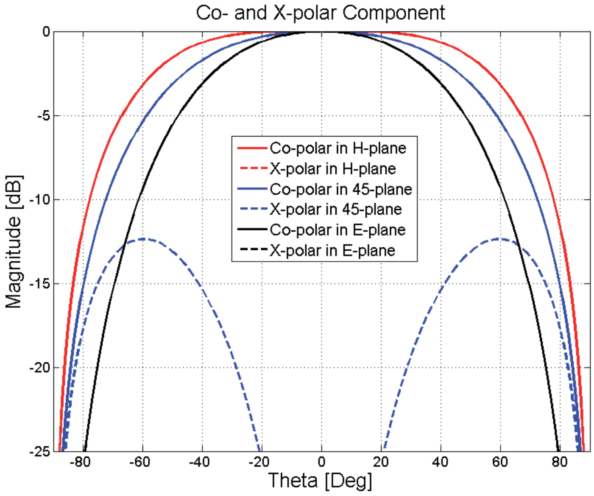

Figure 3.10: Simulated E-field patterns of wide-band OFD at 0.60 GHz ($0.287\lambda_{0.65GHz}$ over infinite PEC ground)

Table 3.2: Performance Details of Wide-band OFD Over Infinite PEC Ground

Frequency (GHz)	0.45	0.6
Return loss (dB, reference: 280 Ω)	13.7	10.0
3dB Beamwidth in E-/H-plane (°)	71.6/101.5	79.8/108.0
Directivity (dBi)	7.9	7.2
Crosspolar level in 45°-plane (dB)	15.5	12.4

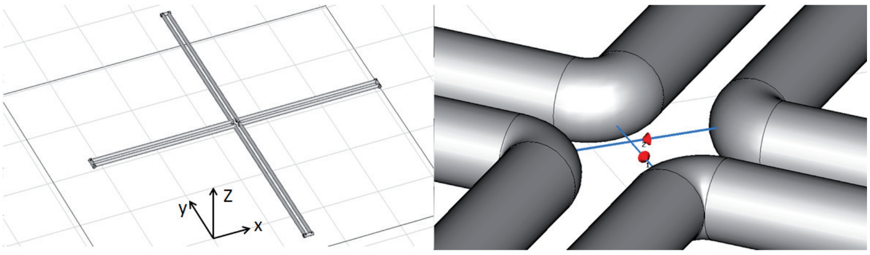

Figure 3.11: 2-port wide-band OFD over infinite PEC ground (CST model)

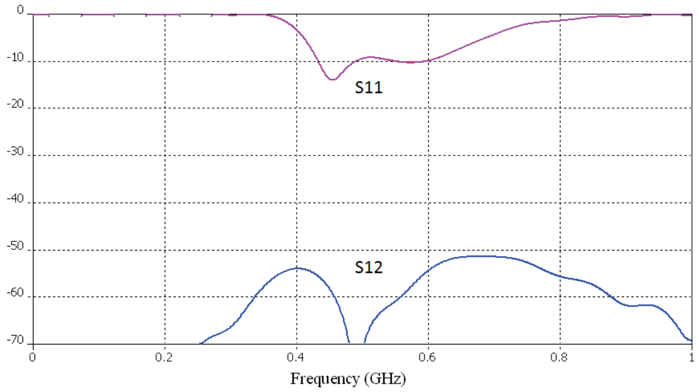

Figure 3.12: S-parameters in dB of 2-port wide-band OFD over infinite PEC ground (Ref: 280 Ω, CST)

3.4 Summary of Chapter 3

A folded dipole can be thought of as the fatter version of a wire dipole, and its impedance bandwidth is somewhat widened. Two orthogonally-connected and cross-fed folded dipoles can achieve an even wider impedance bandwidth. Furthermore, the orthogonal folded dipoles can be fed through different combinations of feed nodes, i.e. node 1, 2, 3, 4 in Figure 3.2, giving rise to the dual-band and the wide-band OFD, respectively. The impedance can be matched well to 300 Ω in both modes. And the properties of the linearly-polarized radiation patterns in the two modes vary quite little, but for ±45° rotation of E- and H-planes. In other words, the orthogonal folded dipoles have a possibility of being pattern-reconfigurable in a context of linear/dual-linear and circular polarizations. In addition, it is pattern-reconfigurable in a context of E-plane orientation at different ϕ planes (0°, ±45° and 90°), when it only comes to linear polarization. Due to some manufacturing issues, the orthogonal folded dipoles are preferably to be applied within the VHF/UHF bands.

Chapter 4

Log-Periodic Folded Dipole Array

The log-periodic antennas have been used for decades in a lot of wideband applications. There are many interesting and bizarre shapes, and a variety of practical antennas have been built from planar and wire log-periodic structures, planar and wire trapezoidal toothed log-periodic structures and log-periodic slots, etc. The configurations most widely used for performing EMC tests are two types, i.e. the circularly polarized conical log-periodic spiral and the linearly polarized log-periodic dipole array. In this chapter, we will introduce a new configuration, log-periodic folded dipole array, and study its performance in potential applications.

4.1 Background

The concept of the log-periodic structure, introduced by DuHamel and Isbell [57], closely paralleled the concept of the frequency independent antennas. DuHamel first studied planar curved (or trapezoidal toothed) log-periodic antennas. He later came up with their wired versions when he discovered that there was a strong current concentration at or near the edges of the planar conductors. Isbell first introduced the configuration of the Log-periodic Dipole Array (LPDA, for short hereinafter) .

As shown in Figure 4.1, the lengths, diameters, dipole spacings and gap spacings of the array increase logarithmically as defined by a scale factor *k*,

$$k = \frac{l_{n+1}}{l_n} = \frac{R_{n+1}}{R_n} = \frac{d_{n+1}}{d_n} = \frac{s_{n+1}}{s_n} = \frac{O_{n+1}}{O_n} \tag{4.1}$$

$$\begin{aligned} O_{n+1} &= R_{n+1} - R_n \\ O_n &= R_n - R_{n-1} \end{aligned} \tag{4.2}$$

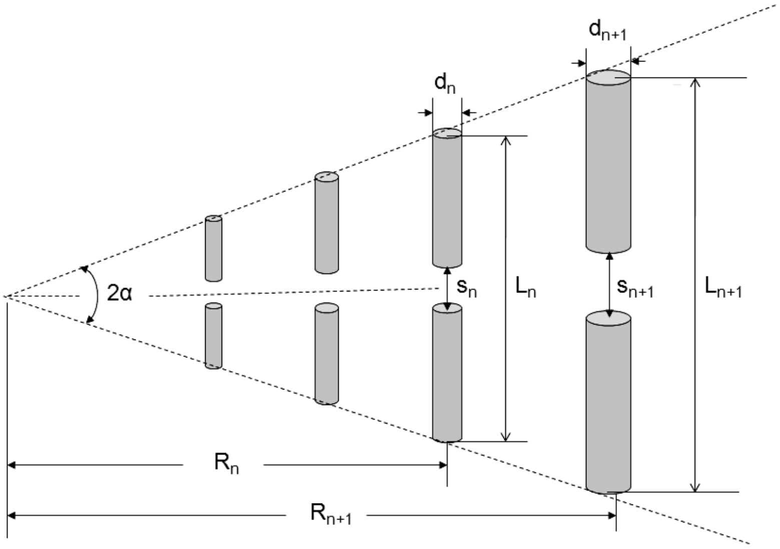

Figure 4.1: A log-periodic dipole array with apex angle 2α

Straight lines through all of the dipole ends join to an apex and thus form an apex angle 2α. In order to find the possible relationship between α and *k*, we can first define a spacing factor ξ,

$$\xi = \frac{R_{n+1} - R_n}{L_{n+1}} = \frac{O_{n+1}}{L_{n+1}} \tag{4.3}$$

According to the trigonometry and (4.1), we have

$$\tan\alpha = \frac{L_{n+1}}{2R_{n+1}} = \frac{L_{n+1}}{2\sum_{m=0}^{\infty} \frac{O_{n+1}}{k^m}} = \lim_{m\to\infty} \frac{L_{n+1}}{2O_{n+1}\left(\frac{1-k^{-m}}{1-k^{-1}}\right)} = \frac{1-k^{-1}}{2\xi} \tag{4.4}$$

By the way, a more straightforward method is as follows:

$$\tan\alpha = \frac{L_{n+1}}{2R_{n+1}} = \frac{(R_{n+1} - R_n)/R_{n+1}}{2(R_{n+1} - R_n)/L_{n+1}} = \frac{1 - R_n/R_{n+1}}{2\xi} = \frac{1-k^{-1}}{2\xi} \tag{4.5}$$

Then it can be concluded that the outline of the LPDA shape can be defined by any two of the three geometric parameters, i.e. *k*, α and ξ.

Because it is usually very difficult to obtain wires or tubing of many different diameters and to maintain tolerances of very small gap spacings, constant dimensions in these can be used, as the minor factors will not sufficiently degrade the overall performance [57]. As the operating frequency changes, the active region shifts to a different portion of the array. The frequency limits of the operational band are roughly determined by the frequencies at which the longest and shortest dipoles are half-wave resonant [3].

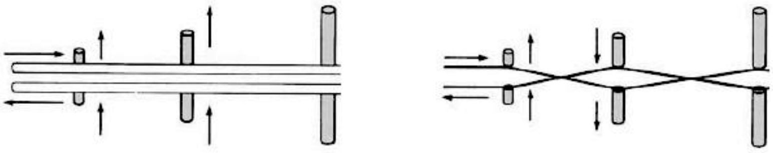

Figure 4.2: Two feed methods: Straight (left) and crisscross connection (right).

There are two basic methods to connect and feed different dipoles in such an array, as shown in Figure 4.2, the straight connection and the crisscross connection, respectively. In the former case, the currents in the terminals of any two adjacent elements have almost the same phase when the elements are closely spaced. The phase progression of the currents is to the right, which results in an end-fire beam in the direction of the longer elements, which will obstruct the radiation and thus make this excitation unsuited. In the latter case, however, the currents in the terminals of any two close adjacent elements have 180° phase reversal. At a certain frequency, very little energy is radiated by the neighboring closely spaced short dipoles, due to the cancelation of radiation by currents with nearly 180° phase reversal. At the same time the longer and larger spaced elements radiate, because of more significant phase difference than 180° reversal. The phase reversal produces a phase progression so that the energy is beamed end fire in the direction of the shorter elements, and the most active elements are those that are near resonant with a combined radiation pattern towards the vertex of the array [57].

4.2 Log-periodic Folded Dipole Array

Based on the concept of the Log-periodic Dipole Array, we may as well apply folded dipoles instead of dipoles as the elements of the array, resulting in the Log-periodic Folded Dipole Array (LPFDA, for short hereinafter) . Since a folded dipole with two ports can conduct current in the transmission-line mode, the nearly 180° phase reversal may occur between the two ports at around resonance frequency. This is similar to the crisscross-fed LPDA in terms of the direction of the main beam, i.e., an auxiliary wedge enclosing all the folded dipoles forms an arrow pointing in the direction of the main beam maximum.

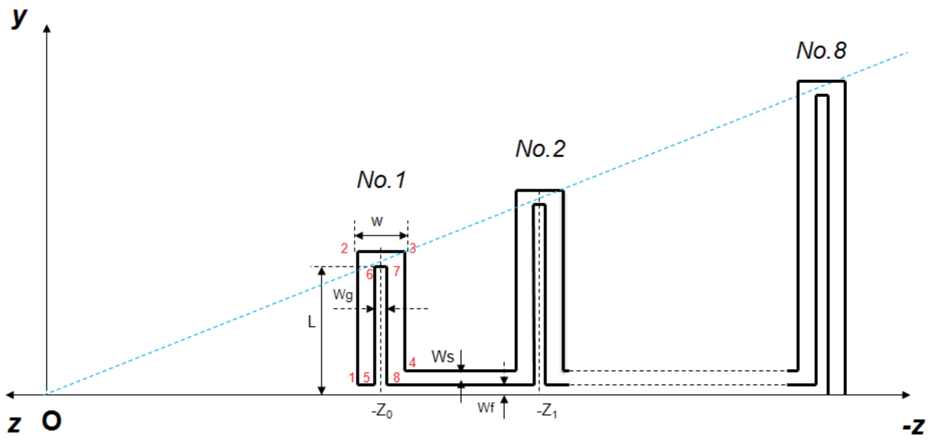

Figure 4.3: Partly-scaled strip-type 8-pair LPFDA (upper half)

4.2.1 LPFDA With Length and Spacing Log-periodically Scaled

As a starting point, let us first study a strip-type 8-pair LPFDA with simple geometry. The upper half of the complete antenna structure is shown in Figure 4.3, where there are in total 6 parameters that define this structure, i.e., the offset from origin Z_0, the arm length *L*, the strip width W_s, the feed gap W_f, the fold gap W_g and the scale factor *k*, respectively. The bottom half can readily be obtained by imaging with respect to the z-axis due to symmetry. By the way, it is actually how we model the array in CST. The copper strip thickness is constant, and W_s, W_f and W_g are kept constant as well just for simplicity, while the length of and the spacing between adjacent folded dipoles are log-periodically scaled. The 8 folded arms, namely No.1 to No.8 in the figure, are positioned by 8 sets of points (point 1, 2, ..., 8 in the figure) and structured by lines joining these points. Assume the minimum geometrical wavelength is $\lambda_{geo-min}$, which equals 50 mm in our attempts, corresponding to a frequency of 6 GHz in free space. By the way, the geometrical wavelength is merely related to the antenna geometry in free space, and it can be somewhat different from the real operating wavelength of an antenna in free space or in other medium.

The normalized coordinates (z/$\lambda_{geo-min}$, y/$\lambda_{geo-min}$) of the points for the No.1 arm (A1P1-A1P8) are given by the following expressions. (Note: z-coordinates need to add negative signs before used to structure the geometry in the -z half space)

w = W_g+2W_s

A1P1: (z1, y1) = (Z_0-w/2, W_f)

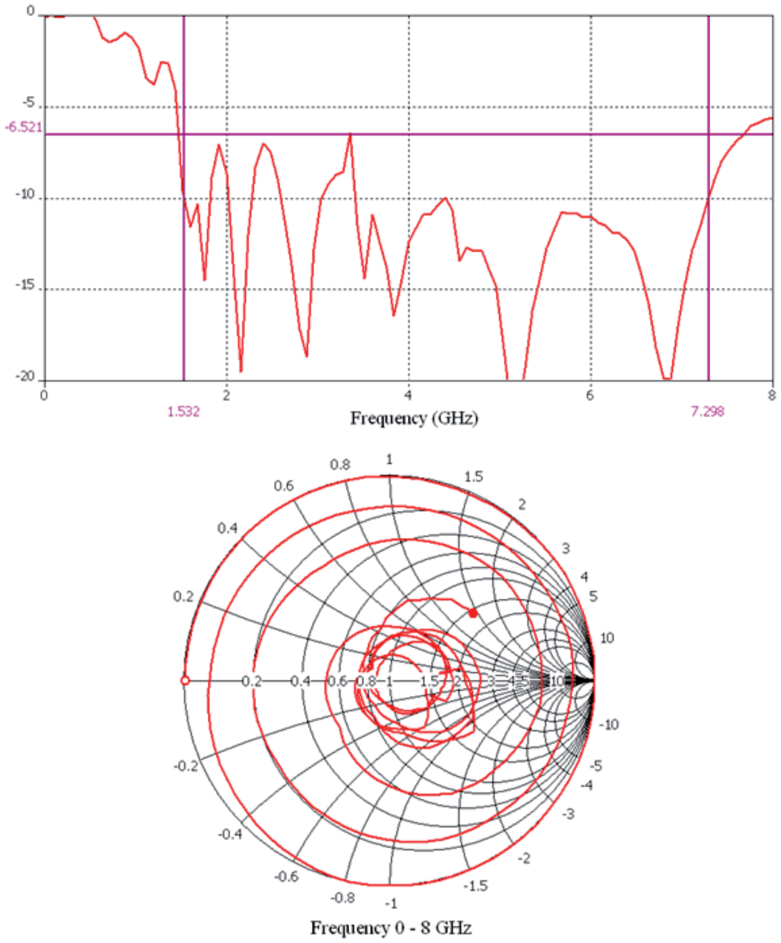

Figure 4.4: S_{11} magnitude in dB and Smith chart of partly-scaled 8-pair LPFDA (Ref: 200 Ω, CST)

A1P2: (z2, y2) = (Z_0-w/2, L+W_s)

A1P3: (z3, y3) = (Z_0+w/2, L+W_s)

A1P4: (z4, y4) = (Z_0+w/2, W_f+W_s)

A1P5: (z5, y5) = (Z_0-W_g/2, W_f)

A1P6: (z6, y6) = (Z_0-W_g/2, *L*)

A1P7: (z7, y7) = (Z_0+W_g/2, *L*)

A1P8: (z8, y8) = (Z_0+W_g/2, W_f)

Since the scale factor *k*=Z_1:Z_0, the normalized coordinates of the points for the No.2 arm (A2P1-A2P8) can be derived from the previous coordinates, respectively,

A2P1: (z1', y1') = (*k*·Z_0-w/2, W_f+W_s)

A2P2: (z2', y2') = (*k*·Z_0-w/2, *k*·*L*+W_s)

A2P3: (z3', y3') = (*k*·Z_0+w/2, *k*·*L*+W_s)

A2P4: (z4', y4') = (*k*·Z_0+w/2, W_f+W_s)

A2P5: (z5', y5') = (*k*·Z_0-W_g/2, W_f)

A2P6: (z6', y6') = (*k*·Z_0-W_g/2, *k*·*L*)

A2P7: (z7', y7') = (*k*·Z_0+W_g/2, *k*·*L*)

A2P8: (z8', y8') = (*k*·Z_0+W_g/2, W_f)

The coordinates of all of the rest arms can similarly be obtained by scaling based on the successively preceding arm. Here we skip the relevant details.

Table 4.1: Normalized Parameters For The Simple LPFDA

Parameters ($\lambda_{geo-min}$=50 mm)	**Value**
$Z_0/\lambda_{geo-min}$	0.3011
$L/\lambda_{geo-min}$	0.1337
$W_g/\lambda_{geo-min}$	0.0114
$W_s/\lambda_{geo-min}$	0.0204
$W_f/\lambda_{geo-min}$	0.0214
k	1.2682

As it is very difficult to study the impedance property of the LPFDA in an analytical manner, we choose to use the Genetic Algorithm (implemented in MATLAB) together with CST MWS to optimize the return loss, where the feed is a discrete port with 200

Ω resistance, connecting the small feed gap at the shortest arms. We set in the algorithm 200 population and 5 generations. The mesh density in CST is set low but with acceptable accuracy, in order to balance the simulation time and precision. When the optimization process finishes, the structure will be further investigated through finer meshing. Finally, we arrive at that the best result for only the return loss takes place when the 6 parameters are selected as listed in Table 4.1.

The simulated results, i.e, S_{11} amplitude and Smith chart curves, show that the return loss is better than -10 dB in the most of the range from 1.53 to 7.3 GHz (the bandwidth ratio $\approx$ 4.8:1). It can be seen, however, that there exist a couple of not so well matched peaks in the lower range.

It can be observed from Figure 4.8 A) and B) that the directivities vary about 1-2 dB within the most of the band from 2 to 7 GHz, and the averaged value is about 7 dBi. It also shows that the main lobes direct to the positive z-axis, and the back lobes are about 12 dB less than the maximum front radiation within the most of the band. The beamwidths in both E and H planes vary not so much when the frequency varies within the most of the band. Analogous to the patterns of a dipole antenna, the E plane patterns of the LPFDA are narrower than the H plane patterns. Meanwhile, Figure 4.8 C) tells us that the relative crosspolar levels remain below -12 dB over the most of the band.

4.2.2 LPFDA With All Dimensions Log-periodically Scaled

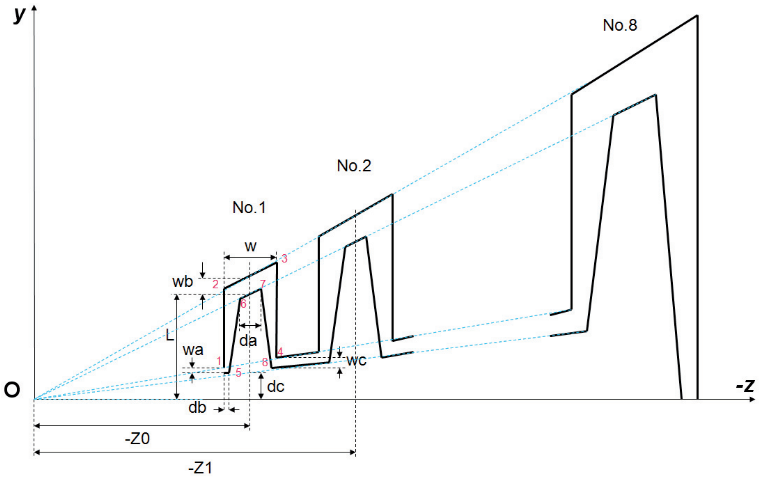

Figure 4.5: Fully-scaled strip-type 8-pair LPFDA (upper half)

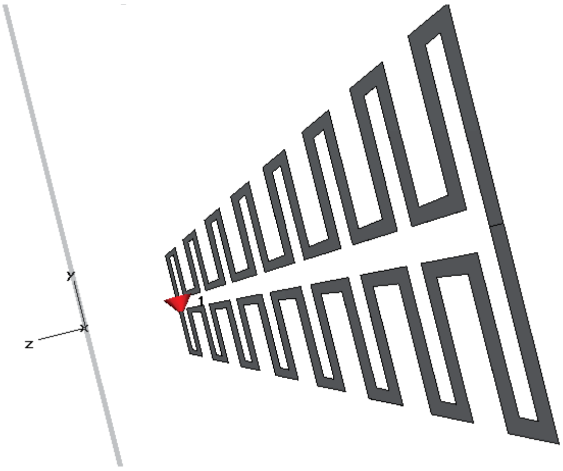

Figure 4.6: Fully-scaled strip-type 8-pair LPFDA modeled in CST

If all the dimensional parameters are scaled log-periodically, we get the following fully-scaled LPFDA, upper half of which is illustrated in Figure 4.5. The bottom half can easily be obtained through imaging. In total, there are 10 parameters that define the complete structure, i.e. Z_0, *L*, *W*, W_a, W_b, W_c, d_a, d_b, d_c and *k* (scale factor), respectively, while the thickness of the strip is a constant.

The same as in the previous section, the 8 folded arms are positioned by corresponding 8 sets of points and constructed by lines connecting these points. Assume the minimum geometrical wavelength is $\lambda_{geo-min}$ (50 mm), the normalized coordinates (z/$\lambda_{geo-min}$, y/$\lambda_{geo-min}$) of the points for the No.1 arm (A1P1-A1P8) become as follows,

a = L/Z_0

b = d_c/Z_0

A1P1: (z1, y1) = (Z_0-W/2, b·z1+W_a)

A1P2: (z2, y2) = (Z_0-W/2, a·z2+W_b)

A1P3: (z3, y3) = (Z_0+W/2, a·z3+W_b)

A1P4: (z4, y4) = (Z_0+W/2, b·z4+W_c)

A1P5: (z5, y5) = (Z_0-W/2+d_b, b·z5)

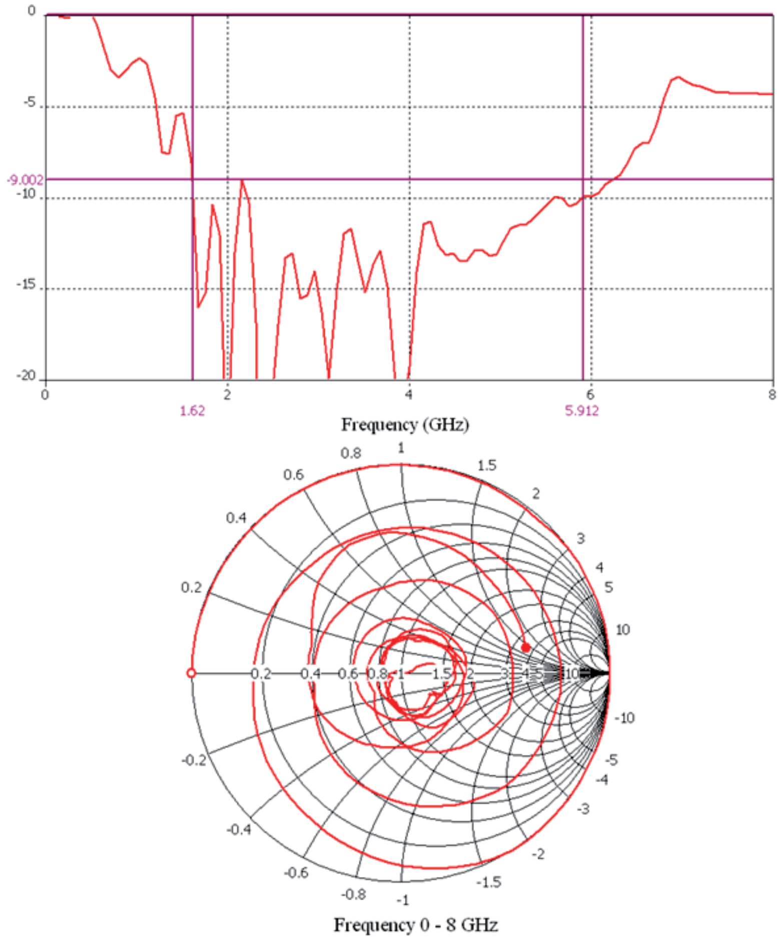

Figure 4.7: S_{11} magnitude in dB and Smith chart of fully-scaled 8-pair LPFDA (Ref: 280 Ω, CST)

A1P6: (z6, y6) = (Z_0-d_a/2, a·z6)

A1P7: (z7, y7) = (Z_0+d_a/2, a·z7)

A1P8: (z8, y8) = (Z_0+W/2-d_b, b·z8)

The coordinates of points of the No.2 arm (A2P1-A2P8) can be derived based on the previous coordinates, A2P1: (z1’, y1’) = (k·z1, k·y1)

A2P2: (z2’, y2’) = (k·z2, k·y2)

A2P3: (z3’, y3’) = (k·z3, k·y3)

A2P4: (z4’, y4’) = (k·z4, k·y4)

A2P5: (z5’, y5’) = (k·z5, k·y5)

A2P6: (z6’, y6’) = (k·z6, k·y6)

A2P7: (z7’, y7’) = (k·z7, k·y7)

A2P8: (z8’, y8’) = (k·z8, k·y8)

Table 4.2: Normalized Parameters For The Modified LPFDA

Parameters ($\lambda_{geo-min}$=50 mm)	**Value**
$Z_0/\lambda_{geo-min}$	0.3384
$L/\lambda_{geo-min}$	0.1634
$w/\lambda_{geo-min}$	0.0389
$wa/\lambda_{geo-min}$	0.0160
$wb/\lambda_{geo-min}$	0.0166
$wc/\lambda_{geo-min}$	0.0168
$da/\lambda_{geo-min}$	0.0145
$db/\lambda_{geo-min}$	0.0118
$dc/\lambda_{geo-min}$	0.0190
k	1.2213

Similarly, the coordinates of each of the rest arms can be scaled up based on its adjacent preceding arm. The graphical model of the complete structure in CST is displayed in Figure 4.6. The feed, which connects the small gap at the shortest arm, is a discrete port with 280 Ω resistance, larger than 200 Ω of the simple version in the previous section. Note that the choice of 280 Ω as the reference impedance is in order to obtain the best possible match across the bandwidth of interest. We use the Genetic Algorithm (200 population and 5 generations) together with CST to optimize only the return loss also. The best result occurs when the 10 parameters are set as listed in Table 4.2.

The S_{11} and Smith chart curves show that the return loss with respect to 280 Ω is better than -10 dB over the whole band from 1.62 to 5.91 GHz (the bandwidth ratio $\approx$ 3.6:1),

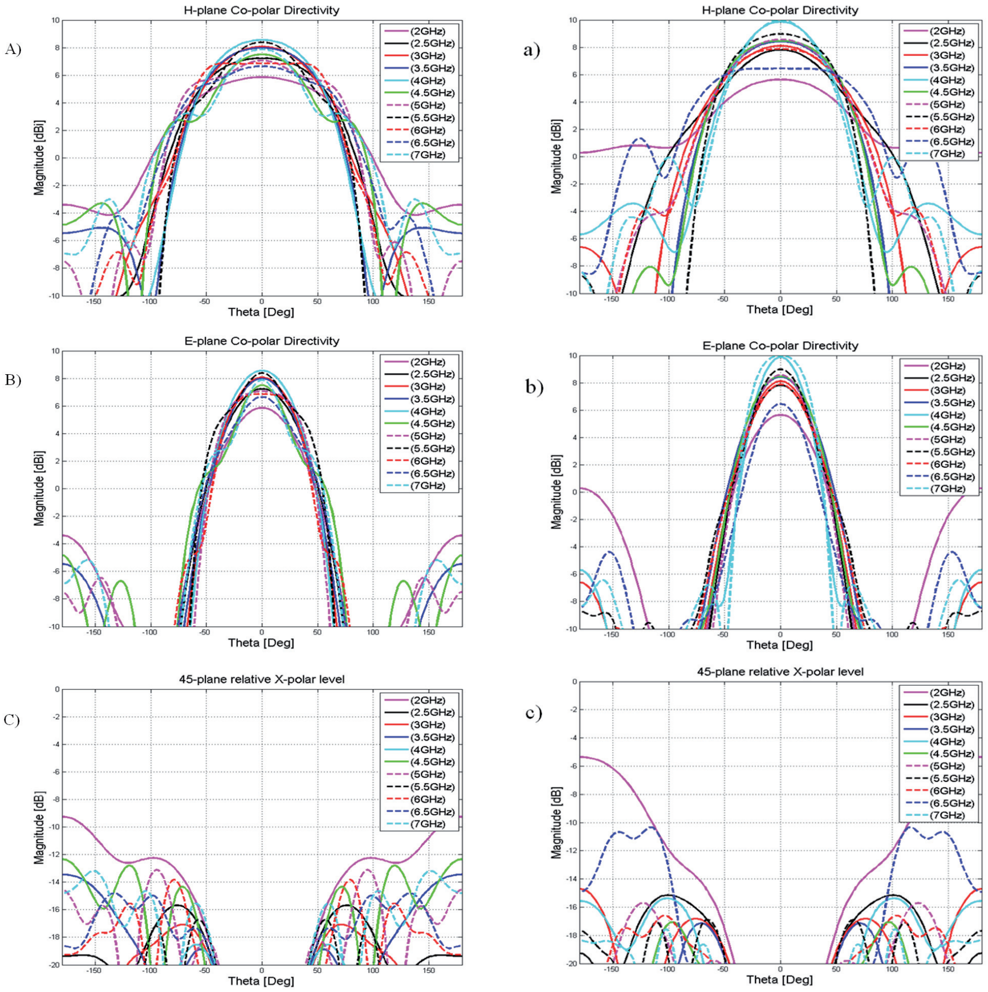

Figure 4.8: A) a) H-plane copolar directivity B) b) E-plane copolar directivity C) c) 45°-plane relative crosspolar level of partly-scaled and fully-scaled 8-pair LPFDA, respectively (CST)

except for one peak up to -9 dB at around 2.2 GHz.

As can be observed from the right column of Figure 4.8, the directivities vary about 1-2 dB within the most of the band from 2 to 7 GHz; however, the averaged value is about 8 dBi. The main lobes also direct to the positive z-axis, and the back lobes are about 14 dB less than the maximum front radiation within the most of the band. Similarly, the beamwidths in both E and H planes vary still not so much when the frequency varies within the most of the band, and the E plane patterns are narrower than the H plane patterns. Meanwhile, the cross-polar levels remain below -15 dB over the most of the band. Compared with the partly-scaled version, the fully-scaled version has advantages in terms of 1-dB higher directivity, 2-dB better front-to-back ratio and 3-dB less relative crosspolar level over the most of the band.

4.3 Summary of Chapter 4

Similar to the conventional crisscross-fed LPDA, the LPFDA radiates its endfire main beam in the direction of the shorter dipoles in the array. The partly and fully scaled LPFDAs have been simulated and optimized for the reflection coefficient, respectively. According to our practice and experience, the latter is much more likely to be impedance-matched over a wide band, compared to the former. Moreover, the latter outperforms the former also in radiation characteristics, such as the directivity, the front-to-back ratio and the relative crosspolar level.

As for the fully scaled LPFDA, another point should be noted concerning the copolar patterns in the two principal planes. As can be seen from Figure 4.8, the magnitudes of both E- and H-plane patterns when θ=90^o are about 8 or even much more dB lower than the corresponding maxima (i.e., when θ=0^o) over the most of the bandwidth. This means the radiation of LPFDA in the broadside direction is considerably lower than that in the endfire direction. Consider oppositely co-locating two symmetrical LPFDA petals (shorter folded dipoles inner, longer ones outer) in one plane to make a flat antenna that is a tiny distance above a perfect magnetic conductor (PMC) ground plane. Even though acceptable impedance match could somehow be achieved within a narrow or even a wide frequency band, the directivity in the broadside direction will tend to be low anyway.

If a PEC ground plane is present instead of the PMC plane, then the LPFDA petals should be raised to a certain height above the ground, and also rotated by a certain angle from the ground so as to keep a roughly half wavelength spacing between different pairs of folded dipoles. By this means, it is possible to obtain good matching and radiation characteristics over wideband. Actually, the wideband Eleven antenna is based on this idea and will be elaborated in Chapter 6.

Chapter 5

Multi-Port Eleven Antenna For Use In Satellite Terminals

It is fact that geostationary-orbit (GSO) satellites with slight inclination angles will trace a figure 8 pattern instead of a fixed point in the sky over one day. Tracking as well as fine-tuning is inherently called for by the land-mobile or maritime satellite communications terminals to minimize the antenna pointing error to the fullest so as to avoid a degraded satellite link. Today's tracking technologies for satellite communications include conical scan, step track, electronic beam squinting, monopulse tracking and so on. Monopulse tracking systems were reported with very good tracking accuracy, fast dynamic response as well as comparatively low requirement on system signal-to-noise ratio, and have been utilized in many of the large earth stations, ship-borne terminals and satellite-to-satellite communications [60].

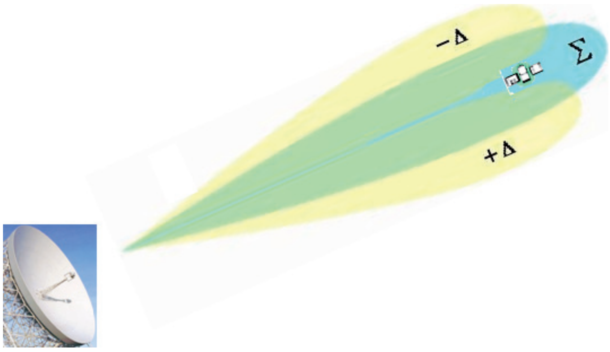

Figure 5.1: Monopulse beams: the sum and the difference beams in one plane

Satellite terminals with monopulse tracking capability can determine the relative angular location of a satellite by receiving a beacon signal from the incoming wave in different antenna beams and comparing the amplitudes and phases. Receiving antennas in monopulse tracking systems typically produce three different beams, a sum beam (Σ mode) and two difference beams, one for azimuth (Δ_{hor} mode) and the other for elevation tracking (Δ_{ver} mode). Figure 5.1 shows the monopulse beams in the 2-D case. The difference beams detect the angular misalignment from the antenna's bore-sight axis to the satellite location, while the sum beam performs as a phase reference, from which the direction of the angular error can be determined.

The Eleven antenna is a new wideband feed that can cover a decade bandwidth up to a largest frequency of within Ku-band, and it has been developed as feed for reflector antennas and in particular for radio telescopes [35] [61] [62] [63]. As reviewed in section 5.3, a single-band circular Eleven antenna can also be combined with a choke horn to form a dual-band feed for reflector antennas on satellite terminals. Moreover, the Eleven feed can be further developed as a multi-port antenna that is capable of producing a sum beam and two difference beams necessary for the monopulse tracking, through different combinations of port excitations.

5.1 4-port Eleven Antenna For Monopulse Tracking

In this section, we will introduce a 4-port Eleven antenna, which is capable of performing monopulse tracking in L-band with linear polarization.

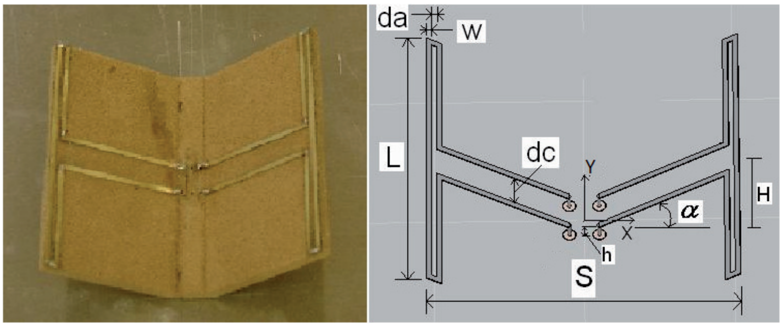

Figure 5.2: Manufactured L-band Eleven antenna and its model in CST

As shown in Figure 5.2, a parallel folded dipole pair, being about half-wavelength apart and a certain distance above a ground plane, is the basic element of a wideband Eleven antenna. This folded dipole pair is designed for operation at around 1.5 GHz (within L-band), and the corresponding dimensions are summarized in Table 5.1. For convenience the folded dipoles are oriented parallel with the y-axis, and we accordingly refer to the yz-plane, hereinafter, as the vertical plane and the xz-plane as the horizontal plane.

Table 5.1: Dimensions of manufactured L-band Eleven antenna

Parameters	Value in mm	Value in degree
Length of dipole *L*	100	-
Width of dipole *w*	2	-
Thickness of all metal lines *t*	0.3	-
Spacing between two parallel dipoles *S*	103.6	-
Arm spacing in folded dipole *da*	2	-
Transmission line spacing *dc*	10	-
Tilted angle α	-	33
The height of the solder point *h*	5.2	-
The height of the folded dipole *H*	33.6	-

5.1.1 Impedance Model (Σ mode)

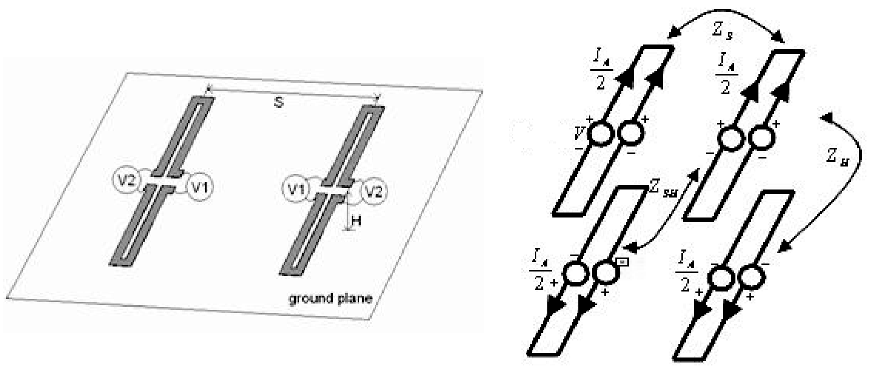

Figure 5.3: Pair of folded dipoles under the Eleven configuration and its equivalent antenna mode

Since the pair of folded dipoles is separated by a distance of *S* and located above the ground plane with a height of *H*, as shown in Figure 5.3, the imaging technique can be applied to remove the ground plane and obtain an equivalent problem with a four-folded-dipole array. There is no radiation from the transmission line mode due to the opposite current direction on the two shorted wires. Therefore, there are no mutual couplings among the transmission line modes of the folded dipoles. The mutual couplings exist only in the antenna mode. Thus, the equivalent problem becomes that the transmission mode current under the Eleven configuration is the same as that in free space and the antenna mode current is changed due to the mutual couplings among the elements in the four-folded-dipole array. The mutual couplings can be presented by mutual impedances Z_S, Z_{2H} and Z_{S2H} of two parallel dipoles separated by a distance of *S*, *2H* and $\sqrt{S^2+(2H)^2}$, respectively. Now we can calculate the impedance in the antenna mode in the same way as calculating active impedance of one element in an antenna array defined as [64]

$$Z_m = \sum_{i=0}^{n} Z_{mn}(I_n/I_m) \tag{5.1}$$

where Z_m is the active impedance of element *m*, I_n is the current on element *n* and Z_{mn} is the mutual impedance between elements *m* and *n*. For our case and due to the excitation (both folded dipoles are excited with the same amplitude and phase), we have the currents on all four folded dipoles with the same amplitude but 180° phase difference on the imaging dipoles. Then we can obtain the antenna mode impedance of a folded dipole under the Eleven configuration is

$$Z_{D,11} = Z_D + Z_S - Z_{2H} - Z_{S2H} \tag{5.2}$$

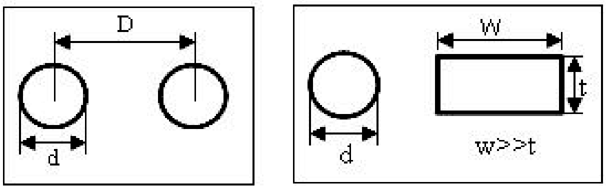

Figure 5.4: Two-conductor transmission line with circular cross section (left) and the equivalence between circular and rectangular cross sections(right)

First, we need to calculate the characteristic impedance of the two-conductor transmission line in order to obtain the impedance characteristics of a folded dipole by using the above analysis. For the characteristic impedance of the two-conductor line with circular cross section, as illustrated in Figure 5.4, we have [65]:

$$Z_0 = \frac{1}{\pi}\sqrt{\frac{\mu}{\varepsilon}}\ln\{\frac{D}{d} + \sqrt{(\frac{D}{d})^2 - 1}\} \tag{5.3}$$

For lines with rectangular cross section, we have equivalence between a rectangular and a circular cross section as [66]:

$$\frac{d}{w} \approx \frac{1}{2}\{1 + \frac{t}{\pi w}[1 + \ln(4\pi\frac{w}{t})]\} \tag{5.4}$$

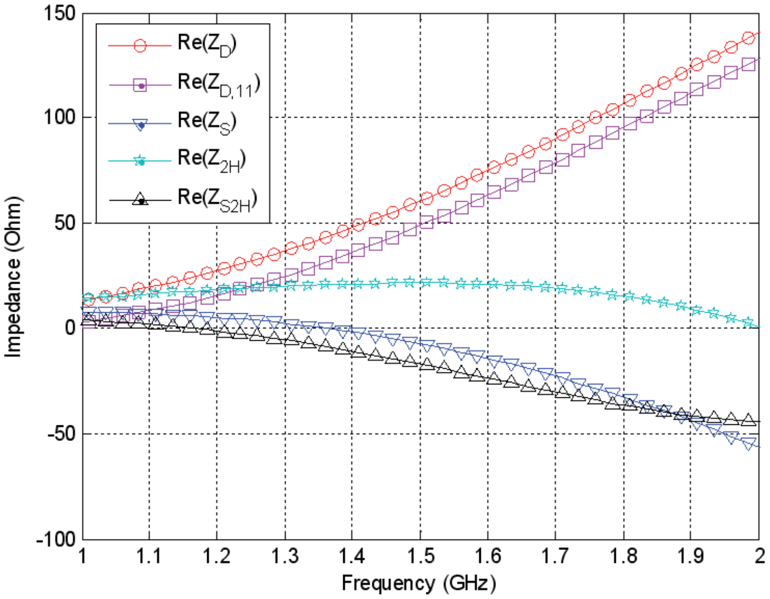

Figure 5.5: Real part of self and mutual impedance of the Eleven antenna shown in Table 5.1.

For antenna mode impedance under the Eleven configuration, we need to calculate the self impedance of the dipole in free space Z_D and the mutual impedances between dipoles for different separations Z_S, Z_{2H} and Z_{S2H}. We calculate the self and mutual impedances of the dipoles of convenience by using the classical approach based on a known dipole current distribution. We list the formula here but leave out the details that can be found in [64] [Eqs. (4.45), (9.52), (9.54)]. For the self impedance, we have

$$Z_D = -\int_{-L/2}^{L/2} \mathbf{E}_j(\mathbf{r}_a) \cdot \mathbf{j}_l(l) dl \tag{5.5}$$

where $\mathbf{j}_l$ is the normalized sinusoidal current distribution along the center line of the dipole and $\mathbf{E}_j(\mathbf{r}_a)$ is the electrical field at the surface of the dipole due to $\mathbf{j}_l$. For mutual impedance, we have

$$Z_M = -\int_{-L_1/2}^{L_1/2} \mathbf{E}_{12}(\mathbf{r}_a) \cdot \mathbf{j}_1(l_1) dl_1 \tag{5.6}$$

where $\mathbf{j}_1(l_1)$ is the normalized current distribution on dipole 1 along l_1, and $\mathbf{E}_{12}(\mathbf{r}_a)$ is the electrical field on the surface of dipole 1 due to the normalized current distribution $\mathbf{j}_2(l_2)$ on dipole 2 along l_2.

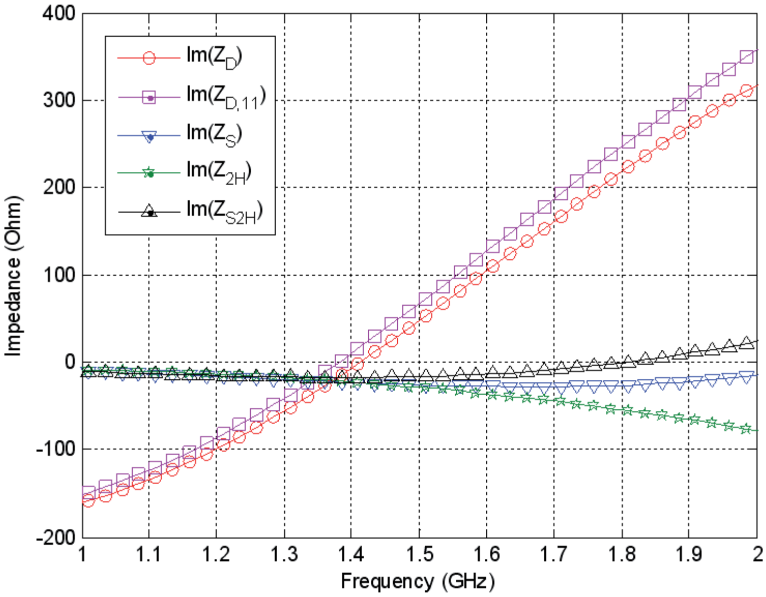

Figure 5.6: Imaginary part of self and mutual impedance of the Eleven antenna shown in Table 5.1.

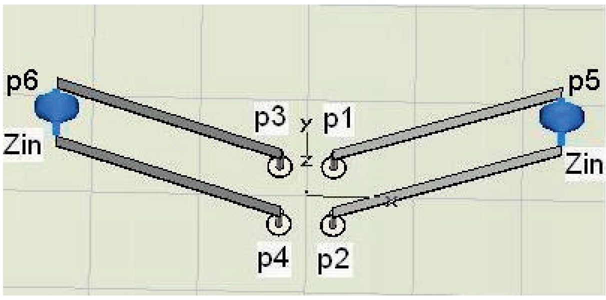

Figure 5.7: The model of the center network in CST (p1 stands for port1 and so on).

In order to verify the present method, a basic Eleven antenna with only one pair of folded dipoles has been manufactured and also modeled in CST MWS, as illustrated in Figure 5.2 and specified in detail in Table 5.1. By the way, the substrate is made of Divinicell foam, which at L band is low loss and low relative permittivity (close to 1). By using equations (5.3) and (5.4), the characteristic impedance of the transmission line of the folded dipole in the transmission line mode can be obtained,

$$Z_0 = \frac{1}{\pi} \cdot 377 \cdot \cosh^{-1} \frac{4}{1.26} = 218\ \Omega \tag{5.7}$$

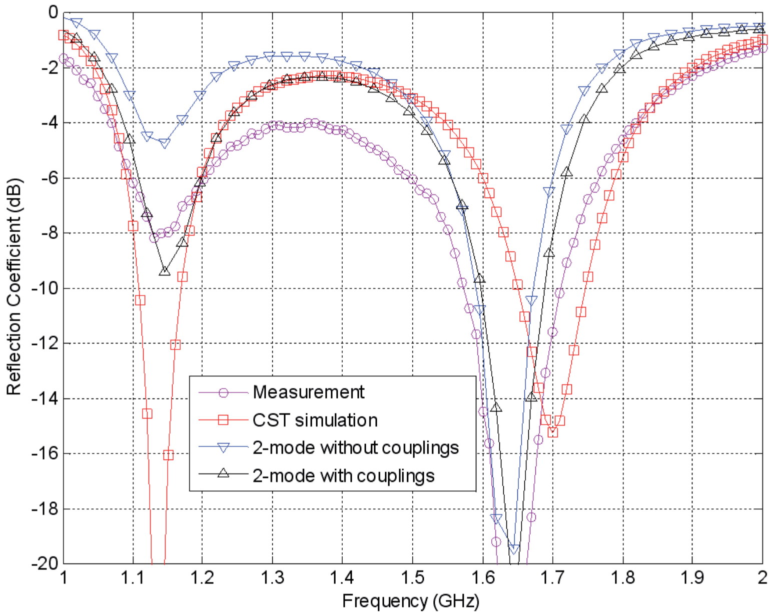

Figure 5.8: Calculated, simulated and measured reflection coefficients of the Eleven antenna. ("2-mode" means that both the antenna mode and the transmission line mode are taken into account on the folded dipoles).

The self and mutual impedances of the folded dipole can be calculated by equations (5.5) and (5.6), and the real and imaginary parts are presented in Figure 5.5 and 5.6. Then, by using equations (3.6), (3.14) and (5.2), we can calculate the input impedance of the folded dipole under the Eleven configuration. It should be noted that Z_d in (3.14) should be replaced by $Z_{D,11}$ calculated by using (5.2) if the mutual couplings are included.

In the model as shown in Figure 5.7, the central network of the transmission lines connecting the center coaxial cables and the folded dipoles is complicated and not easy to be modeled analytically. Therefore, we use CST to model it and obtain the S-parameters of the central network, when ports 5 and 6 are not loaded with Z_{in}. Based on these S-parameters, we can calculate the S-matrix of the central network when the ports 5 and 6 are loaded with Z_{in}. The calculated, simulated and measured reflection coefficient is shown in Figure 5.8. The reflection coefficient of the Eleven antenna is obtained by using the following formula: $S_{11,tot} = S_{11} - S_{12} + S_{13} - S_{14}$, because the excitation for the Eleven antenna is the same amplitude for all port and with the phase (0°, 180°, 0°, 180°) from port 1 to port 4, respectively. One can observe that the data from the present method including the mutual couplings agree better with the measured one than the method without including the mutual couplings, and all data calculated using the present method, simulated from CST and the measured agree well in general, which verifies the present method.

5.1.2 Radiation Model

Sum Channel

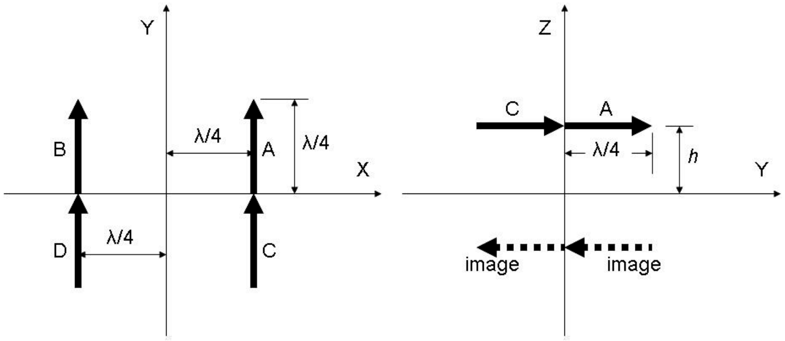

Figure 5.9: Top and side views of sum channel model

As shown in Figure 5.9, the parallel folded dipole pair can be simply modeled as 4 quarter-wavelength monopoles, i.e. A, B, C, D, hanging a certain distance over an infinite ground plane. The central network has no contribution to the far field sum pattern, because of cancelation of opposite currents along the adjacent arms of the transmission lines.

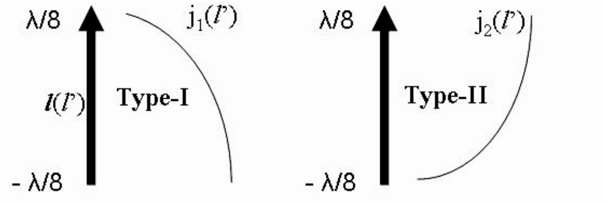

Figure 5.10: Type-I and Type-II monopoles

First consider two types of monopoles shown in Figure 5.10, respectively. Each monopole is vertical (y-directed) with its center aligned with the origin of the Cartesian coordinate system. The Type-I has a y-directed current with a presumed sine-tapered current distribution,

$$j_1(l') = \sin[k(\frac{\lambda}{8} - l')] \quad (-\frac{\lambda}{8} \leq l' \leq \frac{\lambda}{8}, \ k = \frac{2\pi}{\lambda}) \tag{5.8}$$

And we have,

$$\hat{l} \cdot \hat{r} = \hat{y} \cdot \hat{r} = \sin\theta \sin\phi \tag{5.9}$$

The current distribution factor [64] [Eq. (4.7)], i.e. the Fourier transform of the current distribution along the monopole turns to be,

$$\begin{aligned} &\tilde{j_1}(k\hat{l} \cdot \hat{r}) = \textstyle\int j_1(l')e^{jkl'\hat{l}\cdot\hat{r}}dl' = \int_{\frac{-\lambda}{8}}^{\frac{\lambda}{8}} \sin[k(\frac{\lambda}{8} - l')]e^{jkl'\hat{l}\cdot\hat{r}}dl' \\ &= \tfrac{e^{jkl'\hat{l}\cdot\hat{r}}}{(jkl'\hat{l}\cdot\hat{r})^2+(-k)^2}[jkl'\hat{l} \cdot \hat{r}\sin(\tfrac{\pi}{4} - kl') + k\cos(\tfrac{\pi}{4} - kl')]|_{\frac{-\lambda}{8}}^{\frac{\lambda}{8}} \\ &= \tfrac{e^{j\frac{\pi}{4}\sin\theta\sin\phi} - j\sin\theta\sin\phi e^{-j\frac{\pi}{4}\sin\theta\sin\phi}}{k(1-\sin^2\theta\sin^2\phi)} \end{aligned} \tag{5.10}$$

So the far-field function will become [64](Eq. 4.5),

$$G_1(\hat{r}) = \eta I_0 G_{id}(\hat{r})\tilde{j_1}(k\hat{l} \cdot \hat{r}) = \eta I_0 \frac{-jk}{4\pi}(\cos\theta\sin\phi\hat{\theta} + \cos\phi\hat{\phi})\tilde{j_1}(k\hat{l} \cdot \hat{r})$$

where η is the wave impedance of free space; I_0 is the current excitation at the feed gap; $G_{id}(\hat{r})$ is the far-field function of the incremental electric current with unit amplitude, and $G_{id}(\hat{r}) = \frac{-jk}{4\pi}[\hat{l} - (\hat{l} \cdot \hat{r})\hat{r}]$

When this monopole is translated to a point in the xy-plane, e.g. A($\frac{\lambda}{4}\hat{x}, \frac{\lambda}{8}\hat{y}, 0\hat{z}$), its far-field then turns out to be

$$\overrightarrow{r_A} = \frac{\lambda}{4}\hat{x} + \frac{\lambda}{8}\hat{y} : \ G_{1A}(\hat{r}) = G_1(\hat{r})e^{jk\overrightarrow{r_A}\cdot\hat{r}} = G_1(\hat{r})e^{jk(\frac{\lambda}{4}\sin\theta\cos\phi + \frac{\lambda}{8}\sin\theta\sin\phi)} \tag{5.11}$$

Similarly, we have,

$$\overrightarrow{r_B} = -\frac{\lambda}{4}\hat{x} + \frac{\lambda}{8}\hat{y} : \ G_{1B}(\hat{r}) = G_1(\hat{r})e^{jk\overrightarrow{r_B}\cdot\hat{r}} = G_1(\hat{r})e^{jk(-\frac{\lambda}{4}\sin\theta\cos\phi + \frac{\lambda}{8}\sin\theta\sin\phi)} \tag{5.12}$$

$$\overrightarrow{r_C} = \frac{\lambda}{4}\hat{x} - \frac{\lambda}{8}\hat{y} : \ G_{1C}(\hat{r}) = G_1(\hat{r})e^{jk\overrightarrow{r_C}\cdot\hat{r}} = G_1(\hat{r})e^{jk(\frac{\lambda}{4}\sin\theta\cos\phi - \frac{\lambda}{8}\sin\theta\sin\phi)} \tag{5.13}$$

$$\overrightarrow{r_D} = -\frac{\lambda}{4}\hat{x} - \frac{\lambda}{8}\hat{y} : \ G_{1D}(\hat{r}) = G_1(\hat{r})e^{jk\overrightarrow{r_D}\cdot\hat{r}} = G_1(\hat{r})e^{jk(-\frac{\lambda}{4}\sin\theta\cos\phi - \frac{\lambda}{8}\sin\theta\sin\phi)} \tag{5.14}$$

If each of them is further translated by a certain distance *h* over xy-plane which is assumed as an infinite PEC ground plane, the far-field can be derived by taking its image into account [64](Eq. 4.64), respectively,

$$G'_{1A}(\hat{r}) = G_{1A} \cdot 2j\sin(kh\cos\theta) \tag{5.15}$$

$$G'_{1B}(\hat{r}) = G_{1B} \cdot 2j \sin(kh \cos\theta) \tag{5.16}$$

$$G'_{1C}(\hat{r}) = G_{1C} \cdot 2j \sin(kh \cos\theta) \tag{5.17}$$

$$G'_{1D}(\hat{r}) = G_{1D} \cdot 2j \sin(kh \cos\theta) \tag{5.18}$$

Now we consider a Type-II monopole, which has a y-directed current with a presumed cosine-tapered current distribution,

$$j_2(l') = \cos[k(\frac{\lambda}{8} - l')] \qquad (-\frac{\lambda}{8} \leq l' \leq \frac{\lambda}{8},\ k = \frac{2\pi}{\lambda}) \tag{5.19}$$

The same method can be applied to study the far-field of this monopole when it is translated to 4 different positions of interest, and the results become accordingly,

$$\begin{aligned} &\tilde{j_2}(k\hat{l} \cdot \hat{r}) = \textstyle\int j_2(l') e^{jkl'\hat{l}\cdot\hat{r}} dl' = \int_{\frac{-\lambda}{8}}^{\frac{\lambda}{8}} \cos[k(\frac{\lambda}{8} - l')] e^{jkl'\hat{l}\cdot\hat{r}} dl' \\ &= \tfrac{j \sin\theta \sin\phi e^{j\frac{\pi}{4}\sin\theta\sin\phi} + e^{-j\frac{\pi}{4}\sin\theta\sin\phi}}{k(1 - \sin^2\theta \sin^2\phi)} \end{aligned} \tag{5.20}$$

$$G_2(\hat{r}) = \eta I_0 G_{id}(\hat{r}) \tilde{j_2}(k\hat{l} \cdot \hat{r}) = \eta I_0 \frac{-jk}{4\pi} (\cos\theta \sin\phi \hat{\theta} + \cos\phi \hat{\phi}) \tilde{j_2}(k\hat{l} \cdot \hat{r})$$

$$G'_{2A}(\hat{r}) = G_{2A} \cdot 2j \sin(kh \cos\theta) \tag{5.21}$$

$$G'_{2B}(\hat{r}) = G_{2B} \cdot 2j \sin(kh \cos\theta) \tag{5.22}$$

$$G'_{2C}(\hat{r}) = G_{2C} \cdot 2j \sin(kh \cos\theta) \tag{5.23}$$

$$G'_{2D}(\hat{r}) = G_{2D} \cdot 2j \sin(kh \cos\theta) \tag{5.24}$$

Since the central network in Figure 5.7 does not radiate at all, the total far-field in the sum channel end up to be,

$$G^{\Sigma}(\hat{r}) = G'_{1A}(\hat{r}) + G'_{1B}(\hat{r}) + G'_{2C}(\hat{r}) + G'_{2D}(\hat{r}) \tag{5.25}$$

The normalized calculated and simulated patterns in E-plane ($\phi = 90°$) and H-plane ($\phi = 0°$) can be found in Figure 5.11.

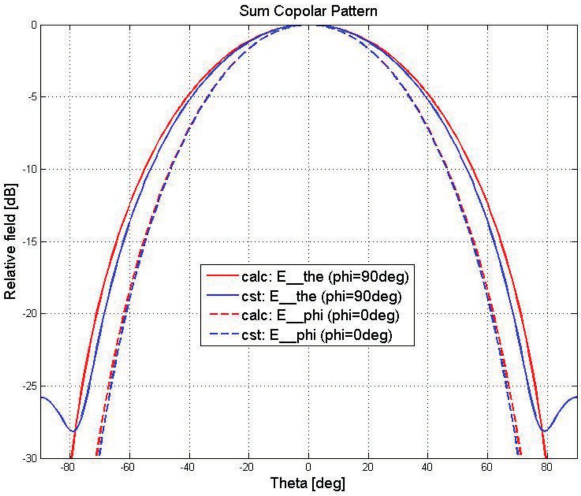

Figure 5.11: Calculated and CST-simulated sum patterns in E and H planes (normalized).

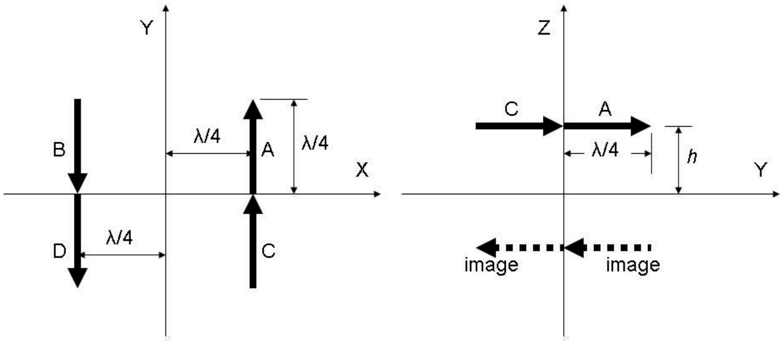

Figure 5.12: Top and side views of horizontal difference channel model.

Horizontal Difference Channel

The horizontal difference channel is modeled in Figure 5.12. The central network in Figure 5.7 functions as two sets of transmission lines too, but with opposite polarization. The network does not radiate either, so the total far-field can be calculated in the following way,

$$G_H^{\Delta}(\hat{r}) = G'_{1A}(\hat{r}) - G'_{1B}(\hat{r}) + G'_{2C}(\hat{r}) - G'_{2D}(\hat{r}) \tag{5.26}$$

The normalized calculated and simulated ϕ-component of electric field in $\phi = 0°$ plane is shown in Figure 5.13.

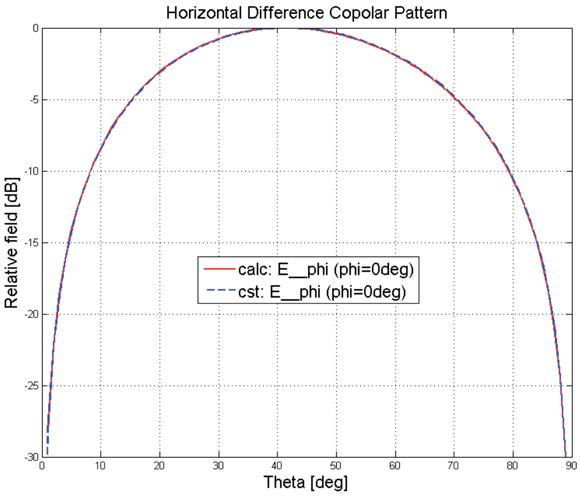

Figure 5.13: Calculated and CST-simulated horizontal difference patterns (normalized).

5.2 Laboratory Demonstration

5.2.1 Network model

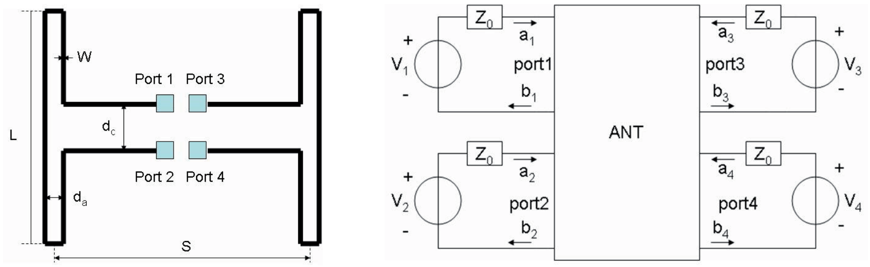
W
Port 1
Port 3
L
d_c
Port 2
Port 4
d_a
S
Z_0
a_1
+
V_1
-
port1
b_1
Z_0
a_2
+
V_2
-
port2
b_2
ANT
Z_0
a_3
port3
b_3
+
V_3
-
Z_0
a_4
port4
b_4
+
V_4
-

Figure 5.14: The equivalent network model of the 4-port folded dipole pair

Figure 5.14 exhibits the simplified diagram of a second laboratory model and its equivalent network model. The dimensions of this model is listed in Table 5.2. In principle, we consider the antenna as four monopoles with four unbalanced coaxial ports. A port is defined between the end of a supporting stripe (central network) and the ground plane, so that there are 4 ports that are designated as port 1-4 in Figure 5.14 and port A, -B, C, -D in Figure 5.15, respectively. The reason why the minus signs are used here is to make the port definitions of the three monopulse modes formed by the Eleven antenna consistent

Table 5.2: Dimensions of the L-band Eleven antenna in Fig. 5.14

Parameters	**Value**
Length of dipole L	100 mm
The height of dipole H	32 mm
Tilted angle α	33°
Width of dipole w	3.5 mm
Thickness of all metal lines t	0.3 mm
Spacing between two parallel dipoles S	130 mm
Arm spacing in folded dipole da	2 mm
Transmission line spacing dc	4 mm

with the traditional definitions for a multi-port monopulse system.

Coaxial-cable model	**Numerical model**	**Port / excitation definitions**		
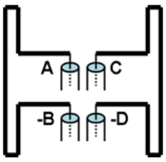	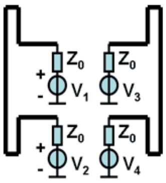 Z0 Z0 + - V1 V3 Z0 Z0 + - V2 V4	**$\sum$ mode excitation**	**Δ_{ver} mode excitation**	**Δ_{hor} mode excitation**
		$\sum$: A+B+C+D	**Δ_{ver}: A+C − (B+D)**	**Δ_{hor}: A+B − (C+D)**
		$V_1=+1$ $V_2=-1$ $V_3=+1$ $V_4=-1$	$V_1=+1$ $V_2=+1$ $V_3=+1$ $V_4=+1$	$V_1=+1$ $V_2=-1$ $V_3=-1$ $V_4=+1$

Figure 5.15: Excitations for 3 modes of the 4-port folded dipole pair

Through different combination of the excitations at each port, the sum mode and two difference modes for both elevation and azimuth planes can be produced, respectively, as briefly summarized in Figure 5.15. As we can see, for example, the antenna is about to work in the sum mode if the voltages at port 1 and 3 are with same amplitude and same phase, while the voltages at port 2 and 4 with the same amplitude but 180° reversal phase. The excitations for the two difference modes can be understood in a similar way.

5.2.2 Feeding network

The port scattering parameters of a multiport network can be found when a single port is excited in presence of all the other ports being passively load-terminated. Besides, it is as well of interest for us to estimate the reflection effect when all of the ports are excited at the same time for generation of the sum or difference beams. According to the equivalent model in Figure 5.14, where a_1, a_2, a_3, a_4 (caused by the source voltage V_1, V_2, V_3, V_4, respectively) represent incident waves while b_1, b_2, b_3 and b_4 represent reflected waves at each port, the total reflection at port 1 can be obtained as follow in (5.27), when a perfect symmetry of the four ports is assumed and the principle of superposition is applied,

$$\begin{aligned}&(S_{11})_{tot} = \tfrac{1}{a_1} \cdot (b_1)_{tot}\\ &= \tfrac{1}{a_1} \cdot (a_1 \cdot S_{11} + a_2 \cdot S_{12} + a_3 \cdot S_{13} + a_4 \cdot S_{14})\\ &= S_{11} + \tfrac{V_2}{V_1} \cdot S_{12} + \tfrac{V_3}{V_1} \cdot S_{13} + \tfrac{V_4}{V_1} \cdot S_{14}\end{aligned} \tag{5.27}$$

This indicates the total reflection, or the total S_{11}, at a specific port is dependent on the port scattering parameters and the relative excitation voltages at different ports. For instance, when the excitations are set as $V_1 = -V_2 = V_3 = -V_4$, a vertically polarized sum beam will be produced and its total S_{11} turns out to be,

$$(S_{11})_{tot}^{\Sigma} = S_{11} - S_{12} + S_{13} - S_{14} \tag{5.28}$$

Similarly, when $V_1 = V_2 = V_3 = V_4$, the elevation difference beam with vertical polarization will be formed and its total S_{11} is,

$$(S_{11})_{tot}^{\Delta_{EL}} = S_{11} + S_{12} + S_{13} + S_{14} \tag{5.29}$$

When $V_1 = -V_2 = -V_3 = V_4$, the azimuth difference beam with vertical polarization will be generated and its total S_{11} becomes,

$$(S_{11})_{tot}^{\Delta_{AZ}} = S_{11} - S_{12} - S_{13} + S_{14} \tag{5.30}$$

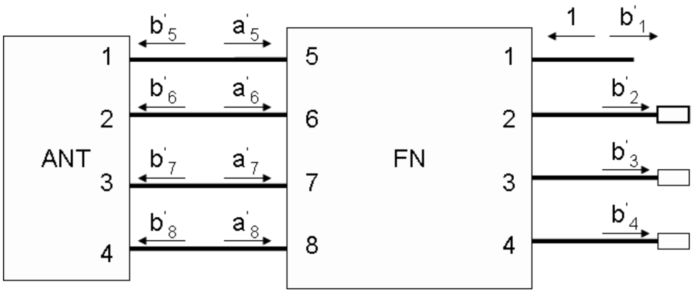

Figure 5.16: The block diagram of the antenna system for any of the monopulse channels

More generally, we may as well consider a system consisting of this 4-port antenna and an 8-port feeding network for any of the monopulse channels, as shown in Figure 5.16. The antenna has a scattering matrix [S] (port S-parameters) at the frequency of interest, while the feeding network has [S']. If ports 2-4 of the feeding network are all match-terminated and an incident wave with magnitude 1 is excited at port 1, the following equations system must be established according to the network theory, in which it is possible for us to solve for b'_1, provided the two scattering matrices are all known.

$$\begin{bmatrix} S_{11} & S_{12} & S_{13} & S_{14} \\ S_{21} & S_{22} & S_{23} & S_{24} \\ S_{31} & S_{32} & S_{33} & S_{34} \\ S_{41} & S_{42} & S_{43} & S_{44} \end{bmatrix} * \begin{bmatrix} b'_5 \\ b'_6 \\ b'_7 \\ b'_8 \end{bmatrix} = \begin{bmatrix} a'_5 \\ a'_6 \\ a'_7 \\ a'_8 \end{bmatrix} \qquad [S'] * \begin{bmatrix} 1 \\ 0 \\ 0 \\ 0 \\ a'_5 \\ a'_6 \\ a'_7 \\ a'_8 \end{bmatrix} = \begin{bmatrix} b'_1 \\ b'_2 \\ b'_3 \\ b'_4 \\ b'_5 \\ b'_6 \\ b'_7 \\ b'_8 \end{bmatrix} \tag{5.31}$$

$$[S'] = \begin{bmatrix} 0 & 0 & 0 & 0 & 0.5 & 0.5 & 0.5 & 0.5 \\ 0 & 0 & 0 & 0 & 0.5 & 0.5 & -0.5 & -0.5 \\ 0 & 0 & 0 & 0 & 0.5 & -0.5 & 0.5 & -0.5 \\ 0 & 0 & 0 & 0 & 0.5 & -0.5 & -0.5 & 0.5 \\ 0.5 & 0.5 & 0.5 & 0.5 & 0 & 0 & 0 & 0 \\ 0.5 & 0.5 & -0.5 & -0.5 & 0 & 0 & 0 & 0 \\ 0.5 & -0.5 & 0.5 & -0.5 & 0 & 0 & 0 & 0 \\ 0.5 & -0.5 & -0.5 & 0.5 & 0 & 0 & 0 & 0 \end{bmatrix} \tag{5.32}$$

We may necessarily define the total S_{11} as the S_{11} at port 1 of the feeding network. If we substitute [S'] in (5.31) with an S-matrix of an ideal 8-port -6 dB 4-way power divider (reciprocal, lossless and matched) for the vertical difference channel (see (5.32)), then we can from (5.31) calculate the total S_{11} of the 4-port antenna itself for the vertical difference channel,

$$\begin{aligned} (S_{11})^{\Delta_{ver}}_{tot} &= \tfrac{1}{4}(S_{11} + S_{12} + S_{13} + S_{14}) + \tfrac{1}{4}(S_{21} + S_{22} + S_{23} + S_{24}) \\ &+ \tfrac{1}{4}(S_{31} + S_{32} + S_{33} + S_{34}) + \tfrac{1}{4}(S_{41} + S_{42} + S_{43} + S_{44}) \end{aligned} \tag{5.33}$$

Similarly, the total S_{11} for the sum and horizontal difference channel can be found as well, respectively,

$$\begin{aligned} (S_{11})^{\Sigma_{ver}}_{tot} &= \tfrac{1}{4}(S_{11} - S_{12} + S_{13} - S_{14}) - \tfrac{1}{4}(S_{21} - S_{22} + S_{23} - S_{24}) \\ &+ \tfrac{1}{4}(S_{31} - S_{32} + S_{33} - S_{34}) - \tfrac{1}{4}(S_{41} - S_{42} + S_{43} - S_{44}) \end{aligned} \tag{5.34}$$

$$\begin{aligned} (S_{11})^{\Delta_{hor}}_{tot} &= \tfrac{1}{4}(S_{11} - S_{12} - S_{13} + S_{14}) - \tfrac{1}{4}(S_{21} - S_{22} - S_{23} + S_{24}) \\ &- \tfrac{1}{4}(S_{31} - S_{32} - S_{33} + S_{34}) + \tfrac{1}{4}(S_{41} - S_{42} - S_{43} + S_{44}) \end{aligned} \tag{5.35}$$

It should be noted that (5.29), (5.28), (5.30) are identical to (5.33), (5.34), (5.35), respectively, provided the antenna has exact symmetry or anti-symmetry between the ports. In practice there will be tolerances which make it necessary to use the complete formulas in (5.33), (5.34) and (5.35). It is important that the dips of the total S_{11} curves of the three channels should be as close to each other as possible, in order for impedance matching at a certain frequency in all channels. Moreover, it should be noted that good symmetry in geometry and excellent balance in excitations are highly beneficial to this multi-port antenna.

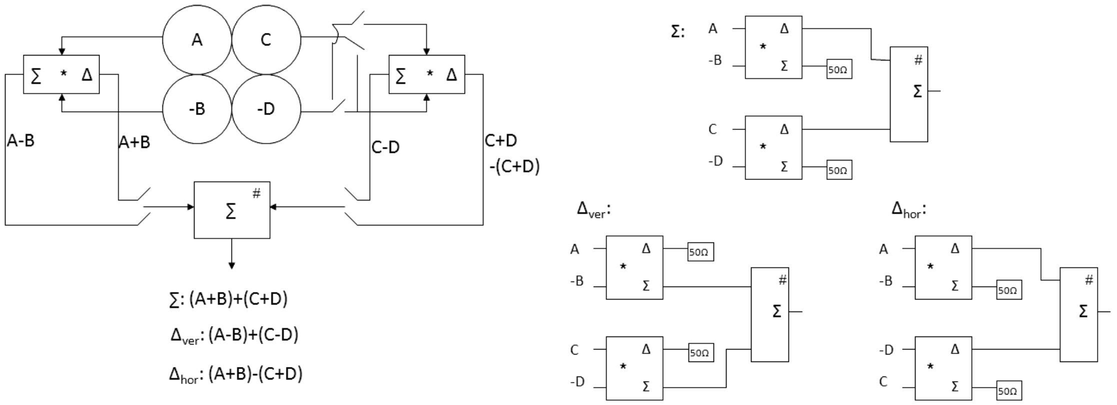

Figure 5.17: The principle diagram (left) and the block diagrams of the feeding (comparator) networks (right). Note that the blocks marked with "*" are 180° hybrids, and the blocks marked with "#" are power dividers.

As for our lab model, a comparator network, of which the principle diagram is shown in Figure 5.17 (left), is utilized to handle the received signals from each monopole in order to form the three different channels. As can be seen in Figure 5.17 (right), it consists of a power divider, two 0°/180° hybrids, several coaxial cables and standard loads, of which three different layouts are shown for the three channels. In our practice, all of them are configured manually.

5.2.3 Feed without reflector

The simulated curves in Figure 5.18 show how the port scattering parameters and the total S_{11} parameters of the three channels vary with frequency. The total S_{11} parameters are better than -10 dB for all the three channels within a narrow band in the range 1.54-1.58 GHz.

The co- and cross-polar patterns of the sum beam in 0°/45°/90° ϕ-planes are shown in Figure 5.19. It can be seen that the co-polar sum patterns have a directivity of around 11 dBi,

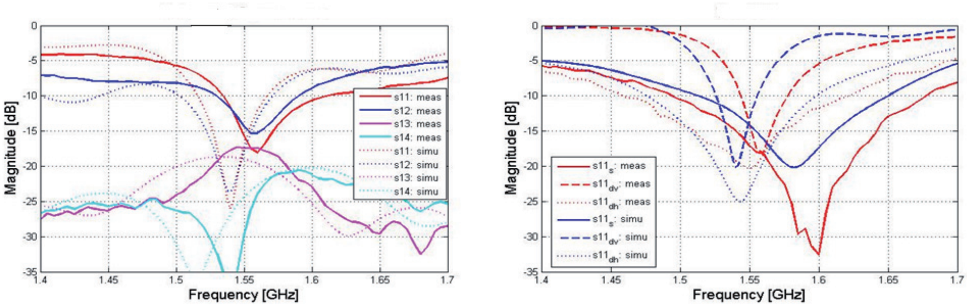

Figure 5.18: Port S-parameters magnitude in dB (left); total S11 magnitude in dB for sum and two difference channels (right)

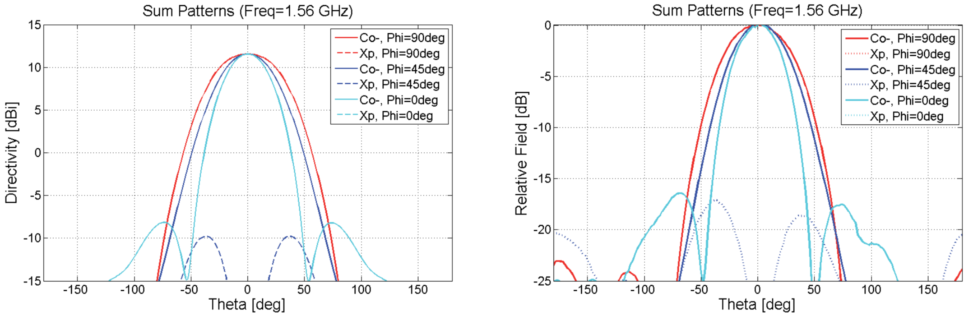

Figure 5.19: Simulated (left) and measured (right) co- and cross-polar components of sum beam

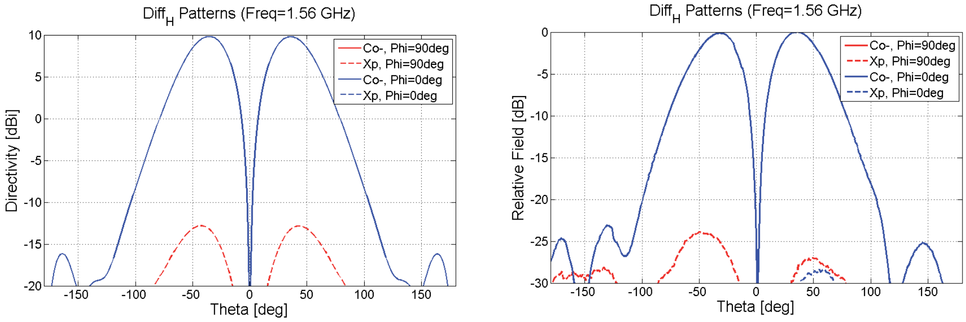

Figure 5.20: Simulated (left) and measured (right) co- and cross-polar components of horizontal difference beam

and the cross-polar level in the 45° plane is better than -17 dB. Figure 5.20 shows both the co- and cross-polar components of the horizontal difference beam, in which there exists a

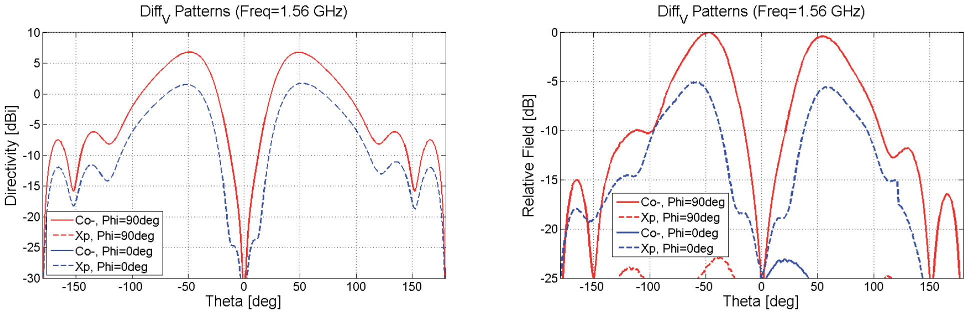

Figure 5.21: Simulated (left) and measured (right) co- and cross-polar components of vertical difference beam

null in the centre (θ=0). It can be further observed that the co-polar (vertical) component in the horizontal tracking plane is much stronger than the cross-polar components, which exhibits a good capability of tracking beacon signals with vertically linear polarization in the horizontal plane. As for the vertical difference beam shown in Figure 5.21, there is also a null in the center and the co-polar component in the vertical tracking plane is 5-8 dB higher than the cross-polar component when θ is between 25° and 50°. For smaller θ the difference is smaller, and the result of this on tracking accuracy needs to be investigated further by studying the performance of the feed in reflector.

5.2.4 Feed with reflector

First, the simulation of the sum and difference patterns of the Eleven antenna itself is carried out in CST MWS. Then, both θ and ϕ components of the far field are extracted from CST and imported into an in-house MATLAB routine, in which the far field after reflection can be computed by assuming Geometrical Optics (GO) reflection at the surface of the reflector (see Appendix B). The primary-fed paraboloidal reflector in our calculation has parameters as shown in Table 5.3.

Table 5.3: Parameters of the paraboloidal reflector

Parameters	**Value**
Diameter of reflector (D)	2.3 m
Area of reflector (A)	4.15 m^2
Operating wavelength (λ)	0.192 m
Half-subtended angle (θ_0)	60°
Focal-length over diameter (F/D)	0.433

According to $D_m = 4\pi A/\lambda^2$, the maximum directivity (D_m) from such an aperture at 1.56 GHz (λ=0.192 m) can be achieved up to around 31.3 dBi, if it is excited by a field with uniform amplitude and constant phase over the whole aperture. The difference of the actually achieved directivity (in dBi) and the above theoretical maximum value (in dBi) is usually used to evaluate the total aperture efficiency.

The sum channel is the communication channel for the satellite links, and the aperture efficiency as well as the return loss should be good enough to meet specific system requirements. The two difference channels take on the main task of monopulse tracking. The most important issues for them include that there should be a deep null of the co-polar component on the bore-sight axis, and meanwhile the cross-polar level should be acceptably low.

Sum (Σ) channel

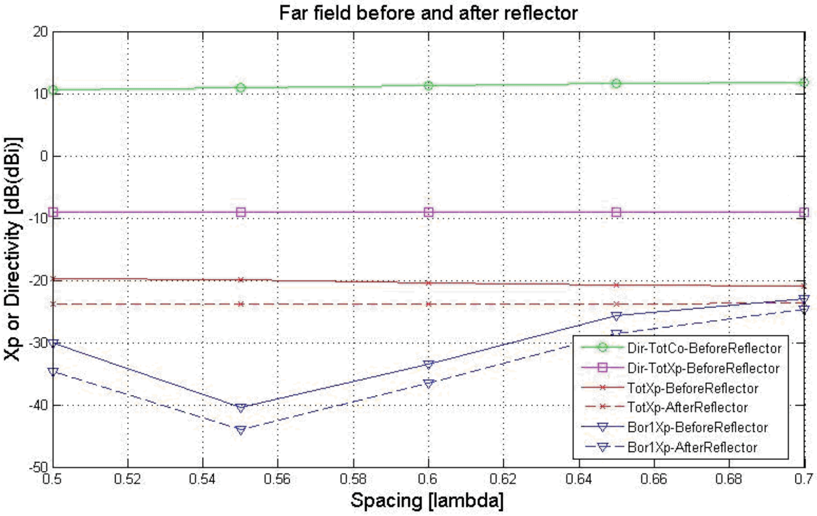

Figure 5.22: Directivity vs. spacing (S) for Σ channel

The entire far field function of a BOR1 (refer to Appendix A) antenna can be constructed merely from patterns in its two principal planes. The BOR1 efficiency is defined as the ratio of the power in the BOR1 component and the total radiated power, as specified in Appendix A, indicating how closely the far-field function resembles a BOR1 type far-field function, as well as quantifying how much power is lost in the part of the far field that is not of BOR1 type. If a parabolic reflector is fed by a BOR1 beam extracted from the total far-field beam, the aperture efficiency can be factorized in a number of sub-efficiencies,

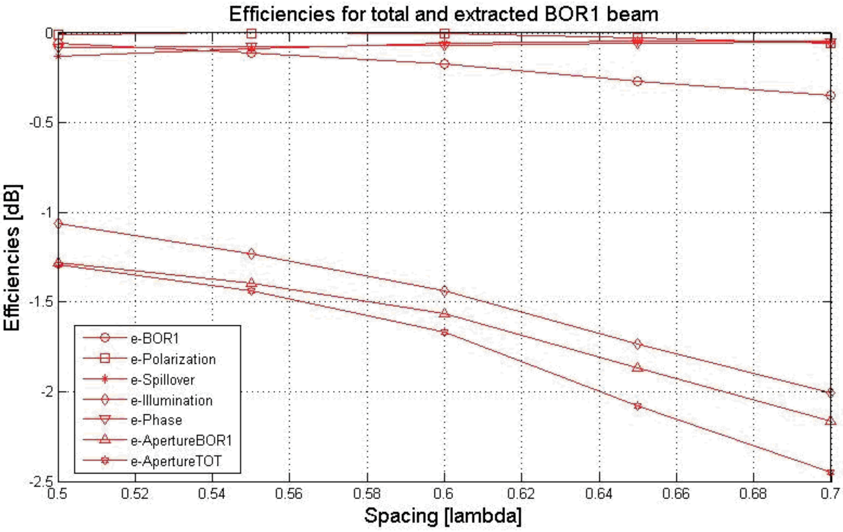

Figure 5.23: Efficiencies vs. spacing (S) for Σ channel

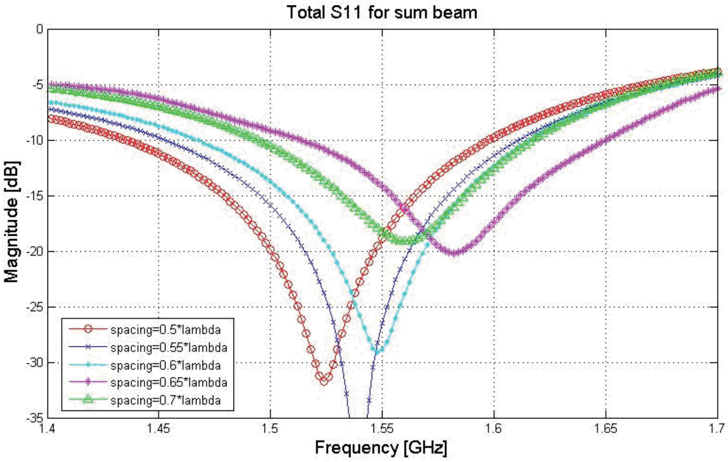

Figure 5.24: Total S_{11} vs. spacing (S) for Σ channel

including illumination efficiency, polarization efficiency, spill-over efficiency, and phase efficiency. All of the sub-efficiencies have been formulated in Appendix A.

Several simulations have been done to study how the 4-port Eleven antenna performs under different spacings between the parallel folded dipoles (S). It can be seen from Figure 5.22 that for the total far-field beam before reflection, the cross-polar level decreases

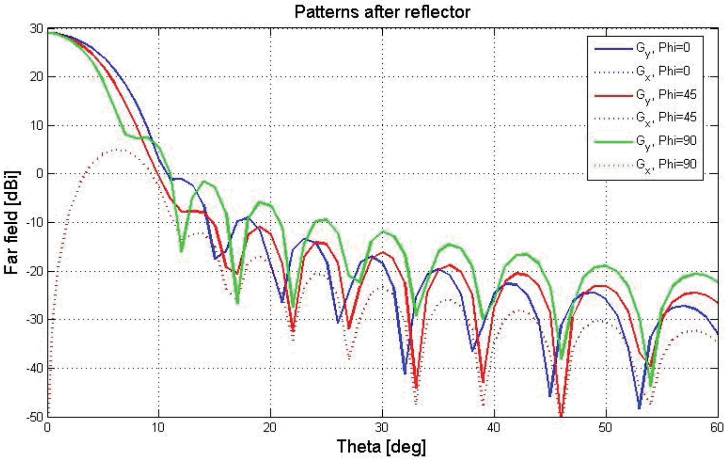

Figure 5.25: Sum beam after reflection for Σ channel (spacing S=0.65λ)

slightly as the spacing increases, since the directivity of the co-polar pattern increases slightly while the directivity of the cross-polar pattern keeps almost constant. However, for the extracted BOR1 beam, the cross-polar level either before or after reflection will reach a peak when the spacing equals about 0.55λ, where the patterns in two principal planes are roughly identical. The cross-polar level will become worse as the spacing increases further. Besides, the difference between the cross-polar level before and after reflection keeps decreasing as the spacing increases.

The aperture efficiencies for both the total and extracted BOR1 beams, as well as all sub-efficiencies, are exhibited in Figure 5.23. There is a clear trend indicating that the BOR1 efficiency and the aperture efficiencies decrease as the spacing increases. Figure 5.24 shows the total S_{11} for the sum channel with respect to several cases of different spacing. Sum patterns after reflection in ϕ=0, 45, 90° planes are plotted in Figure 5.25. The cross-polar level is better than -25 dB.

Horizontal difference (Δ_h) channel

The horizontal difference channel is expected to track the vertical-polarized beacon signal in the horizontal plane (ϕ=0°). Its patterns after reflection in ϕ=0, 45, 90° planes are shown in Figure 5.27. There is a deep null on the bore-sight axis and the cross-polar levels are low neighboring the null in all ϕ planes. Especially, the pattern in the horizontal plane has a very low cross-polar level. The total S_{11} for the horizontal difference channel with respect to different spacing are shown in Figure 5.26.

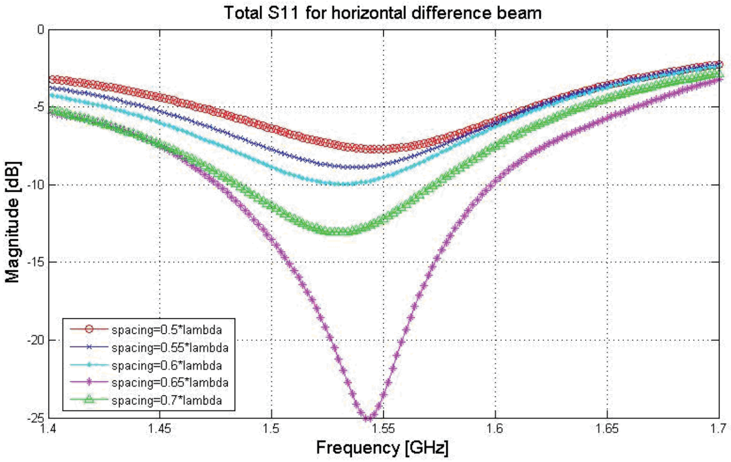

Figure 5.26: Total S_{11} vs. spacing (S) for Δ_h channel

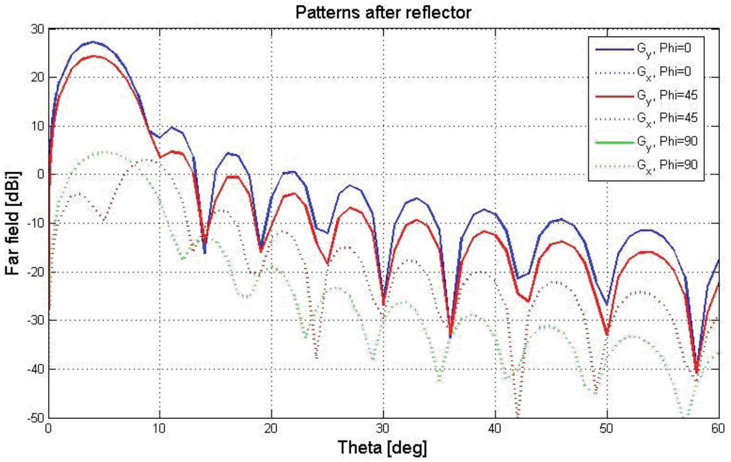

Figure 5.27: Horizontal difference beam after reflection for Δ_h channel (spacing S=0.65λ)

Vertical difference (Δ_v) channel

The vertical difference channel is expected to track the vertical-polarized beacon signal in the vertical plane (ϕ=90°), and its patterns after reflection in ϕ=0, 45, 90° planes are shown in Figure 5.29. As clearly seen, there is also a steep null in the center; however, although the pattern in the vertical plane has very low cross-polar level, there is a significant cross-

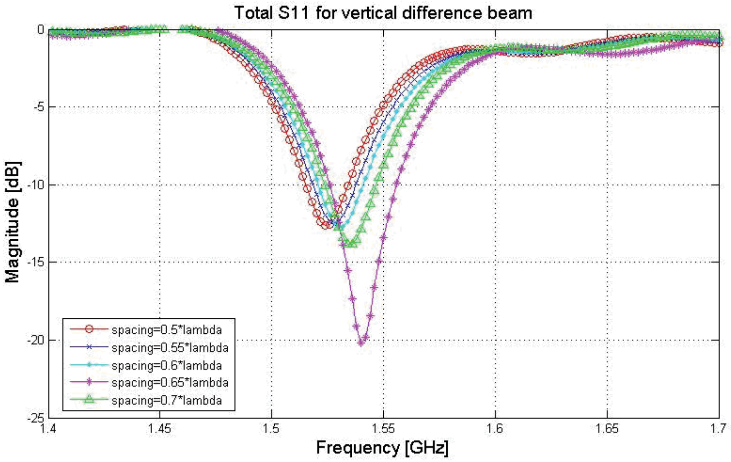

Figure 5.28: Total S_{11} vs. spacing (S) for Δ_v channel

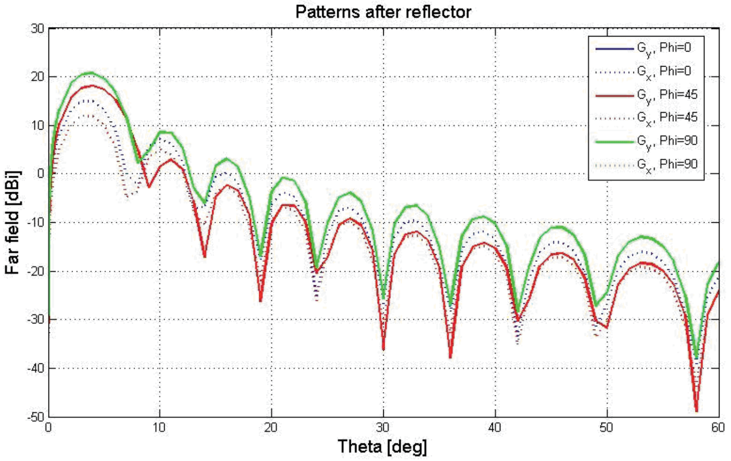

Figure 5.29: Vertical difference beam after reflection for Δ_v channel (spacing S=0.65λ)

polar level in ϕ=0/45° plane, which implies a possible tracking ambiguity. The total S_{11} for the vertical difference channel with respect to different spacing are shown in Figure 5.28.

By comparison between Figure 5.23, 5.24 and 5.25, we can find that when the spacing is about 0.65λ, the total S_{11} parameter of the sum channel can be better than -10 dB over both the uplink and the downlink bands of the L-band for satellites. Meanwhile, the total S_{11} of either of the two difference channels can be no worse than -20 dB.

5.3 Review of a Dual-Band Feed Based on Choke Horn and Circular Eleven Antenna

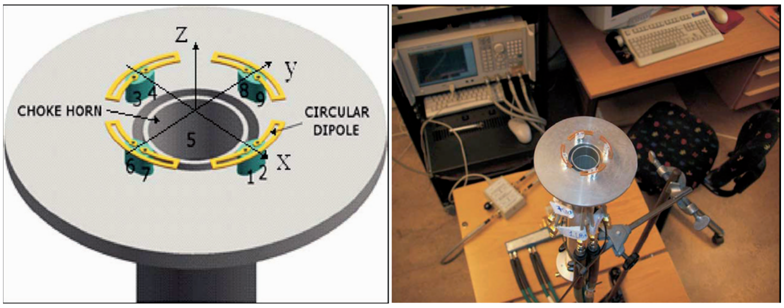

Figure 5.30: C/Ku-band feed prototype geometry [1]

On top of the straight version of single band Eleven antenna mentioned above, there recently come some other designs on, for instance, its circular version. In [1], a novel dual-band feed for reflector antennas is addressed. As exhibited in Figure 5.30, this feed is a combination of a circular Eleven feed for C band (6.2-7 GHz) and a compact choke horn for Ku band (10-15 GHz).

Table 5.4: Measured performance of C/Ku-band feed [1]

Frequency	**6 GHz**	**6.5 GHZ**	**10.5 GHz**	**15 GHZ**
Peak XP sidelobe level (dB)	-22	-20	-13	-17
Reflection Coefficient (dB)	-8	-16	-12	-25
Coupling between dual bands (dB)	<-40	<-40	-18	-23
Feed Aperture Efficiency @ 50° (dB)	-1.83	-2.89	-2.06	-2.11
Total Feed Efficiency @ 50° (dB)	-2.65	-3.02	-2.39	-2.15

The combined feed has been characterized in terms of total feed efficiency of reflector antenna and coupling coefficient of C and Ku bands over all operating frequencies. The measurement results of the dual-band feed performance are listed in Table 5.4, while the radiation patterns are plotted in Figure 5.31. In brief conclusion, this dual-band feed is compact and low-cost, and can be a good candidate for satellite terminals as well as other applications.

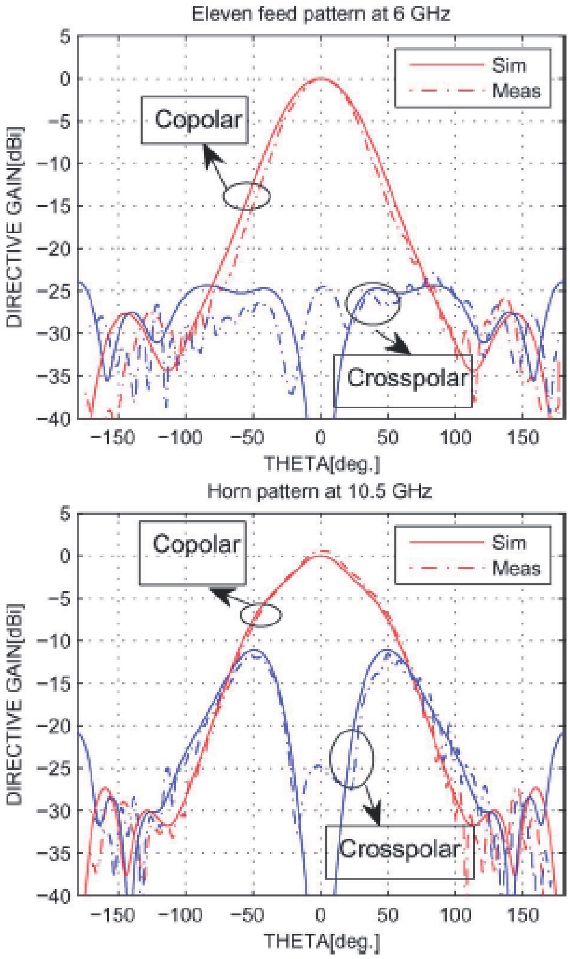

Figure 5.31: Simulated and measured radiation patterns of the Eleven feed and choke horn in ϕ=45° plane at 6 and 10.5 GHz [1].

5.4 Summary of Chapter 5

A 4-port linearly-polarized L-band Eleven antenna is investigated on the communication and monopulse tracking capability for satellite terminals. An impedance model for the sum channel and two radiation models for the sum and the horizontal difference channels have been described. What is more, a study on the spacing between parallel dipoles, which influences the total reflection coefficient as well as the radiation characteristics of the 3 monopulse channels, is also carried out. As can be observed, the vertical difference channel is prone to a much narrower impedance bandwidth compared to the other two; the spacing of 0.65λ (λ is the operating wavelength), which by the way is a bit larger than 0.5λ, is approximately the optimum for all the 3 channels to match simultaneously. However, the aperture efficiency of a reflector fed by this Eleven antenna decreases as the spacing increases over the observed range 0.50-0.70λ. As a result, a compromise must be made when the spacing is chosen to obtain acceptable matching and radiation characteristics at the same time.

Concerning the tracking capability, as far as I feel, the horizontal difference channel is more suitable for tracking due to its deep null and very low cross-polar level, whereas the vertical difference channel is inferior because of its high cross-polar level closely around the null except for the vertical plane. However, the former can be regarded as the main (first) tracking channel and the latter as the auxiliary (second) tracking channel; through proper procedures and algorithms, it is possible to realize the monopulse tracking for linearly-polarized signals in two dimensions by using the 4-port Eleven antenna. Regarding this matter, we are proposing an idea of sequential tracking procedure. Consider a point target at the origin of its own coordinate system, whose horizontal and vertical axes are parallel to those in the coordinate system of the antenna. Since the horizontal difference channel has more sensitive null and lower cross-polar level, it can be used in the first place when the tracking procedure starts. Ideally, it will align the tracking beam along the horizontal direction of the target, until it reaches the vicinity of the vertical axis of the target. Then the vertical difference channel can be used to perform the tracking along the vertical direction of the target, as it has a 'clean' pattern, almost free of cross-polar component, in the vertical plane. These two steps can be repeated until the tracking accuracy is achieved.

Chapter 6

Wide Band Eleven Antennas As Feed For Radio Telescopes

The Eleven feed, featured as a low-profile, logarithmic-periodic and ultra wideband antenna, has during the past few years been developed at Chalmers University of Technology in Sweden. It is referred to as the Eleven feed because its basic geometry is two parallel folded dipoles half-wavelength apart above a ground plane, and it can be used over more than a decade bandwidth with 11 dBi directivity by extending the basic configuration logarithmically. The Eleven feed can be used in both linear and dual polarizations, and its phase center changes so little with frequency and the 10 dB semi-beamwidth is $50\sim60^\circ$ over the entire frequency band. Therefore, it is suitable as feed for reflector antennas, in particular when they are primary-fed.

This chapter consists of five sections. The first section describes my own work at NTNU on designing and simulating a linearly-polarized and a dually-polarized triple-bandwidth Eleven model. The following three sections are mostly based on the research results of wideband Eleven feed achieved by the Antenna Group at Chalmers. In the last section, a novel circular version of wideband Eleven Feed is reported, based on a joint project between NTNU and Chalmers.

6.1 Triple Bandwidth Simulation Models

In our practice, CST MWS are preferably used to simulate Eleven antennas with a moderate number of folded dipole pairs. Because the time domain solver in CST is based on FDTD, the simulation may consume too long time and require too large memory capacity if the antenna model is huge in terms of the minimum wavelength. In particular, long simulation time should be avoided when an optimization procedure, which requires hundreds or even thousands of runs of simulation, is performed. To start with, we choose to study simulation models with 8 pairs of folded dipoles.

6.1.1 Linearly Polarized Model

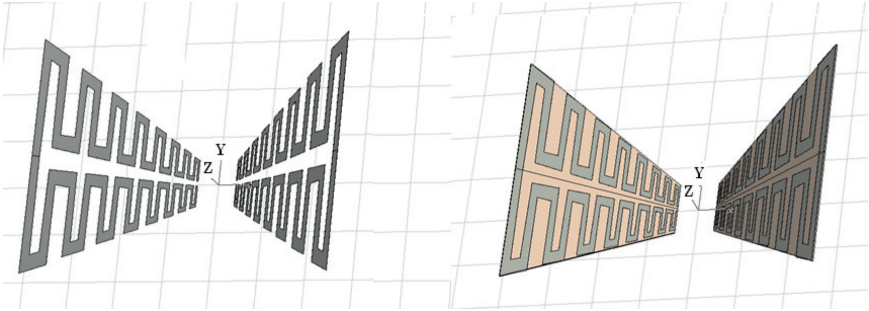

Figure 6.1: Linearly polarized simulation models without (left) and with (right) PCB over an infinite ground plane (8-pair folded dipoles on one petal).

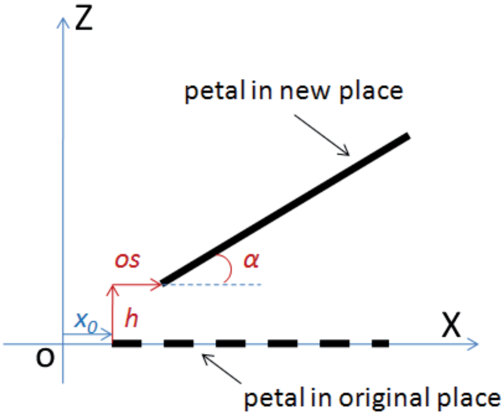

Figure 6.2: Simple side view graph of one antenna petal after displacement and rotation (X_0 is equivalent to $-Z_0$ in Figure 4.3).

As described in Section 4.2.2, the geometry of a fully scaled log-periodic folded dipole array (LPFDA) can be defined by 10 parameters. In order to construct a complete Eleven antenna, which contains two or four identical LPFDA petals leaning over a ground plane, 3 additional parameters are thus introduced as follows (refer to Figure 6.2):

Table 6.1: Normalized Parameters For Eleven Simulation Models

Parameters ($\lambda_{geo-min}$=60 mm)	**1-Pol**	**2-Pol**
$X_0/\lambda_{geo-min}$	0.2929	0.2594
$L/\lambda_{geo-min}$	0.1465	0.1335
$w/\lambda_{geo-min}$	0.0387	0.0381
$wa/\lambda_{geo-min}$	0.0220	0.0247
$wb/\lambda_{geo-min}$	0.0239	0.0279
$wc/\lambda_{geo-min}$	0.0292	0.0297
$da/\lambda_{geo-min}$	0.0137	0.0107
$db/\lambda_{geo-min}$	0.0110	0.0094
$dc/\lambda_{geo-min}$	0.0175	0.0129
k	1.2397	1.3149
$os/\lambda_{geo-min}$	-0.1398	-0.0825
$h/\lambda_{geo-min}$	0.0385	0.1168
α (^{o})	34.708	29.698

$*$ offset *os*: the displacement of the antenna petal along the positive x-axis.
$*$ height *h*: the distance between the shortest folded dipole and the ground plane.
$*$ rotated angle α: the angle between the antenna petal plane and the ground plane.

In order to obtain acceptable radiation patterns, *os*, α together with other parameters, e.g. X_0, are empirically limited within a predefined range where they can be randomly chosen, so that the spacing between any parallel dipoles is not far different from half the corresponding geometrical wavelength. Similar to that in Chapter 4, the Genetic Algorithm (200 population and 5 generations) linked with CST MWS is applied to perform the optimization for the reflection coefficient. The best result occurs when the 13 parameters, 11 of which in terms of the geometrical minimum wavelength $\lambda_{geo-min}$, are configured as listed in Table 6.1 (first column of data).

Shown in Figure 6.1 (left) is a linearly polarized simulation model made of only metal strips, where the arms of folded dipoles are parallel to the y-axis, and the whole structure is over an infinite electric ground plane that has the z-axis as the normal. The yz- and xz-plane are during simulation set as magnetic and electric symmetrical planes, respectively. A discrete port is used as feed across the gap of one of the innermost folded dipoles. Shown in Figure 6.1 (right) is the second linearly polarized model. It has the same geometry as the first one, but with a printed circuit board (PCB) substrate on which the metal strips are printed. The thickness of all the metal strips is 35 μm, and Rogers RT6002 is chosen as the dielectric substrate (ϵ_r = 2.94, $\tan\delta$ = 0.0012, thickness = 3 mm) in the simulation. We would hereby like to call these two ideally-fed antenna models (over an infinite ground plane) ideal models. In contrast, a real model with practical feed scheme will be elaborated later in this section.

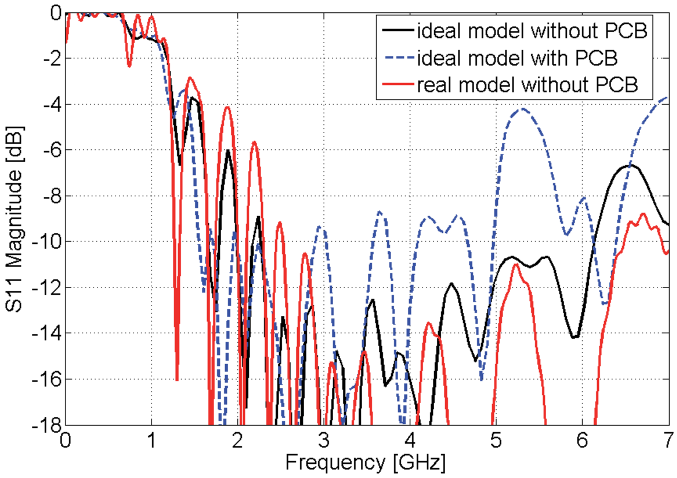

Figure 6.3: CST-simulated S_{11} of linearly polarized ideal models without and with PCB (reference: 200 Ω); CST-simulated S_{11} of a linearly polarized real model without PCB (fed by pairs of 50 Ω coaxial cables).

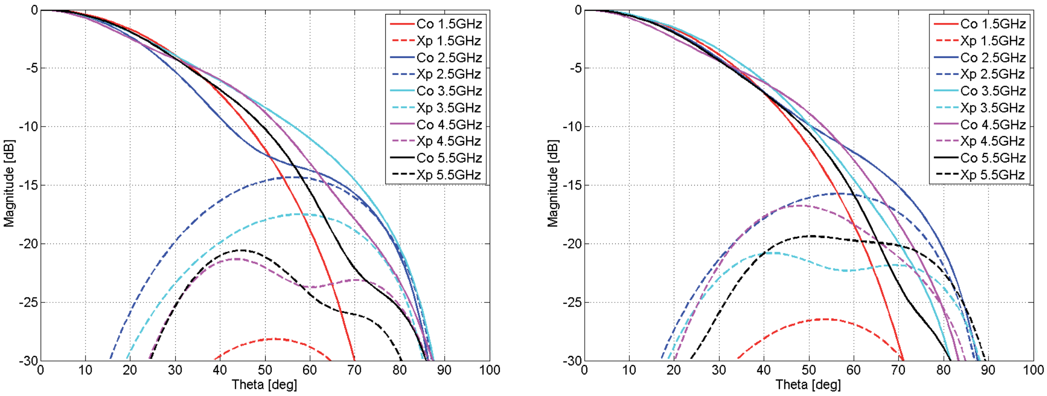

Figure 6.4: CST-simulated BOR1 patterns (in ϕ=45^o plane) of linearly polarized ideal models (over infinite ground plane) without (left) and with (right) PCB.

Figure 6.3 shows the simulated S_{11} (reference: 200 Ω) of the linearly polarized ideal models without and with the PCB substrate. For the model without PCB, the bandwidth ratio is around 3:1 as S_{11} is largely better than -10 dB between 2.0 and 6.1 GHz. In the case of the antenna printed on PCB, in contrast, S_{11} is largely better than -10 dB between 1.6 and 5.0 GHz. Obviously, the matching is a bit worse and the bandwidth is shifted

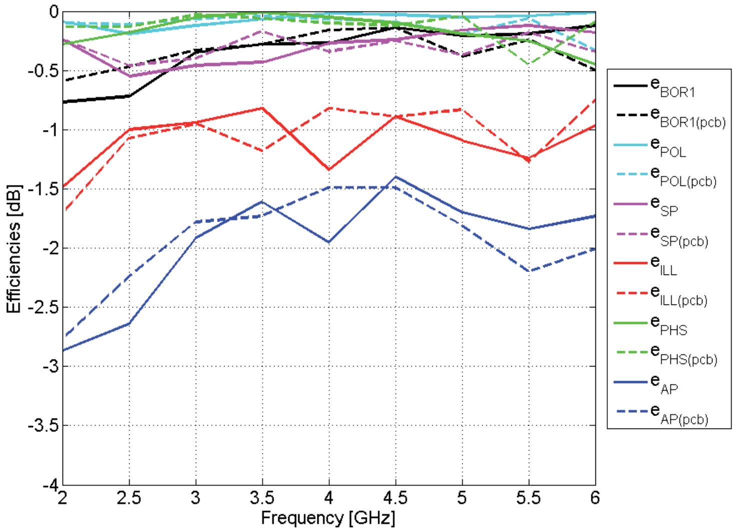

Figure 6.5: Calculated efficiencies of linearly polarized ideal models without and with PCB (half subtended angle = 60^o). Plotted at an interval of 0.5 GHz.

downwards; however, the bandwidth ratio is still around 3:1.

Figure 6.4 compares the BOR1 patterns in ϕ=45^o plane of the above-mentioned two simulation models in the frequency range of 1.5$\sim$5.5 GHz. The BOR1 patterns at one single frequency are derived by first Fourier-transforming the simulated total patterns and then manipulating the far-field functions in the E and H planes. As can be seen, the 10 dB semi-beamwidths are largely in the range of 50$\sim$$60^o$, and the cross-polar levels are largely better than -15 dB in both cases. The copolar directivities of the BOR1 component can be found in Figure 6.10 (left); they are quite constant around 11 dBi over the bandwidth. In addition, Figure 6.5 illustrates the calculated efficiencies when the two simulation models feed a parabolic reflector with a half subtended angle 60^o. It is observed that the BOR1 efficiency is better than -0.7 dB over the whole shown spectrum, and the aperture efficiency is better than -2.5 dB and averaged around 1.8 dB over the most of the whole band. In particular, the difference of the efficiencies in the two cases is quite small. It can be estimated from this study that the PCB substrate with a few mini-meters thickness seems not to greatly affect the radiation properties.

It should be noted that the preceding results are derived through ideal models. Since the infinite ground plane is unavailable and the 200 Ω feedline is not so common in reality, it is of great interest to study the feed details in practice. A prime task is to find a way of matching one antenna petal to a pair of standard 50 Ω coaxial cables in a balanced man-

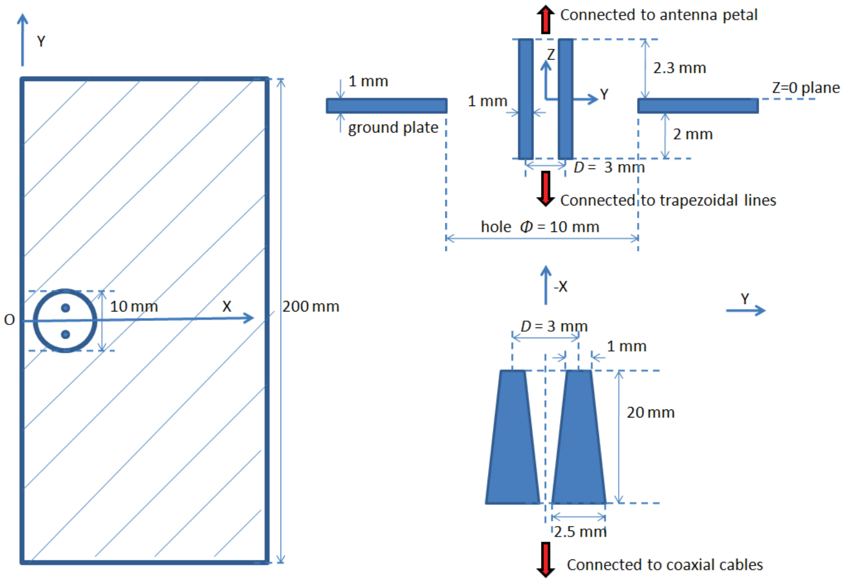
Y
O
10 mm
X
200 mm
1 mm
ground plate
1 mm
Connected to antenna petal
Z
Y
2.3 mm
Z=0 plane
2 mm
D = 3 mm
Connected to trapezoidal lines
hole Φ = 10 mm
-X
Y
D = 3 mm
1 mm
20 mm
2.5 mm
Connected to coaxial cables

Figure 6.6: Drawing of symmetrical half of the real feed with regard to half ground plane (some dimensions are not in right proportion). Top view (left) and side view (upper right) of the hole and the transmission pins; top view (lower right) of the parallel trapezoidal matching lines.

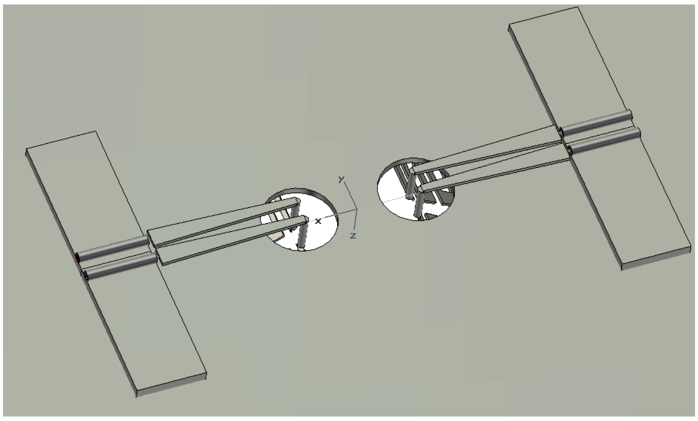

Figure 6.7: Real feed model in CST. The trapezoidal lines are connected with a pair of 50 Ω coaxial cables that are shorted to the ground plane.

ner, while the other petal is fed by the same means; in particular, the matching network is preferably to be installed on the back side of the ground plane. Note that the same electric and magnetic symmetrical planes as those in the previous ideal cases are used in all simulations to follow.

A proposed matching scheme is illustrated in Figure 6.6 and Figure 6.7. First of all, we choose a square (200 mm × 200 mm × 1 mm) metal plate as the finite-sized ground plane. Its side length 200 mm (1.33 × $\lambda_{2\text{GHz}}$, $\lambda_{2\text{GHz}}$ = 150 mm) is according to our experience sufficiently large to maintain the impedance and radiation properties in the case of an ideal ground plane. In order to put the matching network on the back side of the ground plane, we drill two holes (diameter = 10 mm) symmetrical with the center line of the plate, through which two pairs of cylindrical transmission pins (perpendicular to the ground plate) can reach out to the back side.

A pair of parallel metal pins can be thought of as a transmission line with circular cross section, whose characteristic impedance can be found in formula (5.3). In this case, the impedance of the antenna petal is approximated by 200 Ω over the whole bandwidth; and the separation of the pins (D) is set as 3 mm, since the feed gap of the innermost folded dipole is around 3 mm. Then, the diameter of the pins should be about 1.1 mm according to (5.3). However, it can merely be a good first try in that there are objects, such as the hole edge and the ground plate, in the close proximity. The diameter of the pins is finally tuned to be 1 mm. The length of the pins need to be treated carefully as well. Since the height (h) of the feed gap of the antenna petal is around 2.3 mm, the length of the pins *above* the ground plate is no doubt the same as h. The length of the pins *underneath* the ground plate (2 mm) is derived through a number of runs of simulation, in which we aim to make the port of the parallel pins beneath the plate match to 200 Ω.

Parallel trapezoidal metal lines are used to perform the impedance match from 200 Ω down to 100 Ω over the bandwidth (2∼6 GHz). The top side, bottom side and the height of the trapezoid are 1 mm, 2.5 mm and 20 mm, respectively. The thickness of the strips is 0.5 mm. A pair of 50 Ω coaxial cables, placed on top of a shorting brick (height 1.5 mm), are connected to the bottom sides of a pair of trapezoidal lines. The coaxial cables are modeled in CST as follows:

radius of the inner cylinder: 0.15 mm
radius of the outer cylinder: 0.50 mm
Teflon (PTFE) in between: ϵ_r = 2.08, loss free
separation between the paired cables: 3 mm

The return loss at a cross section of a coaxial cable is, together with others, plotted in Figure 6.3. It is observed that the S_{11} is largely better than -10 dB between 2.2 and 6.4 GHz. As the finite-sized ground plate with small holes and the real feed do not significantly change the radiation properties, we choose not to present the far fields of the practical model here.

6.1.2 Dually Polarized Model

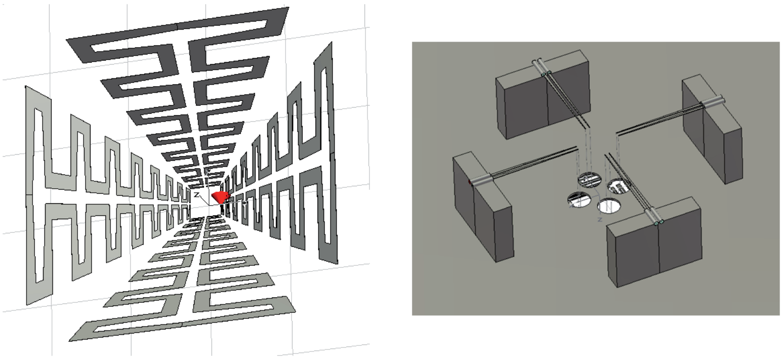

Figure 6.8: Dually polarized ideal model without PCB over an infinite ground plane; real feed model in CST (the trapezoidal lines are connected with a pair of 75 Ω coaxial cables that are shorted to the ground plane).

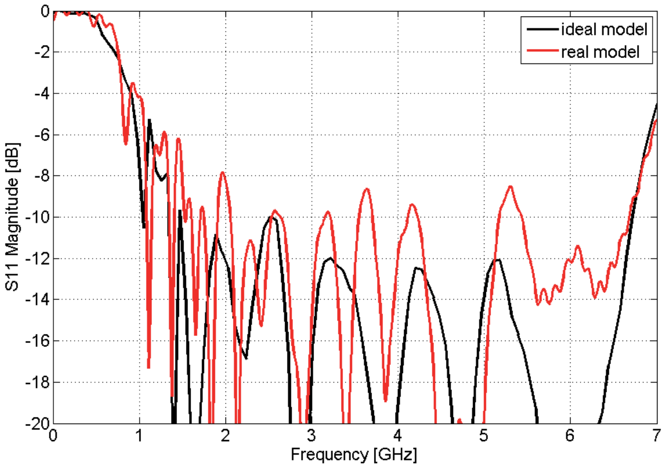

Figure 6.9: CST-simulated S_{11} of a dually polarized ideal model (reference: 300 Ω) and a real model (fed by pairs of 75 Ω coaxial cables).

The dually polarized model can readily be constructed by adding two more identical petals, which located in the orthogonal azimuth plane relative to the original two petals. However, the previous single polarized model can not be directly developed into a 4-petal dually polarized model, because the distance between the two innermost folded dipoles happens to be shorter than the length of them; the coplanar 90^o rotationally symmetric new petals will intersect the original two. To solve this problem, an extra constraint is

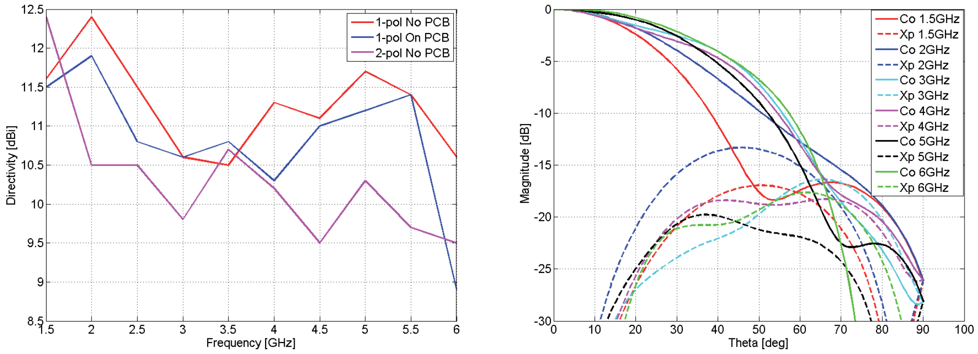

Figure 6.10: Left: Simulated BOR1 copolar directivities of the three Eleven simulation models; Right: CST-simulated BOR1 patterns (in ϕ=45^o plane) of dually polarized ideal model (over infinite ground plane).

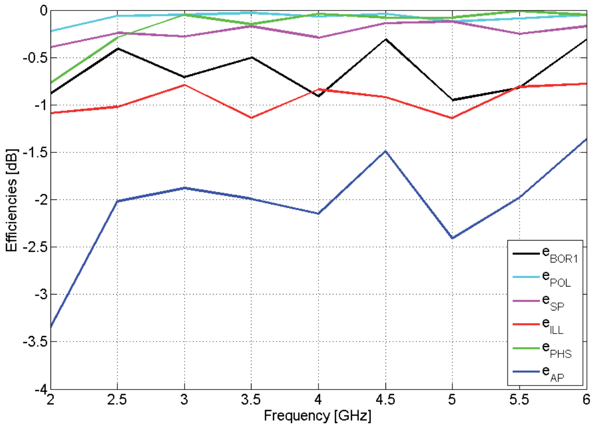

Figure 6.11: Calculated efficiencies of dually polarized Eleven ideal model (half subtended angle = 60^o). Plotted at an interval of 0.5 GHz.

added in the optimization procedure to guarantee a sufficient space between the innermost folded dipoles. This modified procedure is used to search the geometrical parameters that give an optimal return loss spectrum. The most favorable result occurs when the 12 parameters are set as listed in Table 6.1 (second column of data). Shown in Figure 6.8 (left) is a dually polarized simulation model made of only metal strips over an infinite electric ground plane. The coordinate system and the symmetrical planes are the same as those in the previous section.

Figure 6.9 shows the simulated S_{11} of the dually polarized ideal model without PCB substrate. Note the reference is 300 Ω here; because by checking the Smith Chart during the search procedure, we have found that the impedance tends to center around 300 Ω. As we can see, the impedance bandwidth ratio is around 4.4:1 as S_{11} is better than -10 dB between 1.5 and 6.6 GHz.

Similarly, the practical feed details of a real model are studied as well. As shown in 6.8 (right), the feed scheme is in principle the same as that in the previous linearly polarized case. In this case, however, the impedance of the antenna petal is approximated by 300 Ω over the whole bandwidth. The feed gap of the innermost folded dipole is only 2 mm, and this will leave limited room for the trapezoids to flare out. Since it seems difficult to match 300 Ω down to 100 Ω by using parallel trapezoidal matching lines in this case, we otherwise choose to match down to 150 Ω through the same scheme, where a pair of 75 Ω cables are then required. The values of the structural parameters are listed below:

$\star$ Hole and transmission pins:
hole radius: 5 mm
pin radius: 0.1 mm
pin length: 7 (above) + 20 (underneath) = 27 mm
pins separation:2 mm
$\star$ Trapezoidal matching lines:
top side: 0.2 mm
bottom side: 1.1 mm
height: 40 mm
thickness: 0.2 mm
separation: 2 mm
$\star$ 75 Ω coaxial cables:
radius of the inner cylinder: 0.15 mm
radius of the outer cylinder: 0.90 mm
Teflon (PTFE) in between: ϵ_r = 2.08, loss free
separation: 2 mm

The simulated return loss of the real model is presented in Figure 6.9 as well. It can be seen that S_{11} is better than -8 dB between 1.5 and 6.6 GHz, and better than -10 dB over the most of this bandwidth. The BOR1 copolar directivities of the dually polarized simulation model can be found in Figure 6.10 (left); they are quite constant around 10 dBi between 2.0 and 6.0 GHz. Figure 6.10 (right) shows the BOR1 patterns in ϕ=45^o plane within the frequency range of 1.5$\sim$6.0 GHz. As can be seen, the 10 dB semi-beamwidths are in the range of 50$\sim$60^o while the cross-polar levels are better than -13 dB between 2.0 and 6.0 GHz. Figure 6.11 illustrates the calculated efficiencies when this model feeds a parabolic reflector with a half subtended angle 60^o. The BOR1 efficiency varies around -0.65 dB, and the aperture efficiency is largely better than -2.5 dB and averaged around

-2.0 dB over the bandwidth ranging from 2.0 to 6.0 GHz. According to the simulation results, this dually polarized Eleven model (8 folded dipoles in one petal) seems suitable as feed for reflectors (with half subtended angle 50∼60°) over a triple bandwidth, i.e., 2.0∼6.0 GHz.

6.2 Review of Wide Band Models Below 3 GHz

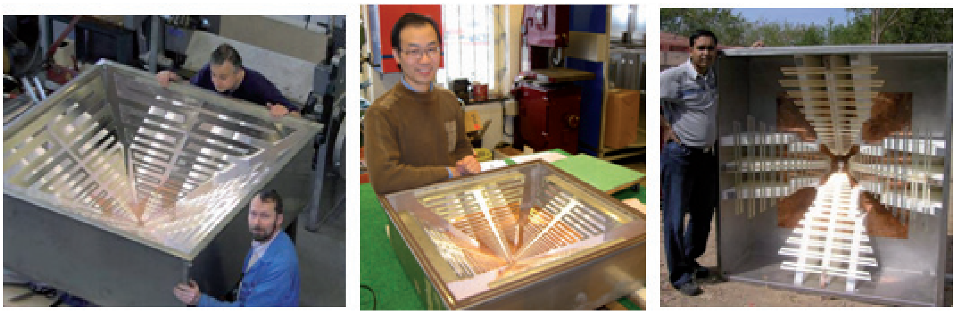

Figure 6.12: Three previous all-metal Eleven feed models developed for use in Green Bank radio telescope for 150 - 1700 MHz (left), in RATAN telescope for 500 - 3000 MHz (middle), and in Giant Meter Radio Telescope for 200 - 800 MHz (right).

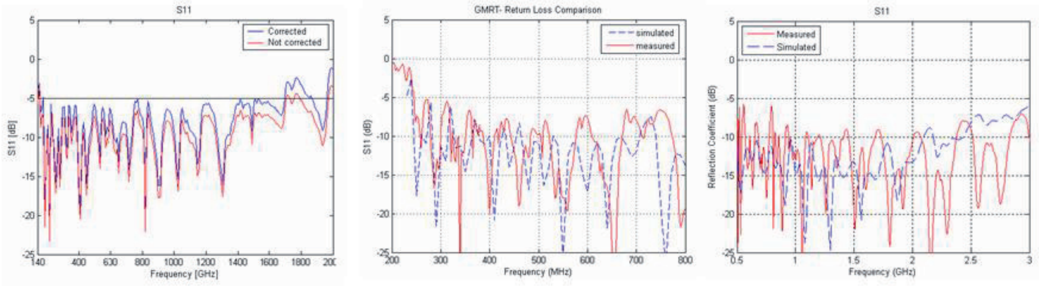

Figure 6.13: Simulated and measured reflection coefficients of Eleven feed for Green Bank, GMRT and RATAN radio telescopes, from left to right, respectively [5] [6].

This section reviews the performance of several previous all-metal Eleven feeds designed, manufactured and and measured at frequencies below 3 GHz for radio telescopes such as Green Bank (USA), GMRT (India) and RATAN (Russia) in Figure 6.12. The model for the 42 m diameter radio telescope in Green Bank [67] was designed to operate between 150 MHz and 1.5 GHz, the model for the Giant Meter Radio Telescope (GMRT) between

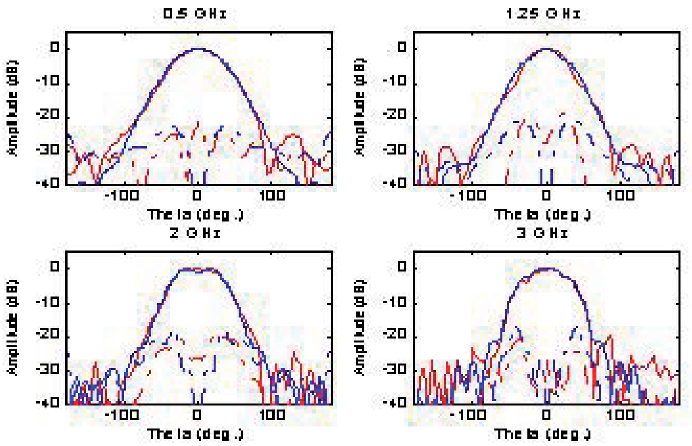

Figure 6.14: Measured and simulated radiation patterns in 45 degree plane of Eleven feed for RATAN telescope at selected frequencies. Red lines are measured. Blue are simulated. Solid lines are co-polar patterns. Dashed lines are cross-polar patterns [6].

200 and 800 MHz, and the model for the RATAN radio telescope between 500 MHz and 3 GHz.

One critical feature of a feed for a reflector used in radio telescope is the impedance mismatch factor, because a strong reflection at the antenna input port will increase the system noise temperature. The input reflection coefficient S_{11} was improved as shown in Figure 6.13. Since the antennas have balanced feeding, the measurements are done on the port of a 180° hybrid and the losses in the hybrid have been removed by appropriate calibration.

The above Eleven antenna models were designed by numerical simulation using WIPL-D based on the Method of Moment (MoM). The discrepancies between simulated and measured S_{11} are mainly due to the difficulties in accurately including the central puck (feeding region) in the simulations. The measured radiation patterns are in very good agreement with the simulations, as can be seen from Figure 6.14. The radiation efficiency due to losses in materials are shown in Figure 6.15. The results have been measured in a reverberation chamber with an accuracy of about 0.5 dB RMS, as described in [68].

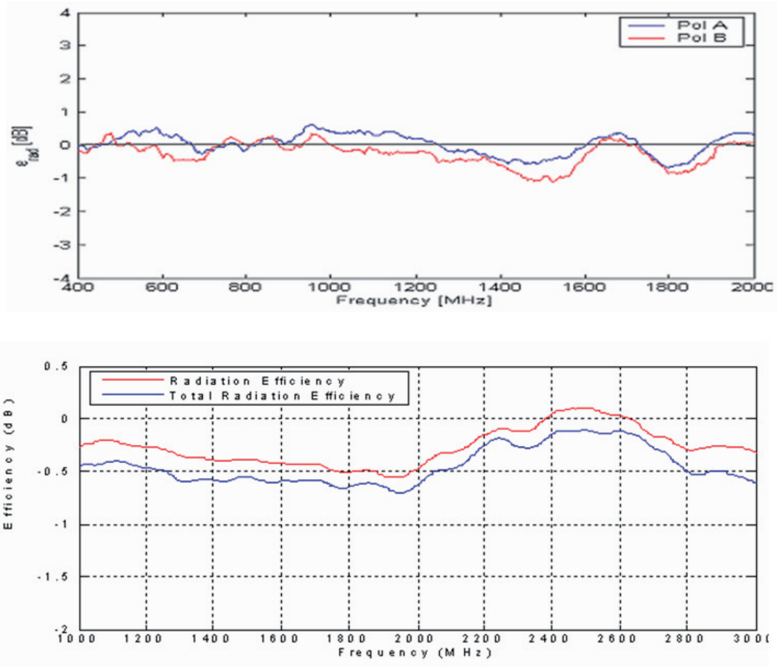

Figure 6.15: Measured radiation efficiencies of Green Bank (top) and RATAN (bottom) models by using reverberation chamber. Note that some efficiencies being larger than 0 dB is due to the 0.5 dB RMS accuracy of the reverberation chamber [6].

6.3 Review of a Decade Wide Band Model 1-10 GHz

Researches on more than octaves bandwidth antennas have gained a lot of attention [36] [69] [70], since wideband antenna systems are required for many new and future applications, such as in radio astronomy and ultrawideband (UWB) communication technology [71], [72]. The ongoing radio astronomy applications mainly include the SKA and the VLBI2010 project, both of which have reflector antennas as candidates covering 1-13 GHz or even higher. In contrast, the UWB systems require small direct radiating antennas covering typically 3.1-10.7 GHz. Thus, the frequency ranges are similar, although the requirements are quite different.

This section introduces a linearly polarized Eleven feed for radio astronomy operation between 1 and 10 GHz [2]. The large bandwidth is obtained through cascading folded dipoles one after another with log-periodic scaling factor *k* within each petal. The first folded dipole pairs are approximately halfwave dipoles at a frequency which is referred to as the highest geometrical frequency $f_{geo-max}$. The second dipole pair has a geometrical frequency $f_{geo-max}/k$, and the rest can be done on the analogy of this; the last folded

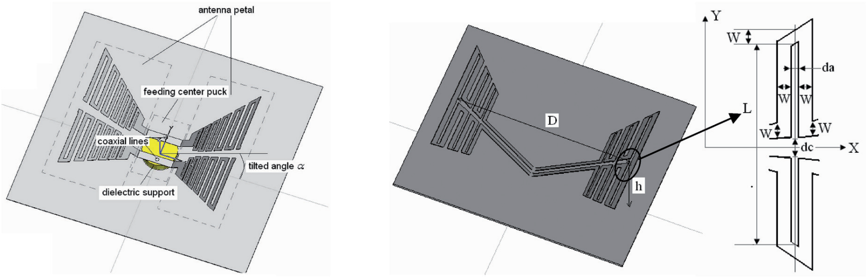

Figure 6.16: Configuration of Eleven feed of single polarization and parameters describing the geometry of the two petals [2].

dipole pair has the geometrical frequency $f_{geo-max}/k^{N-1}$, where *N* denotes the number of folded dipole pairs used in the array. By using geometrical frequency f_{geo} for each folded dipole pair, the parameters describing the geometry can be expressed in terms of the geometrical wavelength $\lambda_{geo} = c/f_{geo}$ (*c* is the speed of light in free space). The outermost folded dipole of each petal is short-circuited at its outer port for mechanical as well as thermal conduction reasons. Usually, the operating bandwidth is somewhat narrower than the geometrical bandwidth $[f_{geo-max}, f_{geo-max}/k^{N-1}]$, because it is according to our experience impossible to match the outermost and innermost dipoles to the same performance as those in the middle.

The antenna petal is modeled in WIPL-D as an infinitely thin copper sheet $without$ any dielectric support. As shown in Figure 6.16, the geometry is specified by the following parameters:

1. the scaling factor *k*
2. the length of the folded dipole *L*
3. the center gap of folded dipole *dc*
4. the strip width in arm of folded dipole *w*
5. the strip spacing in arm *da*
6. the spacing between folded dipole pairs *D*
7. the height of folded dipole over the ground plane *h*

All parameters except *D* and *h* are optimized in this work. *D* is fixed to $0.5\lambda_{geo}$ in order to obtain low cross polar level of radiation performance, and *h* was not included in the optimization due to mechanical constraints. The transmission line connecting two neighboring folded dipoles within each petal is varying log-periodically as well.

The very wide frequency band makes the size of the whole antenna very large in terms of the minimum wavelength, which results in very large computation time. In order to reduce the optimization time, a simple 1-by-1 parameter optimization scheme is adopted corresponding to optimizing each dimension as if it is independent of the others. Even though this scheme may not result in a global optimum solution, it is feasible under the restriction of computational resources.

The above-mentioned 1-by-1 optimization scheme can be described as follows:

1) Starting point based on previous Eleven feed;
2) Loops over different values of the log-periodic parameters, one by one, and in the order of *k*, *L*, *w*, *da*, *dc*;
3) Finally, optimize the same parameters of each of the three innermost folded dipoles individually.

The complete optimization procedure was repeated 3 times. The final optimized result is shown in Table 6.2.

Table 6.2: Results of one-by-one parameter optimization scheme [2]

Predefined parameters	**Value**
Number of dipole pairs *N*	21
Highest geometrical frequency $f_{geo-max}$	18.2 GHz
Spacing between two parallel dipoles *D*	0.50 λ_{geo}
The height of dipole over ground *h*	0.15 λ_{geo}
Optimized log-periodic parameters	**Value**
Scaling factor *k*	1.18
Length of dipole *L*	0.41 λ_{geo}
Arm spacing in folded dipole *da*	0.01 λ_{geo}
Width of dipole *w*	0.012 λ_{geo}
Center gap of folded dipole *dc*	0.03 λ_{geo}

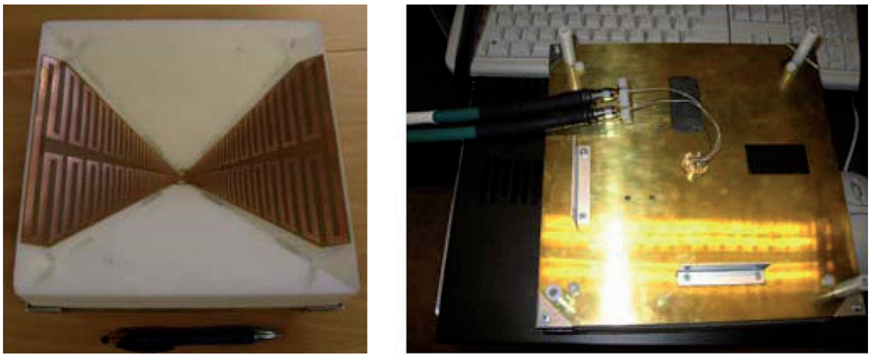

Figure 6.17: Eleven feed for 1-10 GHz (21-pair dipoles) and the measurement set-up for reflection coefficient [2].

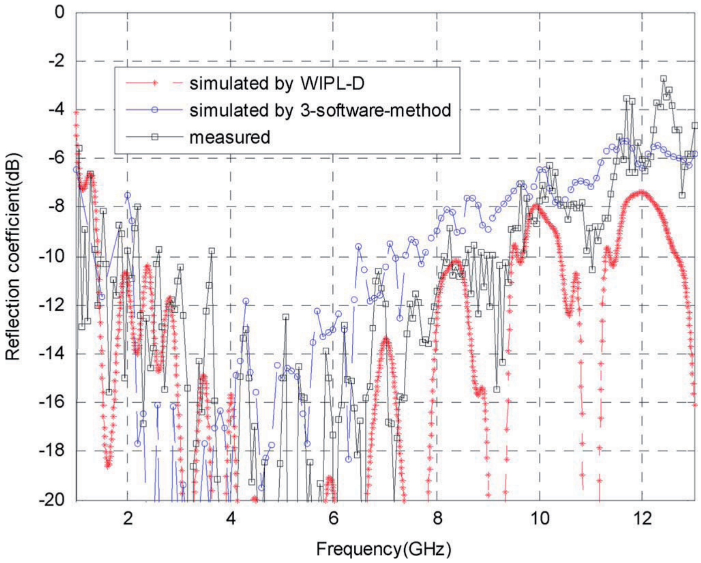

Figure 6.18: Measured and simulated reflection coefficient [2].

Figure 6.17 exhibits the Eleven feed made of metal strips on a thin Kevlar sheet and supported by foam. However, in order to perform time-efficient simulations by the moment method with as few basis functions as possible, the geometry is approximated by removing the dielectric parts; their effect on radiation pattern and input reflection coefficient is negligible, because the dielectric film is very thin and the permittivity of the foam very close to unity. The number of unknowns is dramatically reduced by this approximation. However, the dielectric parts of the center puck must be included, and this is better performed by using CST MWS due to the fine geometrical details in there. So a 3-software method is thus used to improve the analysis after the optimization. WIPL-D is used to model the antenna petals without the Kevlar film, while CST MWS is used to simulate the center puck of the Eleven antenna with the Kevlar film and dielectric support. After full-wave simulations of these two parts, their scattering parameters are extracted and exported into Advanced Design System (ADS) , where the return loss of the whole Eleven feed is calculated.

Figure 6.18 shows the measured and simulated reflection coefficients. It can be observed that the reflection coefficient can be predicted better by using 3-software method than by using only WIPL-D, which did not include the thin Kevlar film and the dielectric support at the center, especially at frequencies above 10 GHz. This is very important to know for further development to higher frequency bands. It can also be concluded that the effect of the thin Kevlar film under the radiating dipoles is negligible, whereas the dielectric support in the center puck is not. The reflection coefficient is below -8 dB over 1-10 GHz,

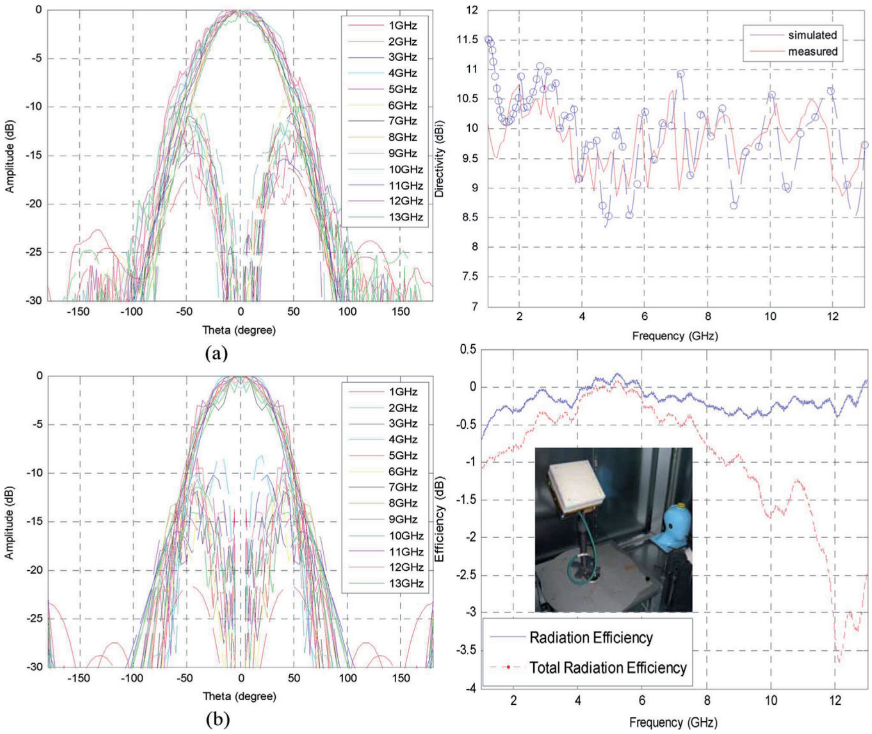

(a)

(b)

Figure 6.19: Measured (a) and simulated (b) radiation patterns in ϕ=45° plane. Solid line-copolar, dash line-crosspolar. Measured and simulated directivity (upper right). Radiation efficiency measured in Bluetest's reverberation chamber (bottom right) [2].

which is better than that of a previous model (-6 dB over 1-6 GHz) in [35].

Figure 6.19 presents the measured (upper left) and simulated (bottom left) co- and cross-polar radiation patterns in ϕ=45° plane from 1-13 GHz. It can be observed that the agreement between the measured and the simulated patterns is reasonable, and the beam shape is almost the same over the whole frequency band. Figure 6.19 (upper right) shows the measured and simulated directivities of the feed over the band, and the difference between them is within 1 dB over the most frequency points. The measured directivities were obtained by integration of measured 3D radiation patterns for angle θ from 0 to 180 degrees and angle ϕ from 0 to 360 degrees, both with intervals of 1 degree. The measurement over the frequency range of 1-8 GHz was done at the Technical University of Denmark (DTU) , and over the frequency range of 8-13 GHz at Chalmers, both with intervals of 0.1 GHz. The simulated results were obtained by using WIPL-D at 61 frequency points over 1-13 GHz with logarithmic interval scale and then using the Spline function in Matlab. Radiation efficiency e_{rad} is a measure of the dissipation losses in the antenna itself. Total radiation efficiency is defined as $e_{totrad} = e_{mismatch} \cdot e_{rad}$, where $e_{mismatch} = 1 - |r|^2$ is the mismatch factor with r the input reflection coefficient. Figure 6.19 (bottom right) shows the measured radiation efficiency by using Bluetest's time-efficient reverberation chamber [68]. The accuracy is ± 0.5 dB, which explains the positive values of the efficiency around 5 GHz. It can be concluded that the radiation efficiency is about -0.25 dB on average and the total radiation efficiency is quite low at high frequencies due to the mismatch loss.

6.4 Review of an Ultra Wide Band Model Above 10 GHz

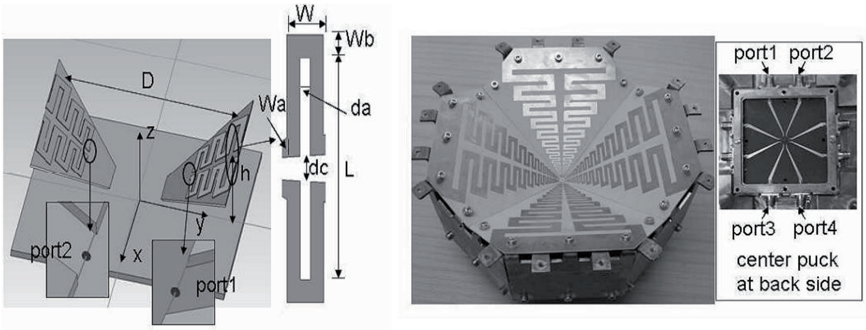

Figure 6.20: Modeling in CST and hardware of the dually polarized Eleven feed for 2-13 GHz (14-pair dipoles). The octagon of metal dewar has a circumradius of 200 mm [7].

This section introduces a dually polarized Eleven feed at 2-13 GHz including 14 pairs of folded dipoles, which has been optimized by using the Genetic Algorithm. As shown in Figure 6.20, the geometry of the Eleven feed is determined by the following parameters:

1. the spacing D between folded dipole pairs
2. the length L of the folded dipole
3. the height h of folded dipole over the ground plane
4. the center gap dc

5-7. the folded dipole widths w, wa and wb

8. the arm spacing da
9. the scaling factor k

All parameters are in term of geometrical wavelength λ_{geo} and varying log-periodically except that the thickness of the copper strips (t_{metal}) and the dielectric layer (t_{die}) is fixed as t_{metal} = 0.070 mm and t_{die} = 0.380 mm, respectively. The optimization goal of the work is to minimize the reflection coefficient of the Eleven feed over 2-13 GHz under condition of keeping good radiation characteristics of the feed and that the feed should be

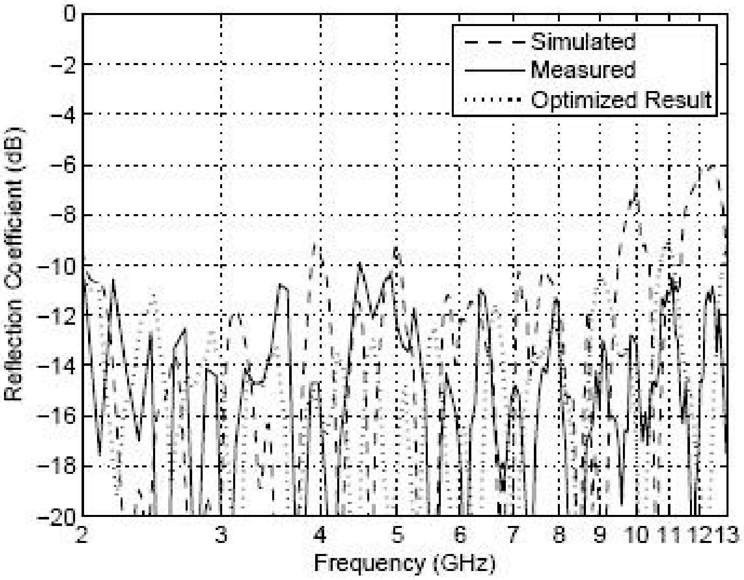

Figure 6.21: Simulated (dash) and measured (solid) reflection coefficient of the dually polarized Eleven feed, and the final result (dot) of optimized linearly polarized Eleven feed [7].

cryogenically coolable. Therefore, the spacing *D* between the folded dipole pair is fixed as $0.5\lambda_{geo}$ and antenna petals are manufactured on a printed circuit board with substrate of Rogers TMM3 (ϵ_r = 3.27 and tanδ= 0.002 at 10 GHz) which has the same thermal expansion factor as copper.

Genetic Algorithm is used together with WIPL-D and the chromosomes expressed by floating point vectors can be shown as

$chromosome = \{k, L, w, w_a, w_b, d_c, d_a, h\};$

The first generation was created randomly with a population of 50 individuals. Then, an elite group of 10 individuals with the best chromosome was selected and two-point crossover is applied among the group for creating chromosomes for next generation. For the remaining non-elite population, roulette-wheel selection is used to choose the chromosomes, and crossover is used to create the chromosomes for the rest population for the next generation. All chromosomes are checked for the possibility of giving manufacturable hardware. If the population of the next generation is fewer than 50 due to the mechanical constraints, mutation and random creation are used to create more chromosomes. The whole procedure runs 5 generations to achieve convergence. The most favorable result is as follows:

chromosome = {*1.19, 0.176, 0.0365, 0.0229, 0.015, 0.025, 0.0107, 0.172*};

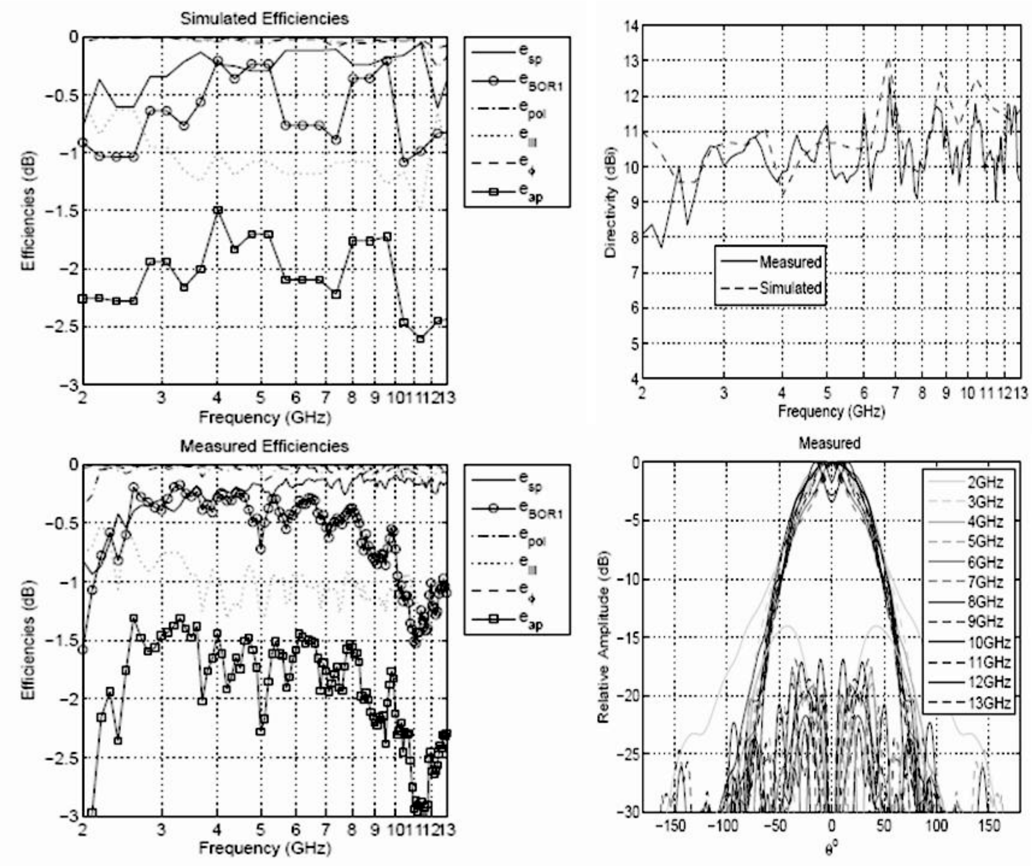

Figure 6.22: Simulated and measured efficiencies of the dually polarized Eleven feed (left); simulated and measured directivity of the dually polarized Eleven feed (upper right); measured radiation pattern of BOR1 component (bottom right) [7].

After the linear polarization configuration has been optimized, the dually polarized Eleven feed is obtained by simply adding two more identical 90° rotationally symmetric petals. A center puck illustrated in Figure 6.20 is designed and optimized in order to feed the antenna petals. Each polarization is excited by 4 ports, as ports 1-4 shown in Figure 6.20. Ports 1-4 have 50 Ω impedance and they are excited with the same amplitude and phase of 0°, 180°, 0° and 180°, respectively. The center puck transfers the 50 Ω port impedance to a differential (i.e. balanced feeding) 200 Ω impedance on each dipole petal. It can be observed from Figure 6.21 that the measured reflection coefficient of the dually polarized feed is below -10 dB over 2-13 GHz. This is an improvement compared with the one in the previous section by 2 dB below 10 GHz and 7 dB over the frequency range of 10 to 13 GHz. For the radiation performance, Figure 6.22 (left) shows the simulated and measured subefficiencies as well as the total aperture efficiency of the dually polarized feed when feeding a large paraboloid with semi subtended angle of 60° (the corresponding F/D = 0.433). As can be observed, the BOR1 efficiency e_{BOR1} is higher than -1 dB for 2.5-10 GHz and higher than -1.5 dB for 10-13 GHz, the polarization sidelobe efficiency e_{pol} > -0.2 dB, the phase efficiency e_{ϕ} > -0.1 dB, and the total aperture efficiency is better than -3 dB for 2-13 GHz. Figure 6.22 (upper right) shows the simulated and measured directivity of 2-13 GHz and Figure 6.22 (bottom right) shows the co- and cross-polar radiation patterns of the BOR1 components in ϕ=45° plane, where we can find that the beamwidth is nearly constant over the whole band.

6.5 Circular Eleven Feed

One important measure of the performance of the wideband feeds is the so-called BOR1 efficiency [38] [73] which characterizes how rotationally symmetric the radiation field function is. In order to improve the BOR1 efficiency for the Eleven feed, it is natural to make circularly curved folded dipoles, since until now all ultra-wideband or decade bandwidth feeds for reflector antennas are non-rotationally symmetrical. It was reported in [1] that a flat circular single-folded dipole pair Eleven antenna had an improved BOR1 efficiency, compared to the straight folded dipole pair one. In this section, we propose a new circularly curved wideband Eleven feed, where the four petals of the circular folded dipole array are made in four pieces of flat printed circuit boards (PCB) in the same way as the models described in [74] [75].

The first work was carried out on an 8-pair-dipole model as a preliminary investigation so that the simulation time by using CST could be reasonably acceptable and an optimization procedure could be performed. Wider frequency bands can be obtained by extending the geometry presented here by cascading more logarithmically scaled circularly curved folded dipoles.

The geometry of the new circular Eleven feed can be described with help from the modeling in CST. Due to the symmetry, we only need to model half of one petal of the circular Eleven antenna. Thereafter, the complete four petals can readily be constructed by mirroring with respect to the symmetrical planes. As illustrated in Figure 6.23, a metal disc is built as a ground in the XY-plane, which center coincides with the center of the rectangular coordinate system. Then, a large triangular plate is added above the ground disc with an angle (ang_0) from the ground plane; ang_0 is chosen such that the spacing between the paired dipoles on the two antenna petals is roughly half wavelength. This plate models a printed-circuit board (TMM3 material from Rogers), which consists of two layers - a metal layer of 0.070 mm thickness and a dielectric layer of 0.381 mm thickness. The apex of the dielectric layer coincides with the center of the ground disc. Afterwards, the circularly curved folded dipole strips is formed by a series of auxiliary cylinders.

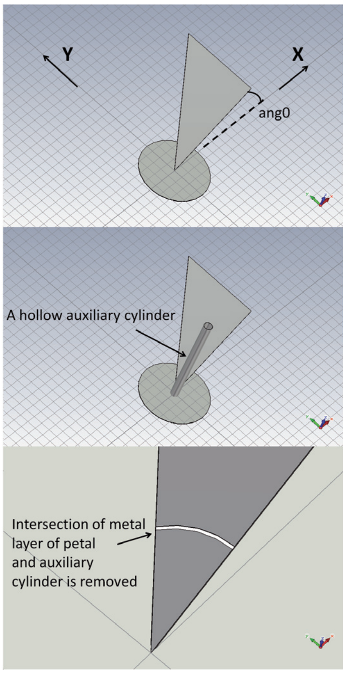
Y
X
ang0
A hollow auxiliary cylinder
Intersection of metal layer of petal and auxiliary cylinder is removed

Figure 6.23: Flat petal plate above ground disc with angle $ang0$ from the ground plane (top); example of auxiliary circular cylinder used to find the circularly curved shape of the folded dipoles on the petal. The shape appears circular when seen from above (middle, bottom).

An auxiliary cylinder is parametrically designed to intersect the tilted metal layer, and the intersection as well as the cylinder itself will be removed afterwards. Presented in Figure 6.23 (middle, bottom) is an example of how an auxiliary cylinder is used to obtain a curved shape which is circular when seen from above. In this way, it is feasible to determine the circularly curved printed dipole shapes on each of the PCB boards forming the four petals. As shown in Figure 6.24 (top), r_0, w_0 and s_0 are, respectively, measures of the XY-plane projections of the radius of curvature, strip width and arm width of the first folded dipole. It implies that auxiliary cylinders can be applied to conveniently shape the curved printed dipole arms. For instance, an auxiliary cylinder with an inner radius (r_0+w_0) and an outer radius (r_0+s_0-w_0) can be used to produce the curved arm gap between the strips of the first folded dipole. Similarly, the projected radius, arm width and strip width of the second

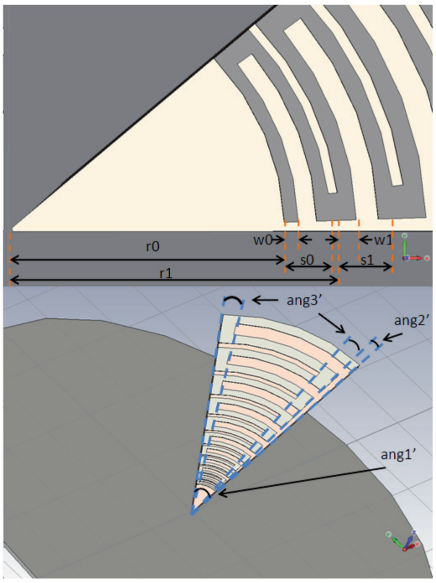

Figure 6.24: Dimensions that define the antenna structure (the denoted lengths are projected lengths in the XY-plane; ang_1, ang_2 and ang_3 are the projected angles in the XY-plane of the denoted angles ang1′, ang2′ and ang3′, respectively).

folded dipole is r_1, w_1 and s_1, respectively; moreover, these subsequent dimensions can be derived by scaling the initial dimensions with a scale factor k:

$$\begin{aligned} r_1 &= r_0 \cdot k \\ s_1 &= s_0 \cdot k \\ w_1 &= w_0 \cdot k \end{aligned} \tag{6.1}$$

In a log-periodic fashion, the projected radius, arm width and strip width of the n^{th} ($n > 1$) folded dipole in an array can be expressed as follows:

$$\begin{aligned} r_n &= r_0 \cdot k^{(n-1)} \\ s_n &= s_0 \cdot k^{(n-1)} \\ w_n &= w_0 \cdot k^{(n-1)} \end{aligned} \tag{6.2}$$

So a series of auxiliary cylinders extended in such a log-periodic fashion can make it quite easy to lathe the metal layer to form circular dipole strips. In addition, the angles ang_2 and ang_3 denoted in Figure 6.24 (bottom) are actually projected angles between the XY-plane projections of the corresponding dashed lines. This is to make it convenient, similar to the previous depiction of ang_1, to shape the petal by using flat surfaces.

Table 6.3: Dimensions that define the circular Eleven antenna

Dimensions	Value
r_0	$0.3000 \cdot \lambda_{geo-min}$
s_0	$0.0500 \cdot \lambda_{geo-min}$
w_0	$0.0150 \cdot \lambda_{geo-min}$
k	1.2000
ang_0	33.0°
ang_1	42.0°
ang_2	2.00°
ang_3	4.00°

The 8 dimensions that define the whole antenna structure are listed in Table 6.3. The first 3 length dimensions are in terms of $\lambda_{geo-min}$ (in this case, $\lambda_{geo-min}$ = 50 mm, corresponding to 6 GHz in free space), which is the geometrical minimum wavelength that is predefined as a design goal. Note that the geometrical minimum wavelength may be somewhat smaller than the operating minimum wavelength at which the simulation model can actually perform. This is because the relative dielectric constant (ϵ_r) of the printed-circuit board is not accounted for in $\lambda_{geo-min}$.

Presented in Figure 6.25 are different views of the complete simulation models of the circular 8-pair-dipole Eleven Feed with dual linear polarizations. A discrete port is placed across the feed gap of the innermost dipole strips on the petal in the X > 0 region. In order to simplify the calculation by CST, the XZ-plane is set as an electric symmetrical plane, whereas the YZ-plane is set as a magnetic symmetrical plane. The time-domain solver of CST (based on FDTD method) is used to simulate the 8-pair-dipole dually-polarized Eleven model as depicted in Figure 6.25.

Below present we the simulation results for the final circularly curved Eleven feed designed by using CST.

Presented in Figure 6.26 is the simulated reflection coefficient with reference to 300 Ω port impedance. As can been seen from the figure, the reflection coefficient is largely better than -8 dB between 1.6 and 3.7 GHz (about 2.3 : 1 bandwidth). We believe that it is possible to further improve the impedance match by using advanced optimization techniques in future work.

The BOR1 component of the far field function of a feed antenna is the most part the total radiation field that adds to the directivity in a rotationally symmetric reflector. The BOR1 efficiency measures how closely the total far field resembles a BOR1-type field with only first order $\sin$ and $\cos$ variations of the far field, and it quantifies how much power is lost due to the non-BOR1 components. Figure 6.27 shows the co- and cross-polar patterns in dBi of the simulated total far field and the extracted BOR1 component of the dually

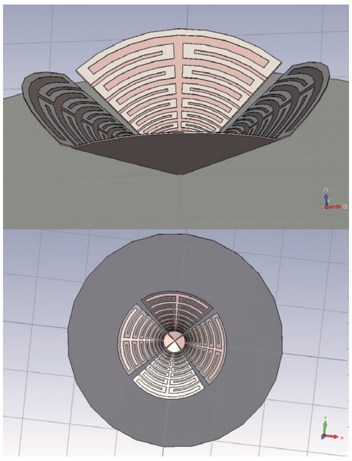

Figure 6.25: Different views of circularly curved 8-pair-dipole Eleven antenna with dual linear polarization.

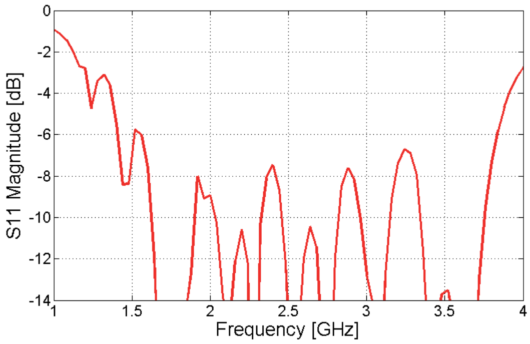

Figure 6.26: Simulated input reflection coefficient (with reference of 300 Ω port impedance) of the dually polarized circularly curved 8-pair-dipole Eleven antenna.

polarized Eleven feed. More precisely, the co-polar directivities and the relative cross-polar level of the BOR1 component are plotted at an interval of 0.1 GHz in Figure 6.28. It can be observed that the BOR1 co-polar directivities are approximately 10.5 dBi, and that the BOR1 relative cross-polar level is below -14 dB over 1.6-3.7 GHz.

Based on the extracted BOR1 component from the total far field of the Eleven feed, the aperture efficiency and several sub-efficiencies (i.e., illumination efficiency e_{ill}, phase efficiency e_{phs}, polarization efficiency e_{pol} and spillover efficiency e_{sp}) of a paraboloidal reflector (semi-subtended angle 60°) can be calculated by using formulas in Appendix A. In Figure 6.29, all the above-mentioned efficiencies are plotted at an interval of 0.2 GHz

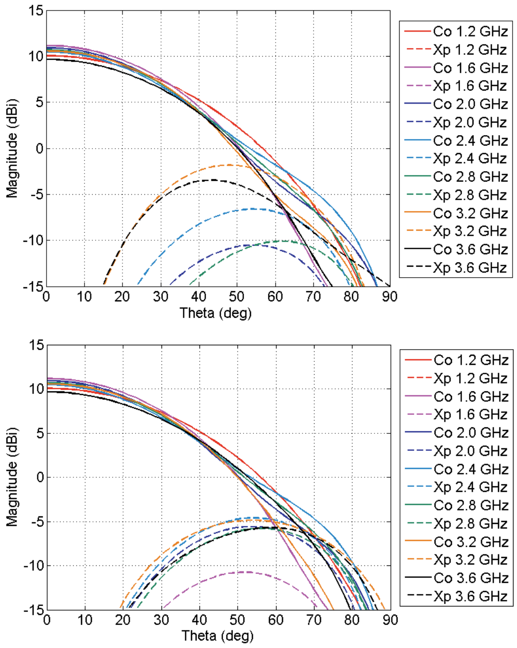

Figure 6.27: Co- and cross-polar radiation patterns (in $\phi = 45°$ plane, in dBi) of the simulated total far field (upper) and the extracted BOR1 component (lower) of the dually polarized circularly curved Eleven antenna (the ground plane is set as an infinite PEC plane in CST.

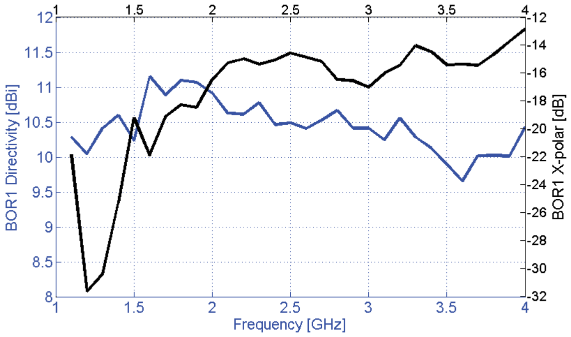

Figure 6.28: Simulated directivities and cross-polar level of the BOR1 patterns over the whole band. Plotted at an interval of 0.1 GHz.

over 1.2-3.8 GHz. We can readily find that the BOR1 efficiency varies around -0.25 dB while the aperture efficiency varies around -1.7 dB over the whole band. Compared with

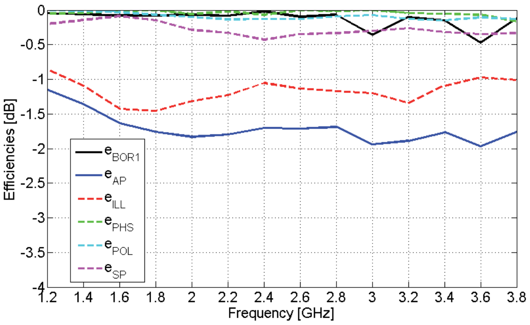

Figure 6.29: Calculated efficiencies when the dually polarized circularly curved Eleven antenna feeds a reflector with semi-subtended angle of 60°, based on the simulated far field by using CST. Plotted at an interval of 0.2 GHz.

the dually-polarized straight Eleven feed introduced in subsection 6.1.2 (recall Figure 6.11), the BOR1 efficiency of this circular Eleven feed is improved by 0.3∼0.4 dB; and therefore, the aperture efficiency is accordingly improved by around 0.3 dB. As a result, we believe that the circular version of the Eleven feed is quite promising to improve the BOR1 efficiency and therefore the aperture efficiency for use in the future wideband radio telescopes.

6.6 Summary of Chapter 6

The Eleven feed is a promising candidate for use in the next generation radio telescopes. A number of different designs of Eleven feed for reflector antennas are exhibited in this chapter. They operate over from triple up to decade frequency bandwidths for different application purposes. The merits of the Eleven feed include low profile, nearly constant beamwidth and constant phase center, etc., over up to a decade bandwidth. Until now, the Ku-band is the highest band the Eleven feed can reach up to, which is primarily due to the mechanical limitations on the innermost folded dipoles, some RF issues (e.g. surface waves) on the center puck, and so on.

A new concept of circular Eleven feed is also introduced in this chapter. Compared with the conventional Eleven feeds based on straight folded dipoles, the circular Eleven feed is rotationally symmetric and capable of improving the BOR1 efficiency and therefore the aperture efficiency by a fraction of dB, according to the simulation results as well as our practical experience on this respect.

Chapter 7

Multi-Port Eleven Antenna For Narrowband MIMO Applications

7.1 Background of Narrowband Radio Channel

In the study of radio channels, signals transmitted over narrowband channels invariably contain a set of frequencies within a bandwidth which is narrow compared with the center frequency of the channel. Narrowband implies that the channel under consideration is sufficiently narrow so that its frequency response (transfer function) can be considered flat, and the bandwidth of the signal does not significantly exceed the channel's coherence bandwidth, which will be introduced later.

Consider a complex baseband signal represented in the time domain by

$$u(t) = a(t)e^{j\theta(t)} \tag{7.1}$$

where $a(t)$ is the envelope and $\theta(t)$ is the phase of the baseband signal. The modulated signal with carrier frequency f_c is then

$$s(t) = Re[u(t)e^{j2\pi f_c t}] \tag{7.2}$$

At the input of the demodulator, the received signal at time *t* is then given by

$$z(t) = A\alpha(t)s(t) + n(t) \tag{7.3}$$

where *A* is the overall path loss due to the path loss in the normal sense and the shadowing (slow fading), and it is assumed not to vary with time (or vary very slowly at least); $\alpha(t)$ is the complex fading coefficient at time *t* due to fast fading; and $n(t)$ is the complex white noise. $n(t)$ consists of real and imaginary components, both of which are independant Gaussian processes with zero-mean and a standard deviation of σ_n. It can be proved that the mean noise power, i.e., $E[n(t)n^*(t)]$), equals σ_n^2.

7.1.1 AWGN Channel

If $\alpha(t)$ in (7.3) equals unity, it simply corresponds to an additive white Gaussian noise (AWGN) channel. When the signal is transmitted over such channels, the signal arriving at the demodulator is perturbed only by the addition of some noise and some fixed path loss. The rapid decrease in bit error rate (BER) as the signal-to-noise ratio (SNR) increases is characteristic of an AWGN channel.

7.1.2 Rayleigh Fading Channel

The performance of most mobile radio channels will not be so good as the pure AWGN channel, because the various detailed characteristics of the environment may result in fast fading due to several waves that arrive at the receiver via different routes, i.e. multipath propagation. If the direct wave from the transmitter to the receiver is present, the case is called the line-of-sight (LOS) propagation; otherwise, if the direct path is somehow blocked, the case is then called the non-line-of-sight (NLOS) propagation. In the NLOS case, each of the waves has a different phase that can be thought of as an independent uniform distribution.

Consider that the complex fading coefficient in (7.3) has its real and imaginary parts,

$$\alpha(t) = x(t) + jy(t) \tag{7.4}$$

and the variable α is now a complex Gaussian random variable (both x(t)- and y(t)-amplitude have Gaussian distribution), whose modulus is represented by a random variable *r*

$$r(t) = |\alpha(t)| = \sqrt{x^2(t) + y^2(t)} \tag{7.5}$$

The probability density function (PDF) of the variable *r* is given theoretically by the Rayleigh distribution function

$$f_r(r) = (r/\sigma^2)e^{-r^2/2\sigma^2} \tag{7.6}$$

where σ is the standard deviation of the real (or the imaginary) part of α, i.e., $E[x^2(t)] = E[y^2(t)] = \sigma^2$. Since the fading varies with time, the SNR at the input of the demodulator also varies with time. If the fading is assumed constant over the transmitted symbol duration, then the instantaneous SNR $\gamma(t)$ is constant over a symbol as well, and is given by

$$\gamma(t) = \frac{\text{Signal power}}{\text{Noise power}} = \frac{|A\alpha(t)s(t)|^2/2}{P_n(t)} = \frac{A^2r^2(t)}{2P_n(t)} \tag{7.7}$$

where $|s(t)|$ is assumed to equal unity, and $P_n(t)$ is the instantaneous noise power. The average SNR $\overline{\gamma}$ is thus the mean of $\gamma(t)$,

$$\overline{\gamma} = \frac{A^2 E[r^2(t)]}{2E[P_n(t)]} = \frac{A^2(E[x^2(t)] + E[y^2(t)])}{2\sigma_n^2} = \frac{A^2\sigma^2}{\sigma_n^2} \tag{7.8}$$

From (7.7) we have,

$$r^2(t) = \frac{2P_n\gamma(t)}{A^2} \quad \text{and} \quad \frac{dr(t)}{d\gamma(t)} = \sqrt{\frac{P_n}{2A^2\gamma(t)}} \tag{7.9}$$

By using the identity and combining (7.6) (7.8) and (7.9), we can find the PDF of γ given the PDF of *r*,

$$f_\gamma(\gamma) = f_r(r)|\frac{dr}{d\gamma}| = \begin{cases} \frac{1}{\overline{\gamma}} e^{-\gamma/\overline{\gamma}} & \gamma > 0; \\ 0 & \text{otherwise} \end{cases} \tag{7.10}$$

and for the cumulative distribution function (CDF) , we obtain

$$P_\gamma(\gamma < \gamma_s) = 1 - e^{-\gamma_s/\overline{\gamma}} \tag{7.11}$$

7.1.3 Rician Fading Channel

The received signal in the LOS case consists of a random multipath component and a line-of-sight component that has essentially constant power. This power will be usually greater than the multipath power before it significantly affects the Rayleigh distribution. The theoretical distribution applied for this case is the Rice distribution,

$$f_r(r) = \frac{r}{\sigma^2} e^{-(r^2+s^2)/2\sigma^2} I_0(\frac{rs}{\sigma^2}) \tag{7.12}$$

where σ^2 is the variance of either the real or the imaginary part of the multipath component alone, *s* is the magnitude of the LOS component, and I_0 is the modified Bessel function of the first kind and zeroth order. The PDF of the Rice distribution is often expressed in terms of *k*, which is usually known as the Rice factor and defined as

$$k = \frac{\text{Power in constant part}}{\text{Power in random part}} = \frac{s^2}{2\sigma^2} \tag{7.13}$$

Then (7.12) can be rewritten as follows:

$$f_r(r) = \frac{r}{\sigma^2} e^{-r^2/2\sigma^2} e^{-k} I_0(\frac{r\sqrt{2k}}{\sigma}) \tag{7.14}$$

The larger *k* is, the more deterministic is the channel. As the *k* factor increases, the probability of encountering a deep fade reduces, resulting in lower mean error rate. Two special cases occur when *k* equals zero and infinity, respectively. The former case is simplified to the Rayleigh channel and the latter case reverts to the AWGN channel, which in some senses are the "worst-case" and "best-case" mobile radio channels, respectively.

In the study of the multipath fading, by the way, there is a very important concept called the coherence bandwidth, B_c (rad/second). It is a statistical measurement of the range of frequencies over which the channel can be considered flat. The coherence bandwidth can be approximated as inversely proportional to the multipath time delay spread (the time difference between the arrival moment of the first multipath component and the last one). In order to make the impairment of signal due to the multipath fading as small as possible, the signal bandwidth must not significantly exceed the coherence bandwidth of the channel.

7.1.4 Doppler Effect

The Doppler effect can be understood with the help of the properties of Fourier transform, one of which states that if a complex signal is multiplied by a positive or negative phase term in the time domain, then its corresponding signal in the frequency domain will be shifted downwards or upwards in frequency. The Doppler effect typically takes place in the situation where there is relative motion between the receiver and the source of the signal. If the receiver moves towards the source, the apparent frequency of the arriving wave, as observed by the receiver, is increased, whereas the apparent frequency of the arriving wave decreases for motion away from the source. The change in the apparent frequency, i.e. the Doppler shift f_d, is given by the rate at which the receiver crosses wavefronts of the arriving wave (the source is assumed stationary),

$$f_d = f_c \frac{v}{c} \cos \alpha \tag{7.15}$$

where f_c is the carrier frequency, *v* is the speed of the receiver, *c* is the speed of the light in free space, and α is the angle between the direction of motion and the direction of the incoming signal. Especially when α=0, we get the maximum Doppler shift $f_{dm} = f_c v/c$. In general, the Doppler shift associated with an incoming wave can have any apparent frequency in the range $[f_c - f_{dm},\ f_c + f_{dm}]$.

The Doppler effect also takes place when multipath propagation occurs, as each of the arriving waves with different directions has its own associated Doppler frequency, the bandwidth of the received signal is spread relative to its transmitted bandwidth. The shape of the resulting Doppler spectrum depends on the relative amplitudes and directions of each incoming wave. The Clarke's model [76] assumes that the arriving waves are equally likely to come from any horizontal directions, and it ends up with the classical U-shaped Doppler spectrum. However, this assumption of uniform Angle-of-Arrival (AoA) probability may not hold in the situations where propagation is dominated by the effect of some particular local scatters; so more accurate AoA assumptions need to be put forward for such specific situations. In addition, there exist as well models for 3-D cases, e.g. the Aulin's model [77], which have included the AoA probability in the vertical direction.

The Doppler effect can also be viewed in the time domain. The Wiener-Khinchin theorem tells us that for a stationary random process, the inverse Fourier transform of the power spectral density equals the autocorrelation function (ACF) of the signal inc the time domain. The ACF expresses the correlation between a signal at any a time and its value at some time delay τ. In the case of the classical spectrum with Rayleigh fading, the ACF turns out to be as follows [78]:

$$\rho(\tau) = J_0(2\pi f_{dm}\tau) \tag{7.16}$$

where J_0 is the Bessel function of the first kind and zeroth order. This leads to a definition of the coherence time T_c for a radio channel as the time over which the channel can be considered constant. T_c is inversely proportional to the Doppler spread of the channel, and the proportionality constant is determined by setting a threshold level (usually $\rho = 1/\sqrt{2}$) on the ACF given by (7.16). A useful approximation to T_c for the classical channel is [79]

$$T_c \approx \frac{9}{16\pi f_{dm}} \tag{7.17}$$

Signals whose symbol durations are less than the coherence time T_c of the channel can be received approximately undistorted by the Doppler effect.

7.2 Background of Diversity Technology

Diversity is an important technique to mitigate the degradation of the signal quality due to the multipath fading in a narrowband radio channel. Although the diversity technique does offer benefits in the wideband channel, more advanced techniques, depending on the modulation and multiple access scheme in use, are demanded to take full advantage of the frequency diversity potential of the wideband channel. These advanced techniques include linear/nonlinear/adaptive equaliser structures for TDMA and single-user systems, Rake receivers for CDMA systems and OFDM receivers for DAB/DVB, WLAN and WiMax, etc., which, however, are out of the scope of this chapter.

7.2.1 Diversity

The basic idea of diversity is that the receiver should have more than one version of the transmitted original signal. Every version is received through a statistically independent channel (or branch) and the outputs of all the channels are processed by a diversity combiner before routed to the demodulator. To obtain a high degree of improvement from a diversity system, two criteria need be noted in the first place [80]. First, the fading in the individual channels should have low cross-correlation. If the correlation is otherwise too high, then it will result in high chance that deep fades in all the branches occur simultaneously. Second, the mean power received from each branch should be nearly equal, since the signal in a weaker branch might not be useful even though it is less faded than the other channels. The diversity can be obtained via a number of methods, including spatial, temporal, frequency, pattern and polarization diversities [81].

Spatial diversity employs multiple antennas that are physically separated from one another. Assume two antennas, separated by a distance *d*, are surrounded by a large number of scatters constituting a Rayleigh scattering environment. The correlation between the received signals at antenna 1 and 2 is as follows [80],

$$\rho_{12}(d) = \int_0^{2\pi} f_\theta(\theta) e^{j\frac{2\pi}{\lambda} d \sin(\theta)} d\theta \tag{7.18}$$

where θ is treated as a continuous random variable that denotes the angle between the direction of a certain incident wave and the broadside direction of the two antenna (the normal to the line joining the two antennas), and $f_\theta(\theta)$ is the PDF of θ. It can be shown that a wider angular distribution will lead to a faster decrease in the correlation at a given antenna spacing. In other words, an environment with significant scatters widely spread around the antenna will produce good spatial diversity for modest antenna spacings.

The idea of temporal diversity is to transmit the same signal multiple times, where the repetition intervals are long enough to achieve sufficient decorrelation. There are mainly three methods to realize the temporal diversity [81]. *Repetition coding* is the simplest but bandwidth-inefficient. *Automatic repeat request*, including a feedback channel, requires multiple transmissions only when the first transmission occurs in a bad fading state. *Forward error correction coding with interleaving* is a more advance version of repetition coding, where the different symbols of a codeword are transmitted at different times, so that it can increase the probability that at least some of them are received with good quality, from which the original codeword can then be reconstructed.

Regarding frequency diversity, the same signal is transmitted at different frequencies and the separation between two frequency components should be larger than the coherence bandwidth of the channel in order to decrease the effects of fading. However, it is more common to spread the information over a large bandwidth than to simply repeat the same information at two different frequencies. Actually, the principle of frequency diversity is implicitly employed in some forms of equalizer for wideband channels.

As we know, different types of antennas have different radiation patterns. Furthermore, even identical antennas can as well have different patterns when they are mounted close to each other, because of the mutual coupling between the antenna elements. As a result, multiple co-located antennas with different radiation patterns "see" differently weighted multipath components. This is basically what pattern diversity means, and this sort of diversity is often used in conjunction with spatial diversity.

A linearly polarized signal propagating in a radio channel can be depolarized into two orthogonally polarized signals by reflection and diffraction effects in the propagation environment. As the fading of signals with different polarizations is statistically independent, receiving both polarized signals via a dual-polarized antenna and processing the signals separately can possibly provide diversity. When one tries to make use of polarization diversity in practice, however, it should be noted that the average received signal power in the co- and cross-polarization branches may differ significantly in some cases, which has been studied in [82] [83] [84]. One improvement in this regard is with a mixed scheme where antennas are both spatially separated and differently polarized [83] [85].

7.2.2 Combination Methods

After multiple diversity branches are created, we need to combine the outputs of the branches to produce a signal resistant to the multipath fading. There are typically four combination methods nowadays: *selection combining*, *switched combining*, *equal-gain combining* and *maximum ratio combining*.

In *selection combining*, the diversity combiner selects the branch that has the highest instantaneous SNR, i.e. $\max(\gamma_1, \gamma_2, ..., \gamma_N)$. Assume *N* independent Rayleigh channels having an equal mean SNR, $\overline{\gamma}$, the CDF of all the channels having an SNR less than a certain value γ_s is then the equivalent probability for a single channel (recall (7.11)) raised to the power *N*,

$$P_\gamma(\gamma_1, \gamma_2, ..., \gamma_N < \gamma_s) = (1 - e^{-\gamma_s/\overline{\gamma}})^N \tag{7.19}$$

This expression indicates that the probability of deep fading can be reduced by means of the increase of the number of independent diversity branches. A drawback of selection combining is that the combiner must monitor all *N* branches simultaneously, which requires *N* independent receivers. An alternative is to use just one receiver with *switched combining* to establish a so-called "switch and stay" combiner, where the receiver is only switched between branches when the SNR on the current branch is lower than a predefined threshold. It is very important that the predefined threshold must be estimated with good accuracy and the switching rate needs to be limited to avoid excessive switching transients. The performance of switched combining is worse than selection combining, in that unused branches may have higher SNR than the current operational branch.

The previous two combiners receive on only one branch at a given time, the signal power in the other channels is then wasted. One improvement by *equal-gain combining* is to apply a phase correction before adding the signals from all N branches to enhance the SNR at the combiner output. Each branch is multiplied by a complex phaser ($e^{-j\theta_1}$, $e^{-j\theta_2}$ ... $e^{-j\theta_N}$) to ensure that the resultant signals are all co-phased, so that the signals can be added coherently; in the meanwhile, the noises on each branch are independent and randomly phased, hence they add only incoherently. In equal-gain combining, it may occur that one or some of the branches have considerably lower SNR than the others, and this will thus lead to reduction in the overall SNR after combining. A more optimum strategy is *maximum-ratio combining*. It is similar to the equal-gain combining, but further allows different weighing on signal amplitude in all branches so that the SNR at the combiner output can be maximized.

For the case of two uncorrelated, equal mean power Rayleigh channels, a comparison of combining methods has been carried out in [80]. The results manifest that the performance of the four methods can be ranked in a descending order in terms of the diversity gain: maximum-ratio, equal-gain, selection and switched combining.

7.3 Background of Reverberation Chamber

An electromagnetic reverberation chamber is a mode-stirred environment for electromagnetic compatibility (EMC) testing and other electromagnetic applications. The idea of reverberating an electrically large metal chamber by means of one or more rotating conductive stirrers to generate an average uniformly homogeneous and isotropic field was first reported by Mendes in 1968 [86]. And the statistical theories of reverberation chambers have also been studied in depth in [87] [88] [89] [90], etc. Comparable to a microwave oven, a reverberation chamber is a shielded cavity with a minimum of absorption of electromagnetic energy (high Q factor), in which very high field strength can be achieved with moderate input power. The reverberation chambers have for decades been an important and powerful tool for both electromagnetic immunity and radiated emission tests. During recent years, however, the reverberation chambers have increasingly been used to test small antennas and active MIMO (multiple-input multiple-output) terminal devices [68] [91] [92] [93], since the market of wireless communication terminals is stunningly booming over the years.

In real outdoor multipath environments, the arriving waves on a mobile terminal will have certain AoA distributions in both the elevation and azimuth planes. It is natural to assume that there is a uniform distribution in the azimuth plane and a non-uniform (e.g. Gaussian) distribution in the elevation plane (larger probability of waves coming in from close-to-horizontal directions). Besides, since most mobile base stations' signals are vertically polarized, the outdoor environments normally have a larger content of vertical polarization than horizontal, or in other words, a polarization imbalance, which can be characterized by cross-polar power discrimination (XPD: defined as the ratio between the co-polar power and the cross-polar power). Because both the AoA distribution and XPD can become different in different real environments, the measurement results of a terminal in one specific environment can not be directly transferred to another. It is thus convenient to define a reference environment, which can easily be reproduced in practice and which gives repeatable measurement results of the terminal's performance. The isotropic environment with polarization balance and a uniform AoA distribution over the whole sphere has this characteristic. This simplifies the characterization of antennas and terminals in the sense that the performance becomes independent of the orientation of the antenna in the real environments.

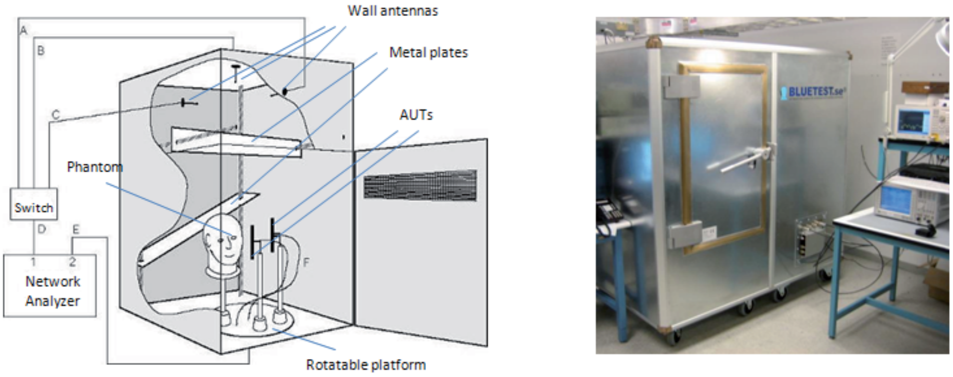

Figure 7.1: Drawing (left) and photo (right) of the Bluetest reverberation chamber. Its measurement accuracy is 0.5 dB standard deviation.

The Bluetest^{TM} rectangular reverberation chamber, as shown in Figure 7.1, is capable of emulating such an isotropic environment through the following four types of mode-stirring methods [94]:

1. Mechanical stirring: This is achieved by means of two plate-shaped mechanical stirrers that can be driven by step motors to move along a complete wall and along the ceiling.
2. Platform stirring: The antenna under test (AUT) is placed on a rotatable platform that moves the antenna to different positions inside the chamber.
3. Polarization stirring: There are three orthogonal wall-mounted chamber antennas, and

the transmission (S_{12}) is successively measured between each one of them and the AUT. The chamber can thus obtain a good polarization balance.
4. Frequency stirring: This corresponds to averaging $|S_{12}|^2$ over a frequency window (typically 10$\sim$25 MHz) during the postprocessing of the measurement results. The head phantom containing absorptive liquid loads the chamber and increases the average mode bandwidth. The chamber Q factor is thus reduced. The reduction in Q is also related to other losses due to leakage, non-ideal metal walls and reference antennas, etc. However, those contributions are generally minor when compared with the head phantom.

It can be argued that the reflection coefficient (S_{22}) of the AUT inside a reverberation chamber consists of two contributions: one (S_{22}^d) is deterministic and from the antenna itself as if it is located in free space, and the other (S_{22}^r) is statistical as a result of the stirring in the chamber. If the number of the independent samples of the random variable S_{22}^r is large enough, it must have a complex Gaussian distribution with zero mean. So it is possible to determine S_{22}^d by complex averaging the measured S_{22} over all stirred positions, and if necessary by additional frequency stirring [95].

Similarly, the transmission S_{12} (between one of the wall-mounted antennas and the AUT) must as well consist of two parts: a deterministic contribution in free space (S_{12}^d) and a statistical contribution due to the chamber (S_{12}^r). Because an isotropic environment with Rayleigh fading is desired in the reverberation chamber, the direct coupling term, S_{12}^d, should be as low as possible. Therefore, the main lobes of the wall-mounted antennas and AUT must not point towards each other; and it is preferred that each wall antenna has a null in the direction of the AUT. Besides, the platform stirring is very effective to reduce the direct coupling, since the AUT changes its direction at different stir positions. However, some researchers also take advantage of the direct coupling, together with loading the chamber, to achieve a controllable Rician environment for certain test purposes [96]. The transmission between two antennas in free space follows the well-known Friis transmission formula. Correspondingly, Hill's transmission formula is the one in the reverberation chamber, which is valid when there are a sufficiently large number of excited modes and no any direct coupling in the chamber [87]. Hill's formula can be referred to as the chamber transfer function and is presented as follows,

$$G_{chamber} = \frac{P_r}{P_t} = \frac{c^3 e_{rad1} e_{rad2}}{16\pi^2 V f^2 \Delta f} \tag{7.20}$$

where *c* is the speed of light in free space, e_{rad1} and e_{rad2} are the radiation efficiencies including mismatch of the two antennas, *V* is the chamber volume, *f* is the operating frequency and Δf is the average mode bandwidth. In particular, Δf, which is in connection with the chamber Q factor by $Q = f/\Delta f$, consists of four additive contributions due to wall losses, chamber aperture leakage, antennas and absorptive objects in the chamber, and the formulas of each contribution can be found in [87]. When measuring active terminals it is important that Δf be larger than the modulation bandwidth of the communication channel, otherwise measurement error can unexpectedly appear [94]. It has been found that if the free space mismatch efficiencies are removed from the transmission, the result is an average chamber transfer function that varies slower with frequency. As explained previously, the free space input reflection coefficients of the two antennas can be obtained by complex averaging the measured S_{11} and S_{22} in the chamber. Therefore, we can in the following way evaluate the chamber transfer function based on the measurement results [97],

$$G'_{chamber} = \frac{1}{N} \sum_{N} \frac{|S_{12}|^2}{(1 - |\overline{S_{11}}|^2)(1 - |\overline{S_{22}}|^2)} \tag{7.21}$$

where N is the number of the wall antennas; $\overline{S_{11}}$, $\overline{S_{22}}$ are the complex mean of S_{11} and S_{22}, respectively, which are averaged over all stirrer and platform positions as well as over a specified frequency window.

It has been derived in [90] that the normalized accuracy of E-field (Rayleigh distribution presumed) measurement inside a reverberation chamber is

$$\sigma = \frac{1}{\sqrt{N_{sample}}} \tag{7.22}$$

where N_{sample} is the number of independent samples, and $N_{sample} = 100$ is required for accuracy of $\pm 10\%$, i.e. ± 0.5 dB. The number of independent samples is determined primarily by the mode density in the chamber, which is indicated by Weyl's formula [98] [99]. If the frequency f is sufficiently high, the averaged mode density can be approximated as follows,

$$\left.\frac{dN_{mode}(f)}{df}\right|_{avg} = \frac{8\pi V}{c}(\frac{f}{c})^2 \tag{7.23}$$

where c is the speed of light in free space and V is the chamber volume. The integration of (7.23) leads to the averaged cumulative number of modes below a given frequency f. In practice, however, the number of modes can be counted over a certain excitation bandwidth around the operating frequency [100]

$$\left.N_{mode}(f)\right|_{avg} = \frac{8\pi V}{c}(\frac{f}{c})^2(B_{fs} + \Delta f) \tag{7.24}$$

where B_{fs} is the bandwidth of the frequency stirring in the chamber and Δf is the same as in (7.20). The number of independent samples is proportional to the mode density in the chamber. As discussed in [101], the E_z and H_z fields (relative to the z-direction) of the TE and TM modes in a rectangular cavity (dimensions: $a \times b \times c$) can be written in a compact form with Cartesian coordinates $(\hat{x}, \hat{y}, \hat{z})$,

$$\begin{aligned} E_z^{TM} &= \text{const}^{TM} \cdot \Sigma e^{-j(\pm\frac{\pi N_a}{a}\hat{x} \pm \frac{\pi N_b}{b}\hat{y} \pm \frac{\pi N_c}{c}\hat{z})\cdot(x\hat{x}+y\hat{y}+z\hat{z})} \\ H_z^{TE} &= \text{const}^{TE} \cdot \Sigma e^{-j(\pm\frac{\pi N_a}{a}\hat{x} \pm \frac{\pi N_b}{b}\hat{y} \pm \frac{\pi N_c}{c}\hat{z})\cdot(x\hat{x}+y\hat{y}+z\hat{z})} \end{aligned} \tag{7.25}$$

where the integer indexes N_a, N_b and N_c determine the resonance frequency f_{res} of both TE and TM modes [102],

$$f_{res} = \frac{c}{2}\sqrt{(\frac{N_a}{a})^2 + (\frac{N_b}{b})^2 + (\frac{N_c}{c})^2} \tag{7.26}$$

It can be noticed that each cavity mode, either TE or TM, can in general be written as a sum of eight plane waves due to permutation of the ± signs in (7.25), except for the cases when one of the indexes is zero. In those cases, one mode can only be represented by four plane waves. Nevertheless, $N_{sample} = 8 \times N_{mode}$ is a good prediction. For example, if N_{sample} greater than 100 is demanded, then N_{mode} must be at least 13.

Complete mobile terminals, such as cell phones, can be measured in reverberation chambers with the help of a base station emulator or other wireless communication test instruments. The total radiated power (TRP) is readily measured by first finding the chamber transfer function by using a reference antenna with known efficiency, and then measuring the radiated power from the phone by a network analyzer connected to the wall antennas. The receiver sensitivity is another important feature of wireless terminals. It is characterized, for instance in CDMA systems, by the signal level needed to give a certain specified bit error rate (BER) or frame error rate (FER) . The limiting static level is, when averaged over many directions in the radiation pattern, referred to as the total isotropic sensitivity (TIS) . An alternative is to measure BER/FER during continuous fading to determine what is referred to as average fading sensitivity (AFS) [103]. The AFS is a more realistic performance parameter than TIS, and it is much faster to measure.

7.4 MIMO Performance of Multiport Eleven Antenna

As illustrated in Figure 7.2, the performance of two multiport Eleven antennas for MIMO applications has been investigated in Bluetest reverberation chamber. One is a 4-port L-band Eleven antenna with linear-polarization (1×4 model), whose geometry is the same as in Table 5.2; the other is an 8-port L-band antenna with dual-polarization (2×4 model), which is the previous antenna plus an orthogonally co-located replica of itself. First of all, we would like to clarify several definitions regarding the efficiency measurement of a multiport antenna in a multipath environment:

1. Reflection-coupling efficiency e_{rc}: This is the efficiency due to the reflected power at the excited port plus all the coupled power to the adjacent ports at the same time. For example, the e_{rc} at port 1 of a 4-port antenna can be expressed in terms of scattering parameters: $1 - |s_{11}|^2 - |s_{21}|^2 - |s_{31}|^2 - |s_{41}|^2$. A fast method to measure e_{rc} is to put the AUT inside the chamber and measure the related S-parameters by using a multiport network analyzer without stirring the chamber.

2. Radiation efficiency e_{rad}: This is the efficiency barely due to conduction and dielectric losses of the antenna.
3. Embedded element efficiency e_{emb}: This is the total efficiency of each port while all other ports being match-terminated with 50 Ω load. It includes all contributions of losses, such as reflection due to mismatch, mutual coupling and conduction-dielectric losses.

The above three efficiencies at a certain frequency can simply be connected by the following relationship,

$$e_{emb} = e_{rc} \cdot e_{rad} \tag{7.27}$$

The measurement of the averaged embedded element efficiency of any a port at a certain frequency f_c is based on a relative measurement method. First, a calibration needs to be performed to calibrate the errors due to the chamber and instrumentation. Second, we measure the received power of a nearly lossless reference antenna (with a known efficiency very close to 1) within a frequency range (in our case, 1300-1700 MHz), in the presence of the AUT inside the chamber as well. Then we average the received power over the 3 wall antennas as well as over a certain frequency window. In our case, the frequency window is $[f_c - 10\ MHz, f_c + 10\ MHz]$ and the number of frequency points, N_{frq}, becomes 21, because of the 1 MHz step. In this way, we obtain $\overline{P_{ref}}$. It should be noted that both the reference antenna and the AUT should be separated at least half wavelength away from each other as well as from any other objects in the chamber, such as walls, the head phantom, etc. Third, we measure the received power of the AUT, in the presence of the reference antenna inside the chamber and keeping all other objects the same as before. This is necessary because the loading of the chamber (the Q-factor) needs to be the same during measurements of both the reference antenna and the AUT. Then we average the received power over the 3 wall antennas, over all the platform positions (in our case, the number of platform positions, N_{pos}, is 200) and over the same frequency window as before. By this means, we get $\overline{P_{AUT}}$. Finally, the ratio between $\overline{P_{AUT}}$ and $\overline{P_{ref}}$ is the averaged embedded element efficiency of one port at a certain frequency, $\overline{e_{emb}}$.

The measurement of diversity gain at a certain frequency f_c can be done at the same time as the embedded element efficiency is measured. Based on the received power by the multiport AUT, we by selecting the instantaneous maximum combine the power samples received on all branches into an optimal selection-combined MIMO branch. Then, we normalize the received power at every physical branch as well as the virtual MIMO branch by $\overline{P_{ref}}$ before we plot CDF curves concerning the received power at every branch. Besides, by applying (7.11) and (7.19), we can plot two theoretical CDF curves of Rayleigh distribution with and without selection combining. At a certain outage probability level (in our case, 1%) in the CDF plot, the difference in dB between any a branch and the MIMO branch indicates the apparent diversity gain DG_{app}, whereas the difference between the theoretical Rayleigh reference and the MIMO branch indicates the effective

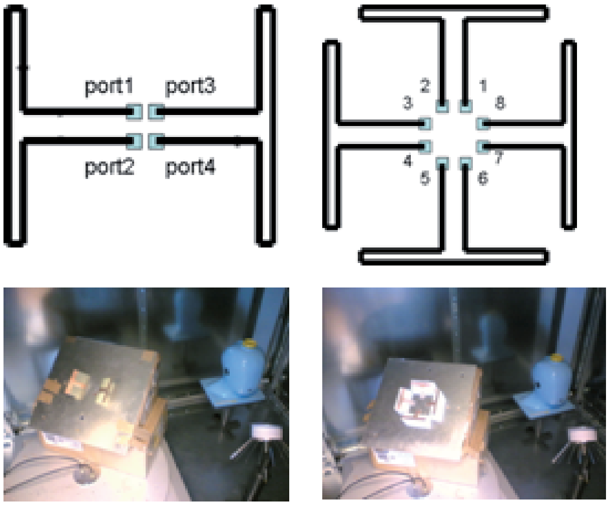

Figure 7.2: Setup for measuring 3x4 (left) and 3x8 (right) MIMO system (3 wall antennas, 4 or 8 AUT ports). The antenna is a 1x4 and 2x4 port Eleven antenna, respectively, and the three antenna elements in the MIMO systems are the three orthogonal wall antennas in the reverberation chamber.

diversity gain DG_{eff} (refer to Figure 7.3). These two quantities are associated with each other by the corresponding averaged embedded element efficiency [68],

$$DG_{eff} = \overline{e_{emb}} \cdot DG_{app} \tag{7.28}$$

As for a 2-antenna system, in particular, the apparent diversity gain can approximately be associated with the correlation ρ between the signals on the two branches [104](p. 474)

$$DG_{app} \approx 10\sqrt{1 - |\rho|^2} \tag{7.29}$$

Moreover, the measurement of the maximum available capacity of a MIMO system at a certain frequency f_c is also a relative measurement and can be performed simultaneously as well. Based on Shannon's theory, the general formula for the maximum available capacity (bits/second/Hz) of a MIMO system with a transmit antenna with *M* (in our case, 3) ports and a receive antenna with *N* (in our case, 2, 4 or 8) ports can be expressed as [94] [105] [106],

$$\tilde{C} = log_2\{det[I_N + \frac{SNR}{M}\tilde{H}_{N\times M}\tilde{H}^*_{M\times N}]\} \tag{7.30}$$

where I_N is an identity matrix, $\tilde{H}_{N\times M}$ is a normalized complex channel matrix, and $\tilde{H}^*_{M\times N}$ is the complex conjugate transpose of the previous channel matrix. First, we normalize the complex received signal strength C_{AUT} by the square root of $\overline{P_{ref}}$ before reshape it to an $M \times N$ matrix, every element of which is an array sized by $N_{fre} \times N_{pos}$. This matrix is called the measured complex channel matrix, H_m. Then, we use MATLAB to automatically generate a theoretical complex channel matrix, H_t, which is with the same dimension as H_m and composed of normally distributed pseudorandom numbers in both real and imaginary parts. Now, we can substitute H_m and H_t into (7.30) and obtain the measured and theoretical capacities, respectively. Note that the latter is the upper limit of the available capacity of an $M \times N$ MIMO system. As long as all elements in the channel matrix are completely uncorrelated and the antennas have 100$\%$ efficiency, the capacity can reach its theoretical maximum. In the following, we will investigate different scenarios where the 4/8-port Eleven antennas are used for MIMO purposes with and without 0/180^o hybrids.

7.4.1 Scenario 1 $\&$ 2: 1×4 and 2×4 Models (Without Hybrids)

Table 7.1: Measured efficiencies, diversity gains and capacities at 1.57GHz

Antenna Model Type	1×4	2×4
Averaged return loss [dB]	-14.8	-9.7
Averaged coupling loss [dB]	-12.0	-9.8
Averaged e_{rc} [dB]	-0.44	-1.0
Averaged e_{emb} [dB]	-1.01	-1.6
Apparent Diversity Gain DG_{app} [dB]	15.6	18.5
Effective Diversity Gain DG_{eff} [dB]	14.7	17.2
Discrepancy between DG_{eff} and DG_{app}: (DG_{eff} - DG_{app}) [dB]	-0.9	-1.3
Theoretical maximum capacity @ SNR=15dB $\tilde{C}_t$ [bps/Hz]	14.3	18.3
Measured maximum capacity @ SNR=15dB $\tilde{C}_m$ [bps/Hz]	12.7	15.9
Discrepancy between $\tilde{C}_m$ and $\tilde{C}_t$: ($\tilde{C}_m$ - $\tilde{C}_t$) [bps/Hz]	-1.6	-2.4
Capacity reduction due to averaged e_{emb} (readings) [bps/Hz]	-0.9	-1.6

In scenarios 1 and 2, 1×4 (1-polarization, 4-port per polarization) and 2×4 (2-polarization, 4-port per polarization) Eleven antennas function with every individual port exploited without 0/180^o hybrids. The measured average embedded element efficiencies, diversity gains and corresponding maximum available capacities at 1.57 GHz are presented in Figure 7.3, and the results are summarized in Table 7.1.

As can be calculated from the table, the ratios between (DG_{eff} - DG_{app}) in dB and $\overline{e_{emb}}$ are 97.5$\%$ (-0.11 dB) and 93.3$\%$ (-0.3 dB), respectively, regarding the 1×4 and 2×4 antenna models. This agrees well with the relationship (7.28).

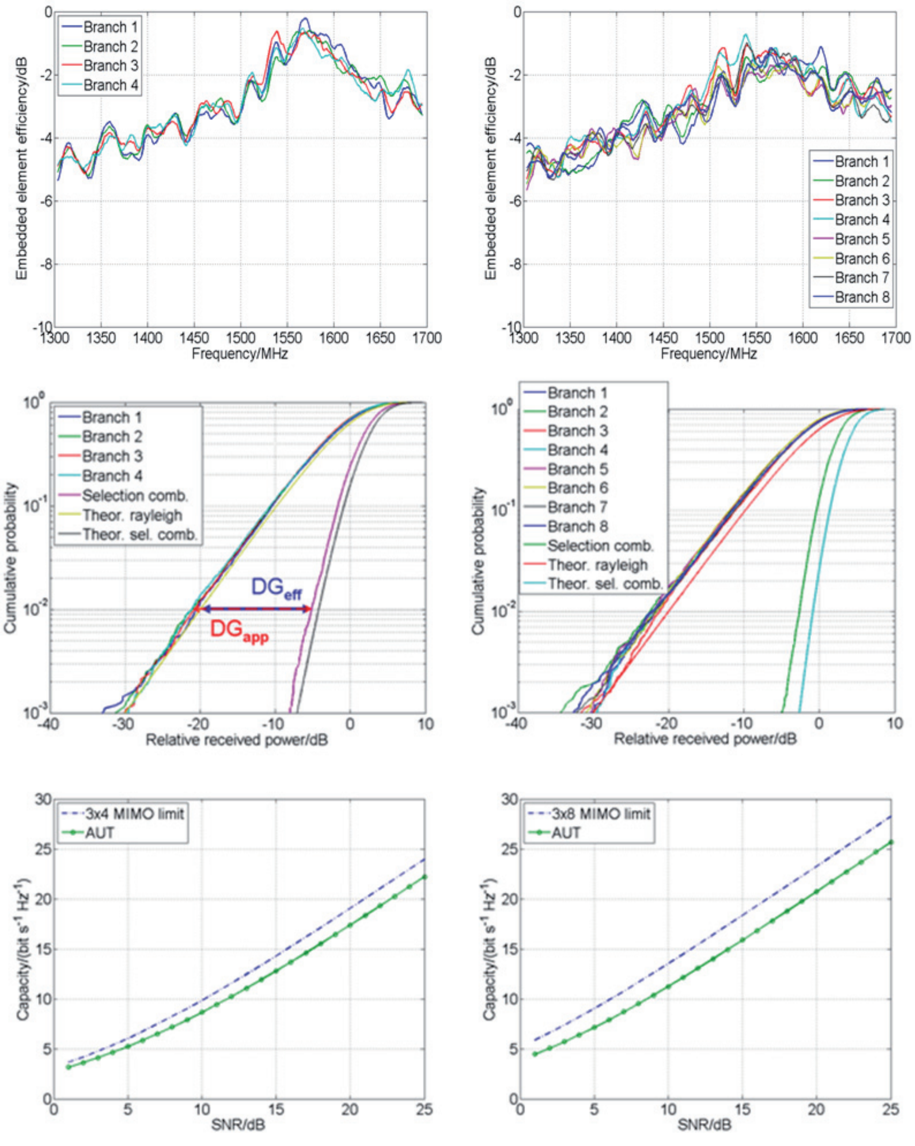

Figure 7.3: Measured embedded element efficiencies, normalized transmission CDFs and maximum available capacities (at 1.57 GHz) of 1x4 (left column) and 2x4 (right column) L-band Eleven antenna. The measurement was performed in Bluetest Reverberation chamber with accuracy of 0.5 dB standard deviation.

The capacity reduction due to $\overline{e_{emb}}$ is derived by directly reading on Figure 7.3. Regarding the 1×4 model, for instance, we read the reduction in capacity between the point of interest (SNR = 15 dB) and an imaginary point (SNR = 15 + 1.01 dB), where the embedded element efficiency is assumed as 1. It can further be observed that the ratios between the reduction in capacity due to $\overline{e_{emb}}$ and ($\tilde{C}_m$ - $\tilde{C}_t$) are 56% and 67%, respectively, for the two antenna models. This tends to indicate that the averaged embedded element efficiency plays a more significant role in the capacity reduction than any other causes, such as the correlation between different channels.

7.4.2 Scenario 3: Combined 1×2 Model (1×4 With Hybrids)

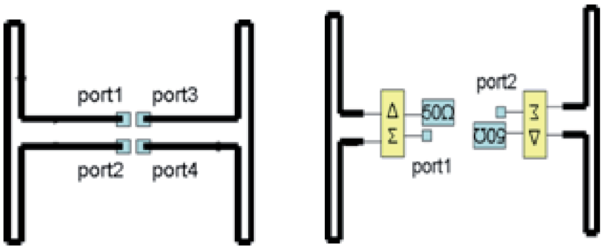

Figure 7.4: 1×4 model with hybrids turns into a model with 1×2 combined ports. 50Ω resistors load the unused hybrid ports.

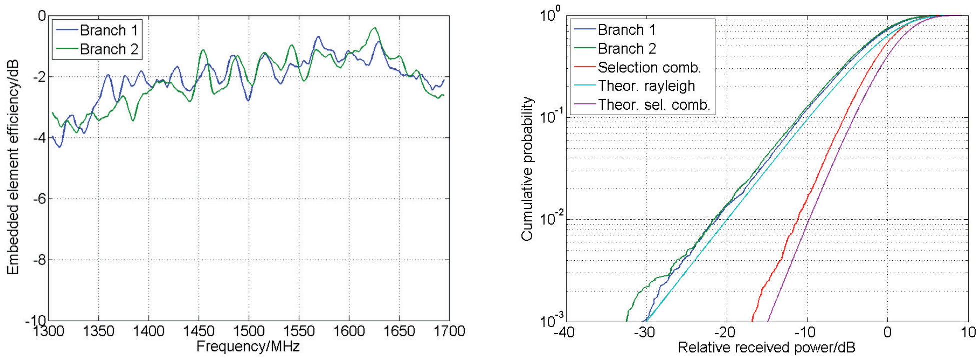

Figure 7.5: Scenario 3.1: Δ - Δ (Combined Port 1 - 2), diversity measured at 1.57 GHz.

We would like to study the scenarios in the presence of 0/180^o hybrids (with Σ and Δ ports), because the hybrids can be in practice used to feed every petal of multiport Eleven antennas. Shown in Figure 7.4 is how a 1×4 Eleven model with 2 hybrids turns into a combined 1×2 (1-polarization, 2-port per polarization) model. As a combined port can

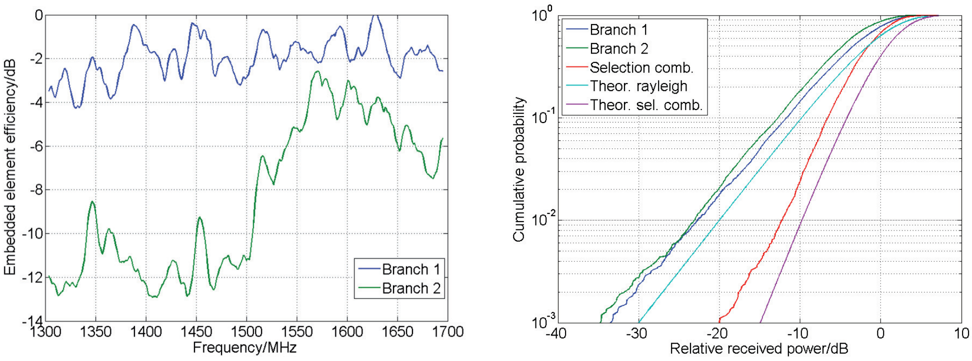

Figure 7.6: Scenario 3.2: Δ - Σ (Combined Port 1 - 2), diversity measured at 1.57 GHz.

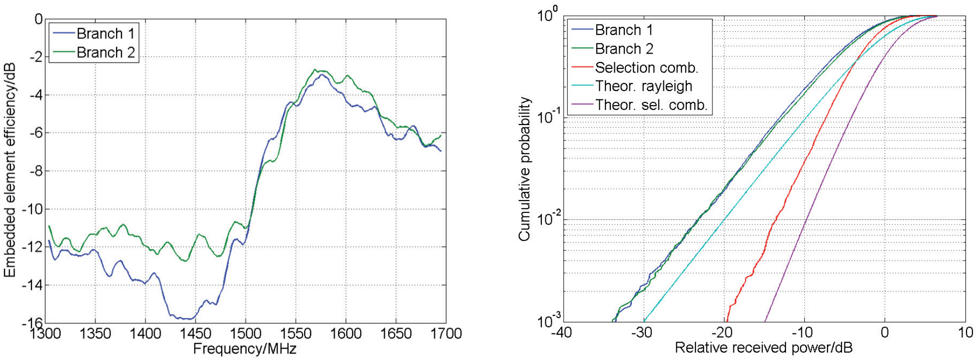

Figure 7.7: Scenario 3.3: Σ - Σ (Combined Port 1 - 2), diversity measured at 1.57 GHz.

either be Δ or Σ port, there are in total 3 different combinations of the 2 combined ports. The measured embedded element efficiencies and normalized transmission CDFs in the 3 cases are presented in Figure (7.5)-(7.7), respectively.

7.4.3 Scenario 4: Combined 2×2 Model (2×4 With Hybrids)

Shown in Figure 7.8 is how a 2×4 Eleven model together with 4 hybrids turns into a combined 2×2 (2-polarization, 2-port per polarization) model. The port definition and analysis are the same as those in the three previous cases.

Presented in Figure 7.9-7.14 are the measured embedded element efficiencies and normalized transmission CDFs in the 6 different cases. The efficiencies at the Σ ports look poorer than those at the Δ ports. It is primarily due to the poor match between the hybrid

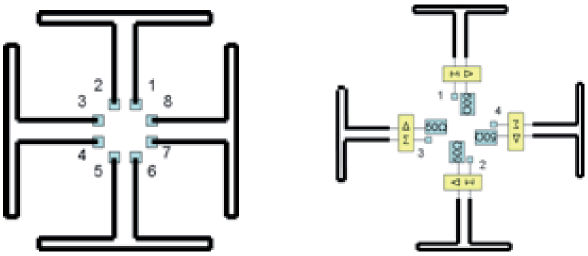

Figure 7.8: 2×4 model with hybrids turns into a model with 2×2 combined ports. 50Ω resistors load the unused hybrid ports.

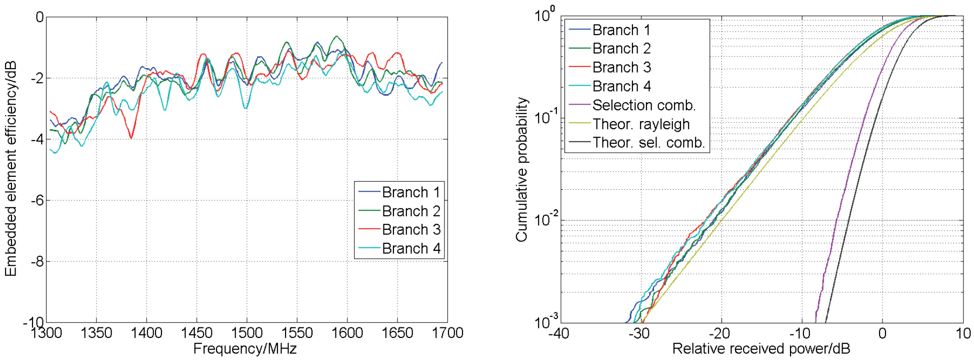

Figure 7.9: Scenario 4.1: Δ - Δ - Δ - Δ (Combined Port 1 - 2 - 3 - 4), diversity measured at 1.57 GHz.

under Σ configuration and the antenna.

The spectrum of the measured maximum available capacities at 15 dB SNR in all the above-mentioned scenarios are plotted in Figure 7.15. It can be found that the shapes of the efficiency curves and corresponding capacity curves are similar to some extent; in particular, the capacity tends to reach its maximum at the frequency where the average embedded element efficiency is highest.

In general, the more MIMO ports are exploited, the higher the capacities tend to be. In the cases of 4 MIMO ports, the curve in scenarios 4.1 seems largely better than that in scenario 1. This is because the hybrid-combined Δ ports are better matched over the whole band except for the peak (resonance) and its vicinity in our experiment. The curves in scenarios 4.3 and 4.4 almost coincide due to the same number of Σ and Δ ports, no matter what combination of the port numbers. A tight link can clearly be observed between the averaged embedded element efficiency and the maximum available capacity.

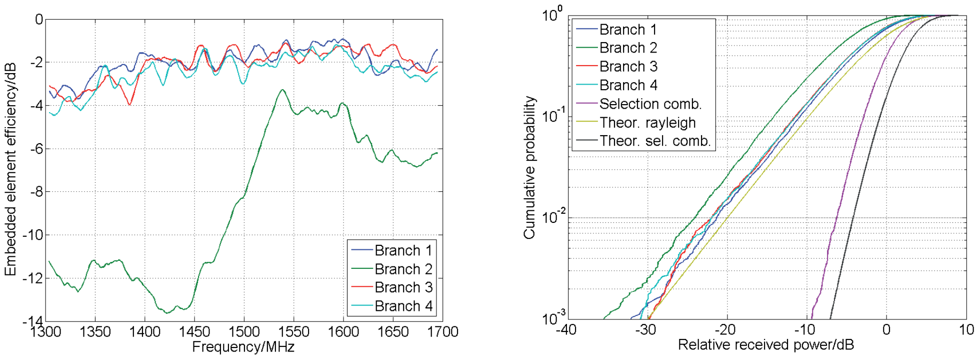

Figure 7.10: Scenario 4.2: Δ - Σ - Δ - Δ (Combined Port 1 - 2 - 3 - 4), diversity measured at 1.57 GHz.

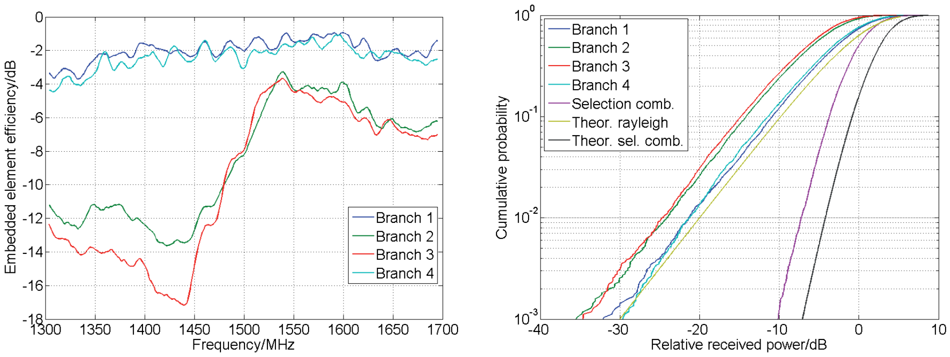

Figure 7.11: Scenario 4.3: Δ - Σ - Σ - Δ (Combined Port 1 - 2 - 3 - 4), diversity measured at 1.57 GHz.

For interested readers, by the way, measurement results of the diversity gain and embedded element efficiency over entire S- and C- bands of a 2-13 GHz Eleven feed can be found in [107].

7.5 Summary of Chapter 7

The embedded element efficiency, diversity gain and maximum available capacity of two L-band multiport Eleven antennas have been experimentally investigated in a reverberation chamber that is capable of emulating an isotropic Rayleigh fading environment.

Without hybrids, the two multiport Eleven antennas can be considered as 1×4 and 2×4

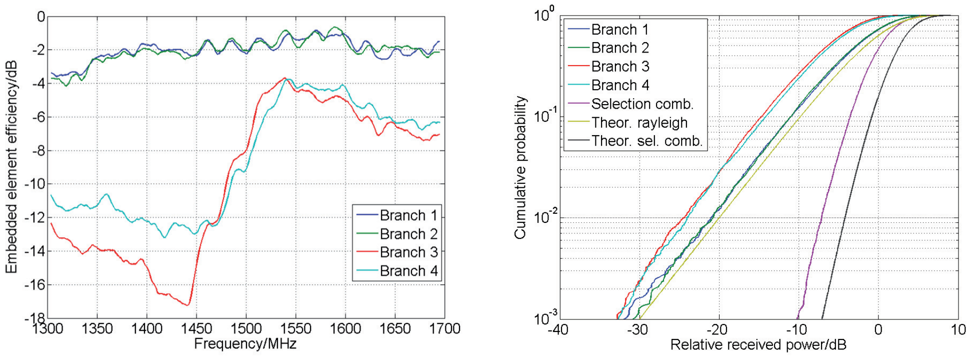

Figure 7.12: Scenario 4.4: Δ - Δ - Σ - Σ (Combined Port 1 - 2 - 3 - 4), diversity measured at 1.57 GHz.

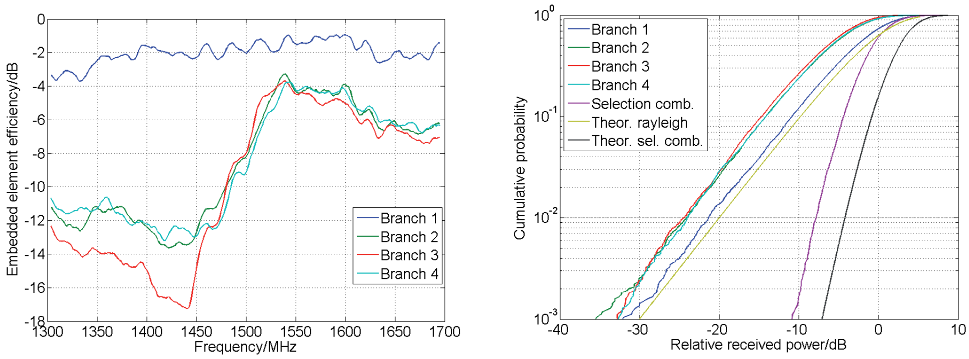

Figure 7.13: Scenario 4.5: Δ - Σ - Σ - Σ (Combined Port 1 - 2 - 3 - 4), diversity measured at 1.57 GHz.

scenarios, respectively, where each port of an antenna petal is individually used and 'identical' to others, since the normalized transmission CDF curves at each port look almost identical. In the presence of $0/180^\circ$ hybrids, in contrast, the previous 1×4 and 2×4 scenarios are thus reduced to combined 1×2 and 2×2 configurations, respectively, corresponding to a number of scenarios where there exist different combinations of Σ and Δ ports. As can be found from the measurement results, in general, a Δ port is better than a Σ port in terms of a higher effective diversity gain as well as a higher embedded element efficiency at the considered resonant frequency. It can also be found, in general, the more diversity ports are used, the higher the maximum available capacity tends to be. Besides, the averaged embedded element efficiency curves and corresponding capacity curves look similar in shape; especially, the capacity tends to reach its maximum at a frequency where the averaged embedded element efficiency is also maximum.

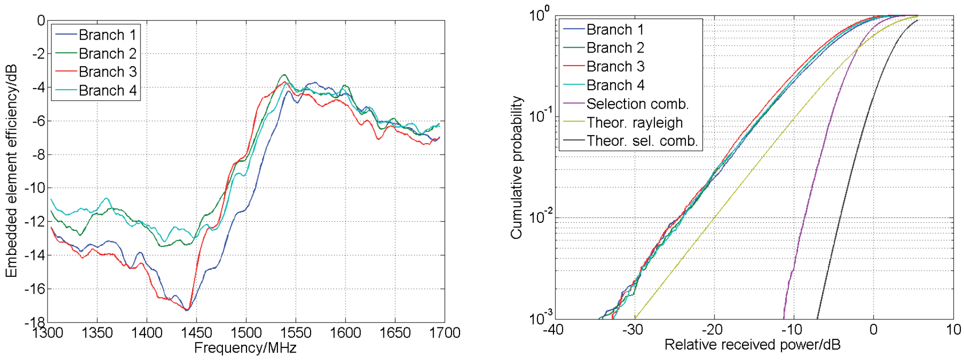

Figure 7.14: Scenario 4.6: Σ - Σ - Σ - Σ (Combined Port 1 - 2 - 3 - 4), diversity measured at 1.57 GHz.

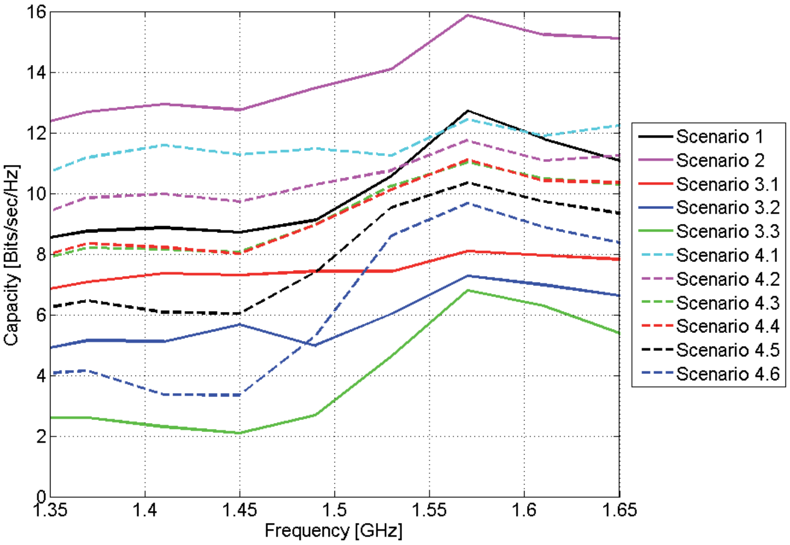

Figure 7.15: Measured maximum available capacities of Eleven models varying with frequency (40 MHz interval) in all the scenarios (SNR = 15 dB).

To sum up, a tight link can be observed between the embedded element efficiency and the maximum available capacity; in particular, the embedded element efficiency seems to play a more significant role in the capacity reduction than any other causes.

Chapter 8

Conclusion and Future Work

Folded dipoles, typically matched to 300 Ω transmission lines, are traditionally used in various applications within the VHF/UHF bands. A folded dipole can be thought of as the fatter version of a wire dipole, and its impedance bandwidth is wider than that of the wire dipole. The concept of two cross-connected folded dipoles, called orthogonal folded dipoles (OFD), is introduced in Chapter 3. This antenna can be fed through different combinations of feed nodes at the center, resulting in the dual-band and the wide-band modes, respectively. The impedance can be matched well to 300 Ω in both modes, while the properties of the radiation patterns in the two modes vary quite little, but for ±45° rotation of the E/H planes. The orthogonal folded dipoles have potential pattern reconfigurability in terms of switchable types and orientations of polarizations.

As described in Chapter 4, a log-periodic folded dipole array (LPFDA) radiates its endfire main beam in the direction of the shorter dipoles in the array, similar to the conventional crisscross-fed log-periodic dipole array (LPDA). The partly and fully scaled LPFDAs have respectively been simulated and optimized for the reflection coefficient. The latter seems much more likely to be impedance-matched over a wide band than the former; the latter also outperforms the former in radiation characteristics, such as the directivity, the front-to-back ratio and the relative crosspolar level. One or two pairs of identical LPFDA petals can be oppositely placed over and rotated from a PEC ground plane, giving rise to the so-called Eleven antenna with linear or dual polarizations, respectively.

As it turns out in Chapter 6, the Eleven antenna has been gradually improved in term of matching as well as efficiencies, and its functional properties have become better understood. A decade bandwidth, an unchanged phase center and nearly constant directivities over the decade band can be regarded as the major figure-of-merit of the Eleven antenna; besides, it has low profile, low side-/back-lobes and its 10 dB semi-beamwidth is 50-60° over the entire band, making it suitable as feed for reflectors, in particular, primary-fed ones. The previous delivery of the Eleven feed includes radio telescopes at Green Bank

(USA), RATAN (Rassia) and GMRT (India), etc; moreover, the Eleven feed is hoped to be used in many other radio telescope sites and projects (e.g. VLBI2010, US SKA, etc.) in the future and help push the science of radio astronomy forward.

In principle, there is no theoretical limit to the bandwidth of this log-periodic antenna. In practice, however, the bandwidth is inevitably limited by the specified size of the antenna at low frequencies and by mechanical and cryogenic problems on the antenna petals and some issues on the center puck, etc., at high frequencies, particularly in Ku-band and above. In order to enhance the radiation performance at up to 14 GHz, a new concept of rotationally symmetric circular Eleven feed is introduced and numerically investigated in Chapter 6 as well. Compared with the straight version of an 8-dipole-pair Eleven simulation model, a circular Eleven simulation model with the same number of dipole pairs shows higher BOR1 efficiency as well as aperture efficiency in the amount of a fraction of dB. In order to verify this new concept, a project has already been started to manufacture and measure a 2-14 GHz circular Eleven feed. Hopefully, the experimental results of this antenna will be reported in the near future.

Although further improvements of the Eleven antenna as feed for radio telescopes are still possible, many other potential versatilities in connection with multifunctional antenna systems are also interesting. First, the radiation patterns for monopulse tracking can be achieved through different excitation combinations with respect to the multiport configuration of the Eleven antenna. This concept was verified by analytical studies, numerical simulations and experiments on an L-band lab model for use in satellite terminals. As summarized in Chapter 5, the sum and the horizontal difference patterns perform better for tracking than the vertical difference pattern does. Therefore, a sequential tracking procedure is needed to make it up for tracking in two orthogonal planes. Second, the Eleven antenna with MIMO diversity ports can possibly overcome narrowband multipath fading in a real radio link. This idea was verified by measuring the diversity gain and maximum available capacity of two L-band lab models in a reverberation chamber that emulates an isotropic Rayleigh fading environment. The results in Chapter 7 reveal that the diversity Eleven antenna can improve the link quality in terms of a significant diversity gain and high capacity at the receiving end. In addition, it is experimentally observed that the embedded element efficiency plays a very important role to realize the maximum available capacity of a radio channel in a multipath environment.

In the following, several specific research activities are suggested for future elaboration.

First of all, as was pointed out before, there remain some work that can further be done on the circular Eleven feed. It is believed that there is still room for improving the reflection coefficient of the feed over the whole band through optimization, while keeping the radiation properties good enough. In particular, when the feed is integrated with the center puck, baluns, low-noise amplifiers, cooling devices and so on, it is thus important to investigate the system performance, including G/T and thermal issues, etc., of such a cryogenic active antenna.

Second, it is of great interest to look into whether monopulse tracking can be realized on a wideband Eleven antenna, how the related patterns and efficiencies vary with frequency, and whether the phase steering is feasible over the whole band. On top of this, multiple (e.g. 4) dually-polarized wideband Eleven antennas may be considered to construct a wideband beam-steering array with monopulse tracking capability on dual polarizations in two orthogonal planes.

Last but not least, extensive efforts are needed to make use of a diversity Eleven antenna in a wideband MIMO system. Hopefully, this track will lead to employing the Eleven antenna in wideband MIMO base stations in the future.

Bibliography

[1] Adeel Yasin, Jian Yang, and Tomas Östling. "A compact dual-band feed for reflector antennas based on choke horn and circular Eleven antenna". *IEEE Transactions on Antennas and Propagation*, 57(10):3300–3302, Oct. 2009.

[2] J. Yang, X. Chen, N. Wadefalk, and P.-S. Kildal. "Design and realization of a linearly polarized Eleven feed for 1-10 GHz". *IEEE Antennas and Wireless Propagation Letters*, 8:64–68, 2009.

[3] W. L. Stutzman and G. A. Thiele. *Antenna Theory and Design*. John Wiley & Sons. Inc., second edition, 1998.

[4] *CST Studio Suite 2010 User's Manual*. 2010.

[5] Y. B. Karandikar and P.-S. Kildal. "Optimization of 200-800 MHz Eleven antenna feed for GMRT". *Proc. of* 2^{nd} *European Conference on Antennas and Propagation (EuCAP)*, 2007.

[6] R. Olsson, P.-S. Kildal, and J. Yang. "Development of three models of the Eleven antenna: A new decade bandwidth high performance feed for reflectors". *Proc. of* 1^{st} *European Conference on Antennas and Propagation (EuCAP)*, 2006.

[7] J. Yang and P.-S. Kildal. "Optimization of reflection coefficient of large log-periodic array with prediction from a small part of the array". *IEEE Transactions on Antennas and Propagation*, 58(12), Dec. 2010.

[8] S. Ananthakrishnan. "The Giant Metrewave Radio Telescope". *Journal of Astrophysics and Astronomy*, 16:427–235, 1995.

[9] *Introducing GMRT*. Available: http://www.gmrt.ncra.tifr.res.in, 2008.

[10] T. Minter. "The proposer's guide for the Green Bank Telescope". Jan. 2010.

[11] *Robert C. Byrd Green Bank Telescope*. Available: http://www.gb.nrao.edu, 2008.

[12] *SKA Brochure*. Available: http://www.skatelescope.org, 2010.

[13] *VLBI 2010*. Available: http://www.haystack.mit.edu/geo/vlbi_td/2010/index.html, 2010.

[14] P.-S. Kildal and S. A. Skyttemyr. "Dipole-disk antenna with beam-forming ring". *IEEE Transactions on Antennas and Propagation*, pages 529–534, Jul. 1982.

[15] P.-S. Kildal, S. A. Skyttemyr, and A. A. Kishk. "G/T maximization of a paraboidal reflector fed by a dipole-disk antenna with ring by using the multiple-reflection approach and the moment method". *IEEE Transactions on Antennas and Propagation*, 45(7):1130–1139, Jul. 1997.

[16] W. N. Christiansen and J. A. Högbom. *Radiotelescopes*. Cambridge University Press, 1969.

[17] B. Thomas, K. Greene, and G. James. "A wideband prime-focus horn for low-noise receiver applications". *IEEE Transactions on Antennas and Propagation*, 38(11):1898–1900, Nov. 1990.

[18] B. Thomas, G. James, and K. Greene. "Design of wideband corrugated conical horns for casegrain antennas". *IEEE Transactions on Antennas and Propagation*, 34(6):750–757, Jun. 1986.

[19] P. R. Clark and G. L. James. "Ultra wideband hybrid-mode feeds". *IEEE Electronics Letters*, 31(23):1968–1969, Nov. 1995.

[20] P. Clarricoats, A. Olver, and et al. "Broadband low-crosspolarization horn". *IEEE Electronics Letters*, 30(25):2085–2086, Dec. 1994.

[21] E. Lier. "A dielectric hybrid mode antenna feed: A simple alternative to the corrgated horn". *IEEE Transactions on Antennas and Propagation*, 38(1):21–29, Jan. 1986.

[22] C. Bruns, P. Leuchtmann, and R. Vahlldieck. "Analysis and simulation of a 1-18 GHz boradband double-ridged horn antenna". *IEEE Transactions on Electromagnetic Compatibility*, 45(1):55–60, Feb. 2003.

[23] J. Shimizu. "Octave-bandwidth feed horn for paraboloid". *IEEE Transactions on Antennas and Propagation*, 9(2), 1961.

[24] Z. Ying, A. A. Kishk, and P.-S. Kildal. "Broadband compact horn feed for prime-focus reflectors". *IEEE Electronics Letters*, 31(14):1114–1115, Jul. 1995.

[25] P.-S. Kildal. "The hat feed: a dual-mode rear-radiating waveguide antenna having low cross-polarization". *IEEE Transactions on Antennas and Propagation*, 35(9):1010–1016, 1987.

[26] J. Yang and P.-S. Kildal. "Calculation of ring-shaped phase centers of feeds for ring-focus paraboloids". *IEEE Transactions on Antennas and Propagation*, 48(4):524–528, Apr. 2000.

[27] W. Wei, J. Yang, T. Östling, and T. Schafer. "New hat feed for reflector antennas realised without dielectrics for reducing manufacturing cost and improving reflection coefficient". *IET Microw. Antennas Propag.*, 5(7):837–843, 2011.

[28] J. Hansen, A. A. Kishk, P.-S. Kildal, and O. DahlsjÖ. "High performance reflector hat antenna with very low sidelobes for radio-link applications". *IEEE AP-S International Symposium*, 1995.

[29] Denstedt M., T. Östling, J. Yang, and P.-S. Kildal. "Tripling bandwidth of hat feed by genetic algorithm optimization". *IEEE AP-S International Symposium*, 2007.

[30] D. E. Isbell. "Log-periodic dipole arrays". *IRE Transactions on Antennas and Propagation*, 8(3):260–270, May 1960.

[31] R. Dybdal. "Defocusing loss for a log periodic fed reflector". *IEEE Transactions on Antennas and Propagation*, 33(7):809–812, Jul. 1985.

[32] G. Engargiola. "Non-planar log-periodic antenna feed for integration with cryogenic microwave amplifier". *IEEE AP-S International Symposium and UNSC/URSI National Radio Science Meetings*, pages 140–143, 2002.

[33] J. Welch and et al. "The Allen Telescope Array: The first widefield, panchromatic, snapshot radio camera for radio astronomy and SETI. *Proceedings of the IEEE*, 97(8):1438–1447, Aug. 2009.

[34] D. Ericsson, P.-S. Kildal, and S. Weinreb. "Study of efficiencies and phase centers of broadband log-periodic feeds for large offset dual-reflector antennas using formulas for bodies of revolution". *IEEE AP-S International Symposium*, 2003.

[35] R. Olsson, P.-S. Kildal, and S. Weinreb. "The Eleven antenna: A compact low-profile decade bandwidth dual polarized feed for reflector antennas". *IEEE Transactions on Antennas and Propagation*, 54(2):368–375, 2006.

[36] G. Cortes-Medellin. "Novel nonplanar ultra wide band quasi self-complementary antenna". *Proc. of IEEE AP-S Symposium*, pages 5733–5736, Jun. 2007.

[37] V. Rodriguez. "An open-boundary quad-ridged guide horn antenna for use as a source in antenna pattern measurement anechoic chamber". *IEEE Antennas Propoga. Mag.*, 48(2):157–160, Apr. 2006.

[38] J. Yang, S. Pivnenko, and P.-S. Kildal. "Comparison of two decade-bandwidth feeds for reflector antennas: the Eleven antenna and quadridge horn". *Proc. of 4*th *European Conference on Antennas and Propagation (EuCAP)*, 2010.

[39] R. F. Harrington. "Matrix method for field problems". *Proc. IEEE*, 55, Feb. 1967.

[40] R. F. Harrington. *Field Calculation by Moment Methods*. Macmillan, New York, 1968.

[41] *MININEC Professional Software*. EM Scientific Inc., Carson City, NV, 1995.

[42] J. H. Richmond. "Computer program for thin-wire structures in a homogeneous conducting medium". *Natoinal Technical Information Service*, NASA CR-2399, July 1973.

[43] G. J. Burke and A. J. Poggio. "Numerical EM Code (NEC) - Method of Moments". *Tech. Doc. prepared for Naval Ocean Systems Center*, NOSC/TD 116, 1980.

[44] D. B. Davidson and et al. "Recent progress on the antenna simulation program FEKO". *Proc. of the 1998 South African Symposium on Communications and Signal Processing*, 1998.

[45] S. M. Rao, D. R.Wilton, and A.W. Glisson. "Electromagnetic scattering by surfaces of arbitrary shape". *IEEE Transactions on Antennas and Propagation*, 30:409–418, 1982.

[46] B. M. Kolundzija and A. M. Djordjevic. *Electromagnetic modeling of composite metallic and dielectric structures*. Artech House, Norwood, MA, USA, 2002.

[47] V. H. Rumsey. "The reaction concept in electromagnetic theoty". *Physics Review*, Series 2, vol. 94, 1954.

[48] G. A. Thiele. *Computer Techniques for Electromagnetics*. Pergamon Press, New York, 1973.

[49] T. Weiland. "A discretization method for the solution to Maxwell's equations for six-component fields". *Electronics and Communication (AEÜ)*, 31:116–120, 1977.

[50] T. Weiland. "Time domain electromagnetic field computation with finite difference methods". *International Journal of Numerical Modelling*, 9:295–319, 1996.

[51] J. P. Berenger. "A perfect matched layer for the absorption of electromagnetic waves". *Journal of Computational Physics*, 114:185–200, 1994.

[52] T. Weiland. "RF and microwave simulator - from component to system design". *Proceedings of the European Microwave Week*, 2:591–596, Oct. 2003.

[53] B. Krietenstein, et al, and T. Weiland. "The perfect boundary approximation technique facing the challenge of high precision field computation". *Proc. of the International Accelerator Conference (LINAC)*, pages 860–862, 1998.

[54] M.Srinivas and Lalit M.Patnaik. "Genetic Algorithms: A Survey". *IEEE Computer*, 27(6):17–26, June 1994.

[55] D. S. Weile and E. Michielssen. "Genetic algorithm optimization applied to electromagnetics: A review". *IEEE Trans. Antennas Propagat.*, 45(7):343–353, Mar. 1997.

[56] J. Michael Johnson and Yahya Rahmat-Samii. "Genetic Algorithms in engineering electromagnetics". *IEEE Antennas and Propagation Magazine*, 39(4):7–21, Aug. 1997.

[57] Constantine A. Balanis. *Antenna Theory, Analysis and Design*. John Wiley & Sons. Inc., third edition, 2005.

[58] G. A. Thiele, E. P. Ekelman, Jr., and L. W. Henderson. "On the accuracy of the transmission line model for folded dipole". *IEEE Transactions on Antennas and Propagation*, 28(5):700–703, Sep. 1980.

[59] Y.-H. Huang, Q. Wu, and Q.-Zh. Liu. "Broadband dual-polarised antenna with high isolation for wireless communication". *IEEE Electronics Letters*, 45(14), Jul. 2009.

[60] G. J. Hawkins, D. J. Edwards, and J. P. McGeehan. "Tracking systems for satellite communications". *IEE Proceedings*, 135(5), 1988.

[61] P.-S. Kildal. "Broadband multi-dipole antenna with frequency-independent radiation characteristics". *Patent application PCT/SE2004/001178.*

[62] Rikard Olsson. "Development of the Eleven antenna - a decade bandwidth feed for reflector antenna". *Thesis for the degree of Licentiate of Engineering, Chalmers University of Technology*, 2005.

[63] Rikard Olsson, P.-S. Kildal, and S. Weinreb. "A novel low-profile log-periodic ultra wideband feed for the dual-reflector antenna of US-SKA. *IEEE AP-S International Symposium*, 2004.

[64] P.-S. Kildal. *Foundamentals of Antennas – A Unified Approach.* Studentlitteratur i Sverige, 2000.

[65] R. E. Collin. *Foundations for Microwave Engineering*. McGraw-Hill, Inc., 1992.

[66] T. S. Saad, R. C. Hansen, and G. J. Wheeler. *Microwave Engineers' Handbook*. Artech House Inc., 1971.

[67] Rikard Olsson, P.-S. Kildal, and Mike Shields. "Measurements of a 150 to 1700 MHz low loss Eleven Feed for the 42 m radio telescope at Green Bank". *IEEE AP-S International Symposium*, 2006.

[68] P.-S. Kildal and K. Rosengren. "Correlation and capacity of MIMO systems and mutual coupling, radiation efficiency and diversity gain of their antennas: Simulations and measurements in reverberation chamber". *IEEE Communications Magazine*, 42(12):102–112, 2004.

[69] S. Bruni, A. Neto, and F. Marliani. "The ultrawideband leaky lens antenna". *IEEE Transactions on Antennas and Propagation*, 55(10):2642–2653, 2007.

[70] S.-Y. Chen, P.-H. Wang, and P. Hsu. "Uniplanar log-periodic slot antenna fed by a CPW for UWB applications". *IEEE Antennas and Wireless Propagation Letters*, 5:256–259, 2006.

[71] P. Hall. *The SKA: An Engineering Perspective*. Dordrecht The Netherlands: Springer, 2005.

[72] I. Oppermann, M. Hamalainen, and J. Linatti. *UWB Theory and Applications.* Wiley, 2004.

[73] P.-S. Kildal and Z. Sipus. "Classification of rotationally symmetric antennas as types BOR0 and BOR1". *IEEE Antennas Propag. Mag.*, 37(6):114, Dec. 1995.

[74] J. Yang and P.-S. Kildal. "Optimizing large log-periodic array by computing a small part of it". *IEEE Transactions on Antennas and Propagation*, 59(3), Mar. 2011.

[75] J. Yang, M. Pantaleev, P.-S. Kildal, B. Klein, Y. Karandikar, L. Helldner, N. Wadefalk, and C. Beaudoin. "Cryogenic 2-13 GHz Eleven Feed for reflector antennas in future wideband radio telescopes". *IEEE Transactions on Antennas and Propagation*, 59(6):1918–1934, Jun. 2011.

[76] R. H. Clarke. "A statistical theory of mobile radio reception". *Bell System Technical Journal*, 47:957–1000, 1968.

[77] T. Aulin. "A modified model for the fading signal at a mobile radio channel". *IEEE Transactions on Vehicular Technology*, 28(3):182–203, 1979.

[78] William C. Jakes. *Microwave Mobile Communications.* IEEE Press, 1974.

[79] R. Steele and L. Hanzo. *Mobile Radio Communications*. John Wiley & Sons., 1998.

[80] S. M. Saunders and A. A. Zavala. *Antennas and Propagation for Wireless Communication Systems.* John Wiley & Sons, Ltd., 2007.

[81] Andreas F. Molisch. *Wireless Communications.* Wiley, IEEE Press, 2005.

[82] A. M. D. Turkmani et al. "An experimental evalution of the performance of two-branch space and polarization diversity schemes at 1800 MHz.

[83] P. C. F. Eggers et al. "Base station polarization diversity reception for mobile radio". *IEEE Journal on Selected Areas in Communications*, 11(7):1046–1057, 1993.

[84] S. Kozono, T. Tsuruhara, and M. Sakamoto. "Base station polarization diversity reception for mobile radio". *IEEE Transactions on Vehicular Technology*, 33(4):301–306, 1984.

[85] R. G. Vaughan. "Polarization diversity in mobile communications". *IEEE Transactions on Vehicular Technology*, 39(3):177–186, 1990.

[86] H. A. Mendes. "A new approach to electromagnetic field-strength measurements in shielded enclosures". *Wescon Tech. Papers*, 1968.

[87] D. A. Hill et al. "Aperture excitation of electrically large, lossy cavity". *IEEE Transactions on Electromagnetic Compatibility*, 36(3), 1994.

[88] D. A. Hill. "Plane wave integral representation for fields in reverberation chamber". *IEEE Transactions on Electromagnetic Compatibility*, 40(3), 1998.

[89] D. A. Hill. "Linear dipole response in a reverberation chamber". *IEEE Transactions on Electromagnetic Compatibility*, 41(4), 1999.

[90] J. G. Kostas and B. Boverie. "Statistical model for a mode-stirred chamber". *IEEE Transactions on Electromagnetic Compatibility*, 33(4), 1991.

[91] P.-S. Kildal et al. "Designing reverberation chambers for measurements of small antennas and wireless terminals: accuracy, frequency resolution, lowest frequency of operation, loading and shielding of chamber". *Proc. of First European Conference on Antennas and Propagation (EuCAP)*, 2006.

[92] L. Garcia-Garcia and B. Lindmark et al. "MIMO capacity of antenna arrays evaluated using radio channel measurements, reverberation chamber and radiation patterns". *IET Microwaves, Antennas and Propagation*, 1(6), 2007.

[93] K. Rosengren and P.-S. Kildal et al. "Characterization of antennas for mobile and wireless terminals in reverberation chambers: Improved accuracy by platform stirring". *Microwave and Optical Technology Letters*, vol.30, 2001.

[94] John L. Volakis. *Antenna Engineering Handbook: Chapter 58*. McGraw-Hill Professional, fourth edition, 2007.

[95] P.-S. Kildal et al. "Measurement of free space impedances of small antennas reverberation chambers". *Microwave and Optical Technology Letters*, 32(2), 2002.

[96] C. L. Holloway et al. "On the use of reverberation chambers to simulate a controllable Rician radio environment for the testing of wireless devices". *IEEE Transactions on Antennas and Propagation*, 54(11), 2006.

[97] P.-S. Kildal and C. Carlsson. "Detection of a polarization imbalance in reverberation chambers and how to remove it by polarization stirring when measuring antenna efficiencies". *IEEE Communications Magazine*, 42(12), 2004.

[98] L. R. Arnaut. "Operation of electromagnetic reverberation chambers with wave diffractors at relatively low frequencies". *IEEE Transactions on Electromagnetic Compatibility*, 43(4), 2001.

[99] G. Orjubin et al. "Chaoticity of reverberation chamber assessed from the analysis of modal distributions obtained by FEM". *IEEE Transactions on Electromagnetic Compatibility*, 49(4), 2007.

[100] Y. B. Karandikar, D. Nyberg, N. Jamaly, and P.-S. Kildal. "Mode counting in rectangular, cylindrical and spherical cavities with applications to wireless measurements in reverberation chambers". *IEEE Transactions on Electromagnetic Compatibility*, 51(4), 2009.

[101] K. Rosengren and P.-S. Kildal. "Study of distributions of modes and plane waves in reverberation chambers for the characterization of antennas in a multipath environment". *Microwave And Optical Technology Letters*, 30(6), 2001.

[102] Roger F. Harrington. *Time-Harmonic Electromagnetic Fields*. McGraw-Hill Book Company, 1961.

[103] C. Orlenius, P.-S. Kildal, and G. Poilasne. "Measurement of total isotropic sensitivity and average fading sensitivity of CDMA phones in reverberation chamber". *IEEE AP-S International Symposium*, July, 2005.

[104] M. Schwartz, W. R. Bennett, and S. Stein. *Communication System and Techniques*. McGraw-Hill, New York, 1965.

[105] G. J. Foschini and M. J. Gans. *Wireless Personal Communications 6: On Limits of Wireless Communications in a Fading Environment when Using Multiple Antennas*. Kluwer Academic Publishers, 1998.

[106] David Tse and Pramod Viswanath. *Fundamentals of Wireless Communication.* Cambridge University Press, 2005.

[107] Jian Yang and et al. "Measurements of diversity gain and radiation efficiency of the Eleven antenna by using different measurement techniques". *Proc. of* 4^{th} *European Conference on Antennas and Propagation (EuCAP)*, 2010.

[108] P.-S. Kildal. "Factorization of the feed efficiency of paraboloids and cassegrain antennas". *IEEE Transactions on Antennas and Propagation*, 33(8):903–908, 1985.

Appendix A

Computation of Aperture Efficiencies

A.1 Radiated Power

In a spherical coordinate system, the electrical far field at an arbitrary point can be expressed locally as a plane wave for large distance *r*,

$$\vec{E}(r,\theta,\phi) = \frac{1}{r}e^{-jkr}\vec{G}(\theta,\phi) = \frac{1}{r}e^{-jkr}[G_{co}(\theta,\phi)\hat{co} + G_{xp}(\theta,\phi)\hat{xp}] \tag{A.1}$$

where 1/*r* is the divergence factor, e^{-jkr} is the phase factor and $\vec{G}(\theta,\phi)$ is the complex far-field function [64], $G_{co}(\theta,\phi)$ and $G_{xp}(\theta,\phi)$ are the co- and cross-polar far-field components, respectively.

The total radiated power is given by [64]

$$P_{rad} = \frac{1}{2\eta}\int_0^{\pi}\int_0^{2\pi}(|G_{co}(\theta,\phi)|^2 + |G_{xp}(\theta,\phi)|^2)\sin\theta d\theta d\phi \tag{A.2}$$

In calculation of relative quantities we will however use the following power integral simplified through normalization,

$$P = 2\eta P_{rad} = \int_0^{\pi}\int_0^{2\pi}(|G_{co}(\theta,\phi)|^2 + |G_{xp}(\theta,\phi)|^2)\sin\theta d\theta d\phi \tag{A.3}$$

A.2 Body of Revolution (BOR)

The geometrical structures of several antennas are rotationally symmetric, or bodies of revolution (*BOR*), such as biconical antenna and circular horn, etc. However, *BOR* antennas do not guarantee rotationally symmetric far field functions. Anyway, the ϕ variation of the far field can always be expanded in Fourier series, as the far field is periodic with ϕ,

$$\begin{aligned}\overrightarrow{G}(\theta,\phi) &= \textstyle\sum_{n=0}^{\infty}[A_n(\theta)\sin(n\phi)+B_n(\theta)\cos(n\phi)]\hat{\theta} \\ &+ \textstyle\sum_{n=0}^{\infty}[C_n(\theta)\cos(n\phi)-D_n(\theta)\sin(n\phi)]\hat{\phi}\end{aligned} \tag{A.4}$$

If the feed is y-polarized and symmetrical with two symmetry planes, which is very often the case, then (A.4) reduces to [64]

$$\overrightarrow{G_y}(\theta,\phi) = \sum_{n=1}^{\infty}[A_n(\theta)\sin(n\phi)\hat{\theta}+C_n(\theta)\cos(n\phi)\hat{\phi}] \tag{A.5}$$

which indicates a sum of BOR1 (n=1, i.e. the first order component), $BOR2$, ... $BORn$ beams. The y-polarized BOR1 beam can thus be written as follows:

$$\begin{aligned}\overrightarrow{G_y}(\theta,\phi) &= A_1(\theta)\sin\phi\hat{\theta}+C_1(\theta)\cos\phi\hat{\phi} \\ &= G_E(\theta)\sin\phi\hat{\theta}+G_H(\theta)\cos\phi\hat{\phi}\end{aligned} \tag{A.6}$$

where $G_E(\theta) = A_1(\theta)$ and $G_H(\theta) = C_1(\theta)$ are the complex far-field functions in the E- and H-planes, respectively. One major advantage with a BOR1 beam is that it is feasible to construct the entire far-field function only from the E- and H-plane patterns. For example, one can calculate the co- and cross-polar far-field functions in the ϕ=45° plane from the following simple relations [64]:

$$G_{co45}(\theta) = \frac{1}{2}[G_E(\theta)+G_H(\theta)] \tag{A.7}$$

$$G_{xp45}(\theta) = \frac{1}{2}[G_E(\theta)-G_H(\theta)] \tag{A.8}$$

And for an arbitrary ϕ plane,

$$G_{co}(\theta,\phi) = G_{co45}(\theta) - G_{xp45}(\theta)\cos 2\phi \tag{A.9}$$

$$G_{xp}(\theta,\phi) = G_{xp45}(\theta)\sin 2\phi \tag{A.10}$$

A.3 Aperture Efficiency

The antenna gain G_0 and directivity D_0 are related by the antenna efficiency e_{ant},

$$G_0 = e_{ant}D_0 \tag{A.11}$$

and e_{ant} can be expressed by

$$e_{ant} = e_{refl}e_{ohmic}e_{ap} \tag{A.12}$$

where e_{refl} accounts for the impedance mismatch and e_{ohmic} for the dissipation losses. The aperture efficiency e_{ap} is a measure of how efficiently the feed illuminates the reflector aperture; it will become unity for a uniform aperture illumination with constant phase and no spill-over. To characterize different properties of the feed, e_{ap} can be further factorized in different subefficiencies [64] [73] [108],

$$e_{ap} = e_{BOR1} e_{sp} e_{pol} e_{ill} e_{\phi} \tag{A.13}$$

A.3.1 BOR1 Efficiency

e_{BOR1} measures how closely the far-field function resembles a BOR1 type far-field and it is defined as the ratio of the power in the BOR1 components and the total radiated power.

$$e_{BOR_1} = \frac{P_{BOR_1}}{P} \tag{A.14}$$

where the denominator is the power integral in (A.3), and the numerator has to be extracted from the actual far-field. By expanding the actual far-field (θ and ϕ components) into a Fourier series, the first terms, i.e. $G_E(\theta)$ and $G_H(\theta)$ in (A.6), can be obtained by

$$G_E(\theta) = \frac{1}{\pi} \int_0^{2\pi} G_\theta(\theta, \phi) \sin\phi d\phi \tag{A.15}$$

$$G_H(\theta) = \frac{1}{\pi} \int_0^{2\pi} G_\phi(\theta, \phi) \cos\phi d\phi \tag{A.16}$$

From [[64]: Eq. 2.92], we know the power of a BOR1 beam,

$$P_{BOR_1} = \pi \int_0^{\pi} (|G_E(\theta)|^2 + |G_H(\theta)|^2) \sin\theta d\theta \tag{A.17}$$

Finally, we get the BOR1 Efficiency as

$$e_{BOR_1} = \frac{\pi \int_0^{\pi} (|G_E(\theta)|^2 + |G_H(\theta)|^2) \sin\theta d\theta}{\int_0^{2\pi} \int_0^{\pi} (|G_{co}(\theta, \phi)|^2 + |G_{xp}(\theta, \phi)|^2) \sin\theta d\theta d\phi} \tag{A.18}$$

A.3.2 Spillover Efficiency

e_{sp} measures how much of the radiation that hits the reflector. It is the power within the subtended angle θ_0 relative to the total BOR1 power,

$$e_{sp} = \frac{\pi \int_0^{\theta_0} (|G_E(\theta)|^2 + |G_H(\theta)|^2) \sin\theta d\theta}{\pi \int_0^{\pi} (|G_E(\theta)|^2 + |G_H(\theta)|^2) \sin\theta d\theta} \tag{A.19}$$

where both the numerator and denominator are given in (A.16) with the only difference being the integration limits. Note that we hereinafter only use the BOR1 components since all other components have already been removed and accounted for.

A.3.3 Polarization Sidelobe Efficiency

As a BOR1 excitation has zero cross polarization on the propagation axis, this polarization sidelobe efficiency is a measure of the power lost in cross-polar sidelobes within θ_0. It is sufficient to use the following expression for both circular and linear polarizations [64],

$$e_{pol} = \frac{\int_0^{\theta_0}(|G_{co45}(\theta|^2 \sin\theta d\theta}{\int_0^{\theta_0}(|G_{co45}(\theta)|^2 + |G_{xp45}(\theta)|^2)\sin\theta d\theta} \tag{A.20}$$

A.3.4 Illumination Efficiency

The illumination efficiency arises due to the fact that the illumination of the reflector is not uniform in most cases. The expression given below is only valid for BOR1 type far-field functions.

$$e_{ill} = 2cot^2(\frac{\theta_0}{2})\frac{[\int_0^{\theta_0}|G_{co45}(\theta)|\tan(\frac{\theta}{2})d\theta]^2}{\int_0^{\theta_0}|G_{co45}(\theta)|^2\sin\theta d\theta} \tag{A.21}$$

e_{ill} becomes unity for a uniform aperture illumination, i.e., when $E_{co45}(\rho) = \text{const}$, corresponding to $G_{co45}(\theta) = \text{const}/\cos^2(\theta/2)$.

A.3.5 Phase Efficiency

The phase efficiency is due to phase errors in the co-polar far-field and it is the only subefficiency that depends on the phase reference point of the feed relative to the focal point of the reflector.

$$e_{\phi} = \frac{|\int_0^{\theta_0} G_{co45}(\theta)\tan(\frac{\theta}{2})d\theta|^2}{[\int_0^{\theta_0}|G_{co45}(\theta)|\tan(\frac{\theta}{2})d\theta]^2} \tag{A.22}$$

A phase center can further be defined such that the location of feed maximizes the phase efficiency. If the feed is located with its phase center in the focal point, e_{ϕ} is normally very high; and if the co-polar far field function has constant phase, e_{ϕ} is 100%.

Appendix B

Far Field of Paraboloidal Reflector

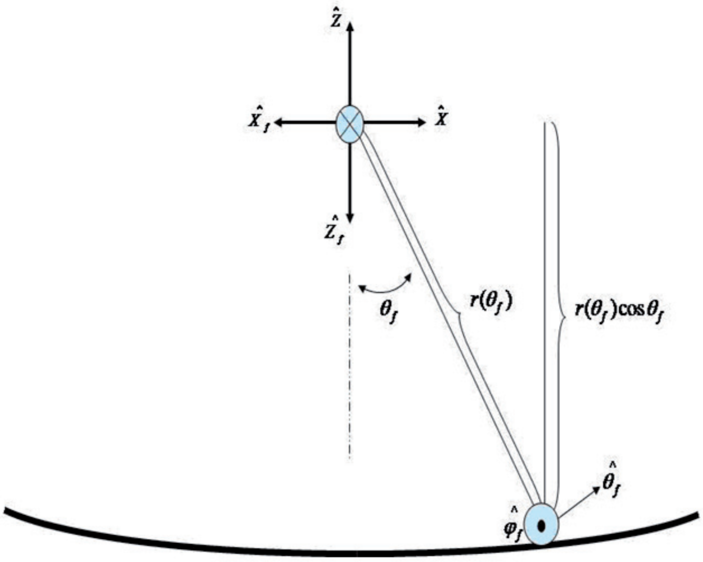

Figure B.1: GO reflection at a parabolic surface

The field equivalence principle is widely used in the analysis of aperture antennas. It replaces an aperture antenna with equivalent electric and/or magnetic currents, which can produce radiation field equivalent to those from the antenna. Geometrical optics (GO) has been known as an approximate method to determine electromagnetic fields, which is asymptotically correct for high frequencies. It is reasonable to assume all incident fields are reflected at the parabolic surface by the classical reflection law, and then propagate along parallel straight lines, referred to as GO rays, in free space. In addition, we also assume a circular aperture, normal to the propagation direction of the GO rays, in front of the reflector. The far field after reflection can be approximated by integration of equivalent Huygen's sources in the virtual aperture.

Given an arbitrary E-field on a free space aperture (area A) in the xy-plane, with the source coordinates $\overrightarrow{r'} = x'\hat{x} + y'\hat{y}$,

$$\overrightarrow{E_a}(r') = E_{ax}(x', y')\hat{x} + E_{ay}(x', y')\hat{y} \tag{B.1}$$

the far field function in the spherical coordinate system of such a free space aperture turns out to be [[64]: Eqs. 6.20-6.21]

$$\begin{aligned} \overrightarrow{G}(\theta, \phi) = & \tfrac{jk}{2\pi}\cos^2(\tfrac{\theta}{2})[\cos\phi\hat{\theta} - \sin\phi\hat{\phi}]\widetilde{E_{ax}}(k\sin\theta\cos\phi, k\sin\theta\sin\phi) \\ & + \tfrac{jk}{2\pi}\cos^2(\tfrac{\theta}{2})[\sin\phi\hat{\theta} + \cos\phi\hat{\phi}]\widetilde{E_{ay}}(k\sin\theta\cos\phi, k\sin\theta\sin\phi) \end{aligned} \tag{B.2}$$

where

$$\widetilde{E_{ax}}(k\sin\theta\cos\phi, k\sin\theta\sin\phi) = \int\int_A E_{ax}(x', y')e^{j(k\sin\theta\cos\phi x' + k\sin\theta\sin\phi y')}dx'dy' \tag{B.3}$$

$$\widetilde{E_{ay}}(k\sin\theta\cos\phi, k\sin\theta\sin\phi) = \int\int_A E_{ay}(x', y')e^{j(k\sin\theta\cos\phi x' + k\sin\theta\sin\phi y')}dx'dy' \tag{B.4}$$

As illustrated in Figure B.1, the feed is assumed to be a point source at the focal point of the paraboloidal reflector. The feed coordinate system denoted with subscript *f*, and the reflected far field coordinate system without subscript, have their origins at the focal point (i.e. the center of the virtual aperture), but point in opposite directions. Consider a general case where the feed has a far field function with arbitrary form,

$$\overrightarrow{G_f}(\theta_f, \phi_f) = G_{\theta_f}(\theta_f, \phi_f)\hat{\theta_f} + G_{\phi_f}(\theta_f, \phi_f)\hat{\phi_f} \tag{B.5}$$

where $G_{\theta_f}(\theta_f, \phi_f)$ and $G_{\phi_f}(\theta_f, \phi_f)$ are θ and ϕ components of the far field function of the feed, respectively; θ_f is the polar angle and ϕ_f is the azimuth angle in the spherical coordinate system of the feed. As ϕ_f is periodic with 2π, the ϕ_f variation of the far field can be expanded in a Fourier series,

$$\begin{aligned} \overrightarrow{G_f}(\theta_f, \phi_f) = & \textstyle\sum_{n=0}^{\infty}[A_n(\theta)\sin(n\phi_f) + B_n(\theta)\cos(n\phi_f)]\hat{\theta_f} \\ & + \textstyle\sum_{n=0}^{\infty}[C_n(\theta)\cos(n\phi_f) - D_n(\theta)\sin(n\phi_f)]\hat{\phi_f} \end{aligned} \tag{B.6}$$

Especially if the feed is y_f-polarized and symmetrical with respect to both Y_fZ_f-plane and X_fZ_f-plane, then (B.6) can be reduced to

$$\overrightarrow{G_f}(\theta_f, \phi_f) = \sum_{n=1}^{\infty}[A_n(\theta)\sin(n\phi_f)\hat{\theta_f} + C_n(\theta)\cos(n\phi_f)\hat{\phi_f}] \tag{B.7}$$

The focal aperture field of a reflector fed by a pure BOR1 beam has been formulated through [[64]: Eqs. 8.41-8.49] by assuming GO reflection. In a similar way, the focal aperture field contributed by any other order BOR beams can readily be analyzed as well. Thereafter, the far field of the reflector fed by them can thus be approximated by using aperture integration. For BOR_n (n>0), the focal aperture field can be expressed as follows,

$$\begin{aligned}\overrightarrow{E_a}(\rho', \phi') &= \pm\frac{e^{-jk\cdot 2F}}{F}\cos^2(\tfrac{\theta_f}{2})[A_n(\theta_f)\sin(n\phi')\hat{\rho'} + C_n(\theta_f)\cos(n\phi')\hat{\phi'}] \\ &= \pm\frac{e^{-jk\cdot 2F}}{F} cos^2(\tfrac{\theta_f}{2})\{[A_n(\theta_f)\sin(n\phi')\sin(\phi') + C_n(\theta_f)\cos(n\phi')\cos(\phi')]\hat{y} \\ &\quad +[A_n(\theta_f)\sin(n\phi')\cos(\phi') - C_n(\theta_f)\cos(n\phi')\sin(\phi')]\hat{x}\}\end{aligned} \tag{B.8}$$

where ρ' is the radial and ϕ' is the azimuth angle in the polar coordinate system of the focal aperture, k is the phase constant, F is the focal length, and θ_f is associated with ρ' by [[64]: Eq. 8.32]. According to [[64]: Eqs. 6.50-6.51], the co-polar ($y-$) component of the aperture integration due to the previous focal aperture field will become,

$$\begin{aligned}\widetilde{E_{ay}}(k\sin\theta\cos\phi, k\sin\theta\sin\phi) &= \int_0^{d/2}\int_0^{2\pi} E_{ay}(\rho', \phi')e^{jk\rho'\hat{\rho'}\cdot\hat{r}}\rho' d\rho' d\phi' \\ &= \hat{y}\frac{-e^{jk\cdot 2F}}{F}\int_0^{d/2}\cos^2(\tfrac{\theta_f}{2})\rho' d\rho' \cdot \int_0^{2\pi}[A_n(\theta_f)\sin(n\phi')\sin(\phi') \\ &\quad +C_n(\theta_f)\cos(n\phi')\cos(\phi')]e^{jk\rho'\sin\theta\cos(\phi-\phi')}d\phi'\end{aligned} \tag{B.9}$$

where θ and ϕ are the polar and azimuth angle coordinates of the far field spherical system. Especially if $\theta = 0$, i.e. along the z-axis, it can easily be found that the field in (B.9) turns out to be zero as long as $n \neq 1$. This implies that if an arbitrary beam is fed to a rotationally symmetric reflector, it is only its BOR1 component that will make contribution on the propagation axis, while any of other order ϕ-variant components always has a null on the propagation axis. In other words, all other order ϕ-terms can not contribute to the on-axis gain and may thus be regarded as losses in the total radiation efficiency.

Appendix C

List of Publications

1. Jungang Yin and Jian Yang. "A 2-5 GHz Circular Eleven Antenna With Improved BOR1 Efficiency," *The 2011 International Symposium on Antennas and Propagation and USNC/URSI National Radio Science Meeting*, Spokane, WA, USA, Jul. 2011.

2. J. Yang, D. Nyberg and J. Yin. "Impedance Matrix of a Folded Dipole Pair under Eleven Configuration," *IET Transactions on Microwaves, Antennas and Propagation*, vol. 4.(6) pp. 697-703, 2010.

3. Jungang Yin and Jon Anders Aas. "Study on Dual/Wide-Band Orthogonal Folded Dipoles," *The 20th Asia Pacific Microwave Conference*, Hong Kong and Macao, Dec. 2008.

4. Jungang Yin, Daniel Nyberg, Xiaoming Chen and Per-Simon Kildal. "Characterization of Multi-Port Eleven Antenna for use in MIMO System," *The 13th International Symposium on Antennas and Propagation*, Taipei, Taiwan, Oct. 2008.

5. Jungang Yin, Per-Simon Kildal and Jon Anders Aas. "Study on a Parabolic Reflector Fed by L-band Multi-port Eleven Antenna," *The 6th WSEAS International Conference on Applied Electromagnetics, Wireless and Optical Communications*, Trondheim, Norway, Jul. 2008.

6. Jian Yang, et al. and Jungang Yin. "Development of decade bandwidth and multiband feeds for future scientific and commercial reflector antenna systems," *RVK08 - The 20th Nordic Conference on Radio Science and Communications*, Sweden, Jun. 2008.

7. Jungang Yin, Jon Anders Aas, Jian Yang and Per-Simon, Kildal. "Monopulse Tracking Performance of Multi-port Eleven Antenna for use in Satellite Communications Terminals," *The 2nd European Conference on Antennas and Propagation*, Edinburgh, UK, Nov. 2007.

8. Jungang Yin, Jon Anders Aas and Per-Simon Kildal. "Multi-Port Eleven Antenna For

Use In Satellite Communications Terminals," *VERDIKT Conference 2007*, Trondheim, Norway, Oct. 2007.

9. Jian Yang; Jungang Yin. "The Eleven Antenna Feed for Monopulse Tracking and Combining L-, C-, X- and Ku- Satellite Bands," *The 29th ESA Antenna Workshop on Multiple Beams and Reconfigurable Antennas*, the Netherlands, Apr. 2007.